Electrochemical Control for Nanoelectromechanical Device Production

by

Nima Moghimian
B.A.Sc., Sharif University of Technology, 2008
M.Sc., University of Barcelona, 2010

A Dissertation Submitted in Partial Fulfillment of the
Requirements for the Degree of

DOCTOR OF PHILOSOPHY

in the Department of Mechanical Engineering

Electrochemical Control for Nanoelectromechanical Device Production

by

Nima Moghimian
B.A.Sc., Sharif University of Technology, 2008
M.Sc., University of Barcelona, 2010

Supervisory Committee

Dr. R.B. Bhiladvala, Supervisor
(Department of Mechanical Engineering)

Dr. R.A. Herring, Departmental Member
(Department of Mechanical Engineering)

Dr. D.A. Harrington, Outside Member
(Department of Chemistry)

Supervisory Committee

Dr. R.B. Bhiladvala, Supervisor
(Department of Mechanical Engineering)

Dr. R.A. Herring, Departmental Member
(Department of Mechanical Engineering)

Dr. D.A. Harrington, Outside Member
(Department of Chemistry)

ABSTRACT

Electrochemical synthesis of straight, separable, cylindrical nanowires for use as cantilevered mechanical resonators is the main focus of this dissertation. These types of nanowires are significant for many applications, but particularly so for chip-based sensor arrays made for ultrasensitive mass detection. Directed-assembly of nanowire-based devices has enabled the development of large-area fabrication of sensor devices with new functions such as cancer detection at early stage.

Chemically stable noble metals gold and rhodium are interesting materials for making nanowire resonators. Gold makes a well-known, stable and strong bond with the thiol group, which enables a range of surface functionalization chemistries. Rhodium nanowires have desirable mechanical properties for resonant mass sensing as they can retain high quality factor (Q-factor) from high vacuum to near atmospheric pressures.

As a versatile and inexpensive tool, electrodeposition provides the most suitable synthesis path for gold and rhodium resonator-grade nanowires in nanoporous templates. In this work, the structural characteristics of nanoporous membranes anodized aluminium oxide and track-etched polycarbonate was explored for use as electrodeposition template. New chemistries for making gold and rhodium nanowires are

introduced. Although gold cyanide-based solutions work well for the electrochemical synthesis of separable nanowires, the toxicity of cyanide solutions makes non-cyanide alternatives desirable. However, electrochemical synthesis of gold nanowires in templates from non-cyanide solutions suffers from serious drawbacks. These include growth-arresting pellet formation, poor length control and defects such as inclusions. In this dissertation, the first electrochemical synthesis of straight, cylindrical, separable gold nanowires from a sulfite-based solution is presented. This work demonstrates a scheme that suppresses electroless particle growth in the weakly-complexed gold in solution by proper use of additives.

The electrochemical nucleation and growth of rhodium nanowires from a sulphate-based solution is also discussed. The effect of pH on the length uniformity as well as the effect of EDTA and polyethylenimine as additives on the development of the wire nanostructure was studied. This study has shown that the control over hydrogen co-reduction on the electrode surface and its bubble transport rate allowed for tailoring the nanostructure of the grown nanowires.

The control over electrochemical nucleation and growth of noble metal films for nanowire clamping has also been investigated in this work for making reliable defect-free clamps for nanoresonator measurements. Silver was introduced as a reliable replacement for gold for nanowire clamping. Resonance measurements of rhodium nanowires clamped with silver, confirmed a reliable and repeatable clamp with very small scatter in the plot of resonance frequency variation with appropriate geometric terms. In addition, we found that the elastic modulus of a set of rhodium nanowires synthesized and measured in this work, was 14% larger than in previous studies.

Contents

List of Tables

List of Figures

ACKNOWLEDGEMENTS

I would like to thank:

My supervisor, Dr. Rustom Bhiladvala, who trusted me, taught me how to think like a scientist, to ask the right questions and look for their answers. He was always there for me when I was sad, hopeless and sick.

Dr. Rodney Herring for all his helpful comments and assistance with the TEM and electron diffractions.

Dr. David Harrington for his valuable guidance on the electrochemical studies.

My colleague and friend, Sahar Sam, with whom I shared all my hopes and disappointments in the lab.

Adam Schuetze and Dr. Elaine Humphrey for their support with SEM, FIB and other tools at the Advanced Microscopy Facility.

Dr. Alex Brolo and Mahdieh Atighi for the use of Brolo's Lab and help with the chemical experiments.

My group members: Fan Weng, Jehad Alsaif and Amin Ebrahiminejad for their help with the experiments.

My aunt and uncle, Farnoush and Farid, who welcomed me at their home and supported me since my arrival in Victoria.

My friend, former colleague and roommate, Ali Etrati, for all the fun and sad moments we shared at UVic and home and delicious times of cooking.

Azadeh Fattahi, for her constant love, patience and support.

All my dear friends and fellow grad students at UVic, especially: Azadeh Hajihosseini and Mana Norouzpour.

And last but not least, my beloved family: Jamileh, Ahmad, and Pouya for their lifetime support.

DEDICATION

To:

Jamileh, Ahmad and Pouya;
and the memory of Iman Bulghani.

Chapter 1

Introduction

The purpose of this document is to describe how materials science and the knowledge of electrochemistry can be used to alter the mechanical properties and the performance of cantilevered nanoresonators, an example of nanoelectromechanical systems. This study explains the challenges involved in the templated electrochemical synthesis and assembly of gold and rhodium nanowires for use as cantilevered nanoresonators and the solutions to these difficulties. This PhD dissertation does not cover the details of mechanical resonance physics or the optical detection method. The resonance measurements carried out in this dissertation were only intended for validation of the new electrochemical and materials work.

Although an extensive literature has been built on the synthesis of metal "nanowires" (NWs) in the past few decades, very little attention has been given to application-specific synthesis of NWs especially for their use as mechanical resonators. An ideal NW resonator should be straight, uniform in diameter, free of defects such as voids or branches, and long enough to be able to easily clamp on a device chip.

An ideal NW resonator synthesis method should make a large number of NWs that are separable (to make multiple single devices) with a narrow size distribution, and cost-effective. The technique should provide "clean" NWs with minimal surface contamination. The material synthesis technique also significantly affects the mechanical properties of the nanoresonator such as Young's modulus or stiffness, as well as the effective density. These contribute to the quality factor (Q-factor) of the resonator and its resonance frequency.

1.1 What Is Not New?

Electrodeposition of metals is about two centuries old and has evolved from an art to a "science" [1]. Use of nanoporous templates for growing NWs is not new either. Martin [2] and many others have been using the idea since more than twenty years.

Even electrodeposition of gold and rhodium NWs for use as cantilevered nanomechanical resonator is not very new. Li and Bhiladvala [3, 4] have used gold, rhodium and silicon template-grown NWs as resonators.

1.2 What Is New?

Combining electrochemistry and materials science for making better mechanical resonators is new. In this work we have used new chemistries and additives for electrodeposition of gold and rhodium that allows control over the electrochemical nucleation and growth of deposited NWs.

Resonator application-oriented growth of NWs by tuning the electrochemical parameters of the synthesis technique is new. What is called NW in general may refer to shapes that are useful for applications like catalysis but not useful at all for other applications such as mechanical resonators.

In this work, structural characteristics of a number of templates have been critically explored to find the most useful template for each area of resonator application.

Also, applying electrodeposition knowledge for producing NW clamps with reliable mechanical rigidity is new.

1.3 Background

This dissertation pulls three research lines together: materials nucleation and growth, templated electrochemical synthesis of NWs and the electromechanical resonance of the cantilevered beams. This section briefly provides background information on how the three topics can be related to each other in a single problem.

Figure 1.1 shows a schematic and a scanning electron microscope (SEM) image of a typical cantilevered nanoelectromechanical resonator made in this work. The rhodium NW resonator is clamped at one end with an electrodeposited silver clamp. The other end of the NW is free to resonate on top of an evaporated gold pad. The

gold pad is used for electrically driving the NW and also for laser light reflection used for resonance frequency measurement.

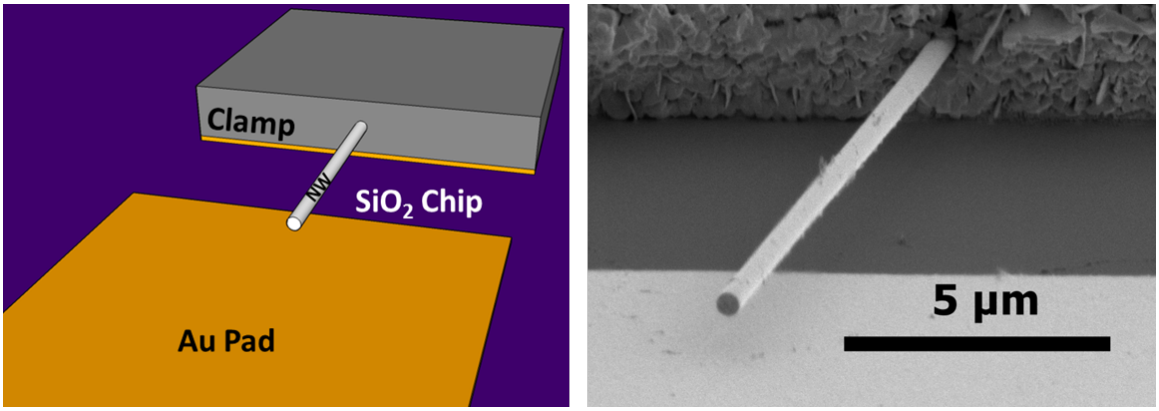

Figure 1.1: A schematic and SEM image of a rhodium electromechanical resonator with 13.6 μm suspended length and a diameter of ~450 nm. The nanoresonator is clamped using an electrodeposited silver and can be driven by electrically biasing the gold pad.

The resonance frequency (f) of a linear cylindrical flexural cantilevered beam with a Q-factor much larger than one, is given by:

$$f = \frac{\beta^2}{8\pi}\sqrt{\frac{E}{\rho}}\frac{D}{L^2} \tag{1.1}$$

where E and ρ are the Young's modulus and the density of NW, D and L are the NW diameter and suspended length. The constant β for a rigidly clamped cantilever vibrating in the fundamental mode is 1.88 [4].

Based on Eq. 1.1, the term relevant to the NW material mechanical properties is mainly the Young's modulus E. A previous study [5] has measured the value for gold NW Young's modulus ranging 44 to 110 GPa. This suggests that the control over the nucleation and growth process of gold NW can potentially change E by 150% and therefore, change f by more than 120%. Maintaining the clamp constant β also requires control over the nucleation and growth process of the clamp deposit. Formation of voids or other hollow defects can reduce the density (ρ). Moreover the Eq. 1.1 is strictly valid only for a perfect cylinder resonator. This could be achieved by using a template product with highly cylindrical pores.

While cylindrical and non-branched NWs are most suitable for electromechani-

cal resonator devices, metal NWs that are not perfect cylinders and/or have small branches were used by colleague Mahshid Sam to make conductive networks by applying dielectrophoresis forces [6]. Ordered arrays of chained NWs between two lithographically-patterned electrodes create low-resistance contacts. Electrical properties of metallic NWs (gold, silver and rhodium) render rapid response to applied electric field, and result in NW orientation and connection along the electric field direction. Formation of aligned NW network with stable electrical conductivity between electrodes could be useful for fabrication of high performance photovoltaic devices.

1.4 Research Aims and Questions

The research work described in this dissertation was motivated by the fact that an improvement in the electrochemical material synthesis can significantly affect the productivity and reliability of several applications enabled by the nanoelectromechanical resonators. These applications include mass sensing down to 10^{-18} g [7], biomedical sensing for early detection of cancer [8], and rarefied gas dynamics studies [3]. The research aims and questions, listed in this section, address the challenges relevant to nanoelectromechanical devices that can be significantly improved by control over electrochemical material synthesis process.

1.4.1 Research Aim I: Investigate Templates for Nanowire Production

Since the pore structure of the template material determines the shape of the NW resonator, the characteristics of several candidate template materials were investigated. The goal is to find a porous template that is closest to an ideal defect-free membrane. Connected or partially connected, branched and non-uniform pores are considered defective in the context of this research work. Also membranes with pores that are not perfectly cylindrical are not the most suitable membranes for NW resonator synthesis. Therefore, one of the initial goals of this work was to explore the structural characteristics of the membranes materials as candidate templates for NW resonator synthesis.

1.4.2 Research Aim II: Develop Gold Nanowire Growth from a Non-cyanide Solution

The second research aim of this work was synthesizing resonator-quality gold NWs from a non-cyanide solution. Gold is an interesting nanoresonator material due to its high chemical resistance and its ability to form strong thiolated bonds with biomaterials. Gold cyanide is strongly complexed in solution and is excellent for the electrochemical synthesis of NWs but is highly toxic and its resistance to decomposition, disproportionation and substitution reactions lead to environmental concerns. Gold sulfite is a plausible, well-studied alternative to gold potassium cyanide and poses considerably lower risk from safety and handling. Previous studies have shown that during electrochemical deposition of gold from aqueous sulfite solution, gold nanoparticles are formed electrolessly as a result of low stability constant of complexed gold and evolution of hydrogen nanobubbles. Gold nanoparticle (pellet) formation prevents growth of high aspect-ratio NWs inside the template. In this work we target electrodeposition of long, straight and separable gold NWs from a sulfite-based solution.

1.4.3 Research Question III: Can Electrodeposition Allow Control over Geometry and Grain Structure?

The third research question of this dissertation is whether straight, separable rhodium NWs with various grain morphologies can be made by controlling the eletrochemistry of the synthesis. Rhodium NWs have desirable mechanical properties for resonant mass sensing as they can retain high Q-factor from high vacuum to near atmospheric pressures. Moreover, rhodium's chemical stability and the relatively high strength of its bond with the thiol group enable a range of surface functionalization chemistries particularly for biomolecular diagnosis. The research question to answer is if the control over electrochemical deposition conditions allow control over shape (e.g. rod vs tube) of the electrodeposit and its grain size, morphology and structure? This control would affect the mechanical properties and the performance of the nanoresonators.

1.4.4 Research Aim IV: Control of Electrodeposited Nanowire Clamp Properties

After making gold and rhodium NWs, the fourth research aim is to control electrochemical conditions for NW clamping with repeatable mechanical rigidity. The electrochemical conditions have to be tuned for different clamp materials and wafer circuit designs. Choosing the appropriate clamp material also had to be explored in this work. In order for the clamp material deposit to be smooth, compact and uniform with an intimate coverage of NW, several experiments had to be performed for each material–wafer pair.

1.4.5 Research Question V: What Can Be Learnt about Device Production from Resonance Measurement?

The final research aim is to draw the connecting line starting from the material's electrochemical nucleation and growth all the way to the mechanical performance of the NW resonator on the chip. The aim is to obtain the resonance spectra from several batches of NWs made under different electrochemical conditions and relate their mechanical properties to their grain structure evolution during the electrodeposition process. This should lead to understanding more about what can be improved in the nanoelectromechanical device production for more useful and reliable tests.

1.5 Structure of Dissertation

This dissertation comprises two results-included, introductory chapters on the templated NW electrodeposition and the electrochemical nucleation and growth. These are followed by two chapters that present the contributions in the form of peer-reviewed papers on gold and rhodium NW synthesis.The next two chapters present the results of NW resonator clamping and validating resonance measurements. Finally the last chapter lists all the conclusions from this dissertation.

There is no separate *methods* or *experimental* chapter in this document. The methodological details have been presented in each chapter as-needed. In cases where the experimental details are long, the reader is directed to external sources or the Appendices. Also, a few mini-studies that were not aligned in the main stream direction of the nanoresonator synthesis work, are presented in the Appendix section.

The relevant background and literature review information are presented in each section where needed, to avoid an exhaustive literature review chapter. Each chapter terminates with a Conclusions and Future Work section.

Chapter 2 briefly summarizes the electrochemical deposition principles, methods and conditions used in this work and it then focuses on the membrane materials used as template for NW growth. This chapter addresses the structural characteristics of five commercially available template products made from either aluminium oxide or polycarbonate. Template preparation method and NW extraction technical details are discussed and finally a critical comparison on choosing the suitable template product is given.

Chapter 3 focuses on the electrochemical nucleation and growth of metals from aqueous solutions. The introductory principles presented in the beginning of this chapter are directly relevant to both NW synthesis and clamp electrodeposition discussed in Chapter 6. The characterization methods (mainly electron microscopy) used for studying the nucleation and growth process is also discussed in this chapter. Nucleation and growth of silver and gold inside nanoporous membranes from the typical electrolytes used in this work are presented. Nucleation and growth of rhodium is mainly described in Chapter 5.

Chapter 4 presents a peer-reviewed published[1] article [9] with results from gold NW synthesis using a sulfite-based solution. The article mainly explains the enabling role of polyethyleneimine additive in the first successful growth of long, straight, cylindrical gold NWs from a non-cyanide solution.

Chapter 5 presents a peer-reviewed published[2] article [10] with results from rhodium NW synthesis using a sulfate-based solution. The article describes the effect of hydrogen evolution, working potential and the pH on the NW uniformity and growth. It also shows that grain structure can be altered by use of additives such as EDTA and polyethyleneimine.

Chapter 6 mentions the NW resonator directed assembly, NW clamping and chip fabrication. The main focus of this chapter is the challenges involved in the NW clamping for making cantilevered devices and how can electrochemical conditions alter

[1]Moghimian, Nima, Mahshid Sam, Jesse D. Coelho, Stephen D.W. Warwick, and Rustom B. Bhiladvala. "Suppressing electroless growth allows cyanide-free electrodeposition of straight separable gold nanowires" *Electrochimica Acta* 114 (2013): 643-648.

[2]Moghimian, Nima, Mahshid Sam, and Rustom B. Bhiladvala. "Rhodium nanowires: Synthesis and nanostructure tailoring by controlling hydrogen evolution" *Materials Letters* 113 (2013): 152-155.

the clamp quality. Chapter 6 discusses the clamp material requirements for providing sufficient mechanical support and reliability for the resonance measurement. The considerations for quality clamp electrodeposition for two wafer chip designs used in this work are given in this chapter.

Chapter 7 is the validation of all the previous works described in Chapters 2 through 6. The resonance measurement setup and methodology are presented. The resonance results from NWs made in this research work are provided together with a discussion on how the results obtained in this work compare to the previous measurements.

Chapter 8 summarizes the main outcomes of this PhD work.

Chapter 2

Electrodeposition of Metals in Nanoporous Templates

This chapter describes the process of electrodeposition (also known as electrochemical deposition) of NWs in porous membranes and provides information on various types of membranes used as a template in this study. The structural features of the templates used are described and finally a conclusion on template material choice for resonance NW fabrication is presented towards the end of the chapter.

2.1 Why Electrochemical Synthesis?

A number of processes have been used for the synthesis of various kinds of NWs. These processes mainly include chemical vapor deposition (CVD) such as vapor-solid-liquid (VLS) growth processes [3], electroless [11], and sol-gel [12] methods. NWs synthesis methods can be classifed into two general categories, so-called soft-template and hard-template techniques [13]. In the soft-template method, NW growth occurs by chemical or electrochemical reduction, usually in a solution that contains surfactants or other structure-directing molecules. In the hard-template method, an inorganic material or polymer, typically in the form of a porous membrane, acts as rigid mold for the chemically or electrochemically grown replica [13].

Hard template electrodeposition is a wet chemical technique in which NWs are grown by metal ion reduction within the pores of a membrane. One of the main advantages of electrodeposition is that it can be operated at room temperature and ambient pressures. This provides a minimum of capital investment. The growing need

for processes with low cost, high throughout, high volume and ease of production, has made template-directed electrodeposition emerge as a promising process for the synthesis of NWs [2, 14].

Another advantage of electrodeposition is the ability to deposit various types of materials including metals, conductive polymers and semiconductors. The ability to deposit many different materials also provides the possibility to synthesize NWs with sequentially deposited materials by simply changing the electrodeposition solution and/or variation of the deposition potential/current. These segmented NWs have been useful in several applications such as simple identification of submicrometer patterns under light microscopes [13, 15].

Finally, the grain structure of the NW deposit can be customized for specific material properties by controlling the electrochemical parameters and use of additives in the solution. These controls will be described in more depth throughout this work, but mainly in Chapter 3.

2.2 Electrochemical Deposition Process

Electrochemical deposition of metals involves the reduction of metal ions from electrolytes. In this work, all the electrochemical deposition processes were carried out from aqueous solutions only. The reduction of metal ions M^{z+} in a solution is usually represented by [1]:

$$M^{z+}_{\text{solution}} + ze \longrightarrow M_{\text{lattice}}. \tag{2.1}$$

This process is accomplished when the z electrons (e) are provided by an external power supply —known as potentiostat or galvanostat in this context.

All the NWs in this work were grown by means of electrodeposition in commercially available nanoporous membranes as template. In an electrodeposition process, there exists an anode, an electrolyte (the target ion source) and a cathode (target deposition site). An applied stimulus (e.g., potential) reduces the target metal ions at the cathode. The amount of the deposited material is determined by the quantity of charge (current×time) and the number of electrons required per reduction reaction [16].

Figure 2.1 shows the electrochemical setup with the arrangement of electrodes and the VersaSTAT potentiostat/galvanostat used for the synthesis of NWs. In this work, the aqueous electrolyte was contained in the Teflon electrochemical cell and the

NW synthesis process was run by the VersaStudio software package.

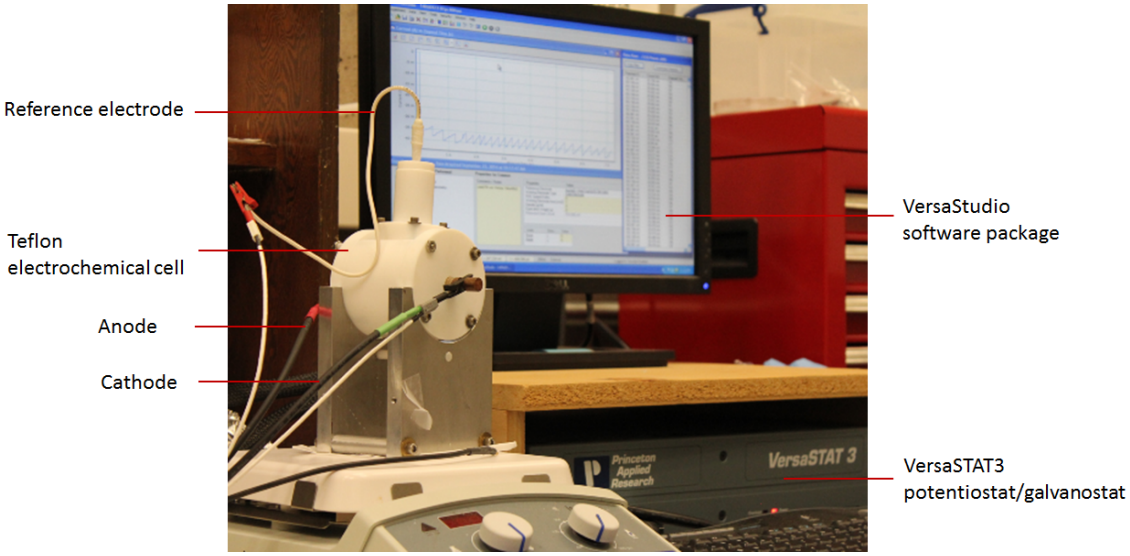

Figure 2.1: Assembled electrochemical cell connected to potentiostat/galvanostat and controlled using a VersaStudio software package for electrodepositon of NWs in this work.

2.2.1 Electrodes

In an electrodeposition process, the cathode is the negative terminal. The cathode by definition is where the reduction reaction happens. Since the metal ions in the electrolyte carry a positive charge, a relatively negative potential is required to reduce them.

The anode, however, can be one of the two types: sacrificial anode (dissolvable anode) and permanent anode (inert anode). The sacrificial anodes are made of the metal that is to be deposited. In contrast, permanent anodes only complete the electrical circuit, but do not provide a source of fresh metal to replace what has been removed from the solution by deposition at the cathode. Platinum and carbon are usually used as inert anodes. In this work, a platinum gauze was used as anode in all the NW synthesis experiments.

The metallic ions of the salt in the electrolyte carry a positive charge and are thus attracted to the cathode. When the ions reach the negatively charged electrode, it provides electrons to reduce those positively charged ions to metallic form, and then the metal atoms will be deposited onto the surface of the negatively charged

conductor.

A third electrode with a fixed potential is also needed to read other electrode potentials against that. This reference electrode (RE) has a stable and well-known electrode potential. In this work, a NaCl-saturated Ag/AgCl was used as RE. When the activity of the chloride ions is 1, a silver-silver chloride reference electrode has a potential of E^0 =+0.222 V against a Standard Hydrogen Electrode (SHE). In practice, however, it is easier to use a saturated Cl^- solution. The NaCl-saturated silver-silver chloride RE used in this work has a potential +0.194 V at 25°C with respect to the SHE [1].

A silver-silver chloride type RE was chosen because of its simplicity and its ease of operation within a large concentration of chlorine ions. Silver chloride electrodes are prevalent in electrochemistry, used primarily in pH meters. The silver chloride half-cell potentials are well documented and compensated for, over a wide range of temperatures and concentrations.

2.2.2 Electrolytes

The electrolyte is the electrical conductor in which current is carried by ions rather than by free electrons (as in a metal). The electrolyte completes an electric circuit between two electrodes. Upon application of electric current, the positive ions in the electrolyte will move toward the cathode and the negatively charged ions toward the anode. This migration of ions through the electrolyte constitutes the electric current in that part of the circuit. The migration of electrons into the anode through the wiring and an electric generator and then back to the cathode constitutes the current in the external circuit. Table 2.2.2 lists all the electrolytes used in this work for silver, gold and rhodium electrodeposition. The composition and utility of each solution will be discussed in other sections accordingly.

Table 2.1: Composition of electrodeposition solutions used in this work. Various amounts of polyethyleneimine (PEI) were used for gold electrodeposition as will be discussed in Chapter 4.

Electrolyte	Target metal	Chemical composition (g/L unless specified)
SOL1	Au	5 $HAuCl_4 \cdot 3\,H_2O$, 2 EDTA, 65 Na_2SO_3 and 12.5 K_2HPO_4
SOL2	Au	5 $HAuCl_4 \cdot 3\,H_2O$, 2 EDTA, 65 Na_2SO_3 and 12.5 K_2HPO_4 + PEI
SOL3	Au	5 $HAuCl_4 \cdot 3\,H_2O$, 2 EDTA
SOL4	Au	5 $HAuCl_4 \cdot 3\,H_2O$
SOL5	Ag	Cyless (commercial); Ag content: 24.7
SOL6	Rh	Rh225D (commercial) + 0.5 vol% H_2SO_4
SOL7	Rh	Rh225D (commercial) + 5 EDTA
SOL8	Rh	Rh225D (commercial) + 16 vol% Stress Reducer (sulfamic acid)
SOL9	Rh	Rh225D (commercial) + 0.1 vol% PEI
SOL10	Rh	Rh225D (commercial)

2.2.3 Potentiostat/Galvanostat

The VersaSTAT 3 (Figure 2.1), teamed with the VersaStudio software package, comprises a system for performing a range of electrochemical techniques. The VersaSTAT 3 is a potentiostat/galvanostat contained in a single unit. It can be controlled from any PC using the VersaStudio electrochemistry software package.

In potentiostatic mode, the VersaSTAT 3 controls the potential at the working-sense electrode with respect to the RE. The counter electrode is driven to the potential required to establish the desired working potential.

In galvanostatic operation, the VersaSTAT 3 controls the current between the counter and working electrodes at the specified fraction of the selected current range (up to the maximum of the current range). The counter electrode is driven to the potential required to establish the desired cell current. The RE is not used in the control loop, but is usually used to measure the potential at some point in the electrochemical cell relative to the working-sense connection point.

The polarity convention is that if the working electrode is driven positive with respect to the equilibrium potential, the resulting current is anodic. If the electrode is driven negative with respect to the equilibrium potential, the resulting current is

cathodic. For more information see the VersaStudio Software manual[1].

2.2.4 Electrochemical Cells

An electrochemical cell is an apparatus in which an electrochemical reaction occurs. This usually consists of a two-electrode system plus a RE. A unique design of electrochemical cell was required to work with commercial 25 mm disk membranes as the template, allowing for repeatable experiments with uniform current distribution. The design consists of five main PTFE (Teflon) pieces along with supporting components as depicted in Figure 2.2. The five Teflon parts are the body, anode end cap, cathode end cap, RE flange and plug. For more information about the Teflon electrochemical cell design and fabrication, see Jesse Coelho's May 2010 co-op work term report [2].

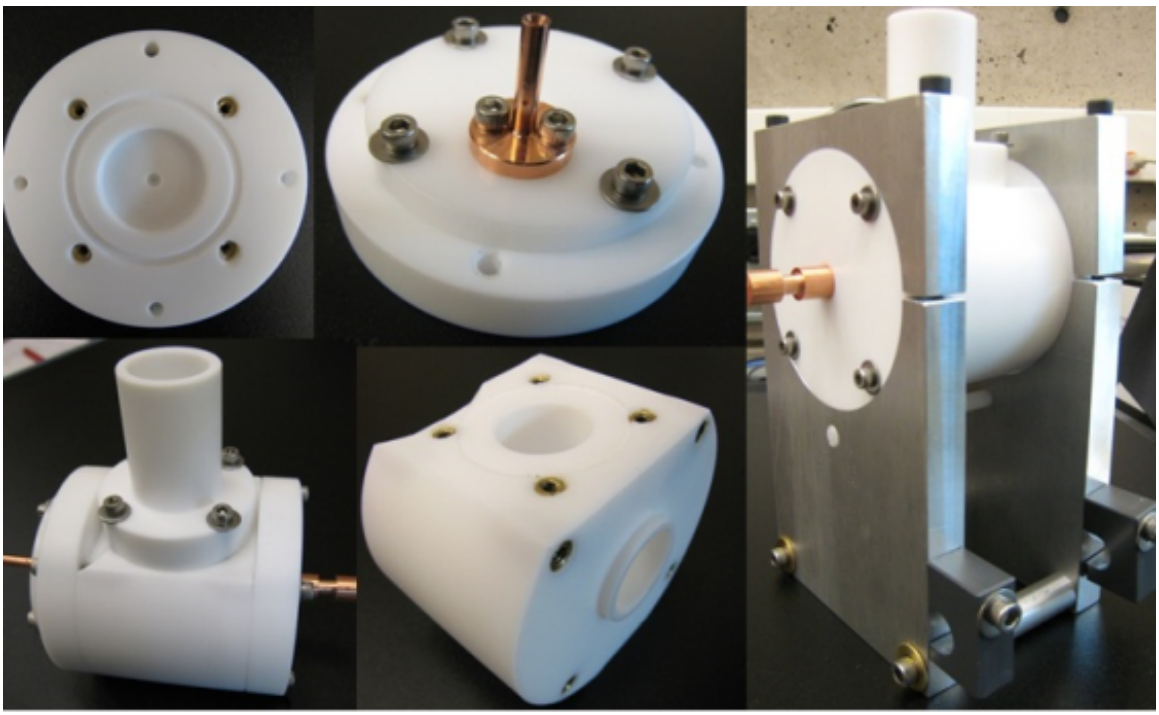

Figure 2.2: Electrochemical cell is made of Teflon.

The Teflon cell was designed for three-electrode standard configuration using platinum gauze as counter electrode and NaCl-saturated Ag/AgCl as RE. A second Teflon

[1]The manual is available online at Princeton Applied Research Webpage: www.princetonappliedresearch.com

[2]Available from UVic Engineering Coop Office.

cell was also designed and machined in a joint work with co-op student Spencer Davis, specifically for 13 mm disk templates (see Appendix A for details).

2.3 Nanoresonator Materials: Gold and Rhodium

In this work, electrochemical synthesis of two noble metals i.e., gold and rhodium, was studied in depth for specific application of nanoresonators. The reasons for these choices are briefly given in this section. Although both metals has previously been made in NW shape and utilized as resonators, the electrochemical aspect of the nucleation and growth process and its relationship to Young's modulus and Q-factor has not been investigated before. Additionally, the chemistry of synthesis solutions used in this work for both metals is new.

For nanoscale resonators made entirely from metals, there is a little work with quantitative information about the materials elastic modulus or Q-factor [3, 4]. Despite many attractive features of noble metals such as little or no native surface oxide formation, only a few reports on metal nanoresonator have been published especially before 2007. Li and coworkers [4] mention two main reasons. First, the difficulty in controlling distortion of cantilevers and residual stress. Second, previous reports of data on thin film resonators indicating high dissipations and low Q-factors. Two reports published in 2007 [4] and 2008 [3], showed that cylindrical cantilevered noble metal NW can have Q-factors higher than 1000, free of distortion and residual tension. Noble metals can extend nanoelectromechanical device applications by expanding the range of physical and chemical properties available such as high electrical and thermal conductivity, density and elastic modulus [4].

Rhodium NWs, specifically, benefit from desirable mechanical properties as resonant mass sensor as they can retain high Q-factor from high vacuum to near atmospheric pressures [3]. Moreover, rhodium's chemical stability [17] and the relatively high strength of its bond with the thiol group [18] enables a range of surface functionalization chemistries [8] particularly useful for biomolecular diagnosis.

Gold was chosen for NW resonator synthesis mainly due to its chemical stability and the well-known strength of its bond with the thiol group [18], which enables a range of surface functionalization chemistries [8] for biosensing. Table 2.2 summarizes the properties of rhodium and gold that are most relevant to NW resonator work.

Table 2.2: Range of quality factor and properties of gold and rhodium relevant to synthesis work. Q-factor and NW elastic modulus values from [4].

Material	Bulk elastic modulus (GPa)	NW elastic modulus (GPa)	Q-factor
Au	82	44	600-940
Rh	379	222	1100-1300

Although rhodium has a much higher elastic modulus, gold can be more attractive to biomedical sensing communities for its exceptionally strong thiol bond strength.

2.4 Template Synthesis Technique

The underlying principle of template synthesis technique is similar to that of producing components through the use of replication e.g. die-casting or mold casting [19], like making ice candies out of molds. In this technique, materials can be deposited within the pores of the template membranes by either electrochemical or chemical (electroless) reduction of the appropriate metal ion.

Template synthesis for preparing micro- and nanomaterials has a long history. Bean (1969) [20] first demonstrated the art of filling the pores of a membrane with silver, followed by Possin (1970) [21], who used electrodeposition technique in the fabrication of thin wires as small as 40 nm. Williams and Giordano (1984) [22] claimed to have reduced the size to 8 nm after effecting some refinements to the technique. Penner and Martin (1987) [23] reported on the preparation and electrochemical characterization of ultramicroelectrode ensembles with radii as small as 100 nm.

The Martin laboratory [2] has pioneered template synthesis, a versatile nanofabrication method. The general strategy of this approach is to deposit a precursor to the desired material into the micro- or nanopores of a template. These pores act as nanoscopic beakers. The template may be chosen from a variety of porous materials, from a commercially available organic filter to an anodized aluminium oxide membrane to an array of spherical nanobeads.

2.5 Template Materials

In this work two membrane materials were used as templates: aluminium oxide and polycarbonate. A membrane, in general, may be defined as a phase that acts as a barrier to the flow of matter or heat. In most cases, with the exception of pure liquids and solids, it is heterogeneous in structure. Perhaps the simplest conceptual heterogeneity is that of pore, i.e. a discontinuity in solids impervious phase that can allow selective transport of some chemical species. Although this sieving property has been employed for thousands of years, it is only relatively recently that a technological application like template synthesis of nano- or microstructures has been brought to this process almost a by-product and not connected with sieving property at all [24].

To date, most of the work in this area has entailed the use of two types of membrane: (1) track etch membranes, and (2) porous anodized aluminium oxide. Other materials used include nanochannel array glass, Xeolite, proteins derived from a bacterium and having nanoscopic pores, etc. (see references in Klein *et al.*, 1993 [25] and Martin, 1994 and 1996 [26, 27]). A wide variety of other nanoporous solids that can be used as template materials are cited in the literature (see for example, Martin, 1995 [28]).

2.5.1 Track-etch Membranes

Track-etch membranes in the form of nuclear track filters (NTFs) have emerged as a spin-off from solid state nuclear track detectors (SSNTDs) —solid dielectric materials capable of storing tracks of energetic, heavily ionizing ions, which can subsequently be chemically amplified for optical observation as pores or channels of well-defined geometry and density. The size or dimensions of the pores depend upon various factors such as the nature and energy of incident particles, the target material, etch conditions, e.g. temperature, nature of etchant, pre-etch storage conditions. The pore size, which is controllable, may range from a few nm to mm. NTFs have been put to numerous other applications besides their use in the synthesis of nano- or microstructures [26, 29, 30]. There exists a wealth of literature on SSNTDs and related information (see, for example [29, 31]).

A large number of materials are used as NTFs, which include mainly polymeric sheets, micas, glasses, etc. The ion track etch technique enables the generation of pores with definite shape.

In the commercial manufacturing of the NTFs, fission fragments from nuclear

reactors have been put to use. The custom-made NTFs are commercially available also in a wide variety of pore size and porosities (for example from Whatman).

Polycarbonate is perhaps the most common example of a track-etch membrane material. Other options of materials include polyester, Teflon, and polyethersulfone. In the track-etching process, One ion creates one track, which in turn becomes one pore. During production, the pore density is controlled by the duration of time that the polycarbonate film is exposed to the charged particles. Typical pore densities of a commercial track-etch membrane are 10^4-10^8 pores/cm^2 [2].

Varying parameters of this etching solution such as temperature, strength, and exposure time dictate the pore diameter. Commercial membranes are available with pore diameters ranging from 10 nm to 20 μm. The microporous material etches to form uniform cylindrical pores, but as the pore diameter is reduced to smaller nanoscopic dimensions, the shape of the pore becomes like a cigar, slightly tapered at the ends. Microscopic investigations of template-synthesized nanostructures prepared within the pores of such nanoporous membranes have shown that the diameter of the pore in the center of the membrane is usually larger than the diameter at the membrane surface producing cigar-shaped pores. It has been suggested that this pore geometry arises because the fission fragment that creates the damage track also generates secondary electrons, which contribute to the damage along the track [32]. The number of secondary electrons generated at the faces of the membrane is lesser than in the central region of the membrane. An alternate suggestion is that the surfactant protective layer adsorbed to the surface of the membrane retards the local etching process [33]. Either suggested mechanism leads to bottleneck pores.

An artifact of the random-directional nature of the fission-film interaction is that a tilt may occur in the tracks . When this tilt from the normal is significant, it causes some pores to intersect. Though, this property does not adversely affect this membrane's application as a filter, when employed as a template, this must not be ignored in certain situations such as straight separable NW synthesis in the current PhD work, which is significantly affected by this.

2.5.2 Anodized Aluminium Oxide Membranes

Porous aluminium oxide membranes are prepared electrochemically from aluminium and can have high porosity (pore density as high as 10^{11} pores/cm^2). The pores are arranged in a hexagonal array. These membranes are commercially available in only

very limited values of pore size but can be produced with pore size as small as 5 nm [24].

Anodization is an electrolytic passivation process used to increase the thickness of the natural oxide layer on the surface of metal parts. The process is called anodization because the part to be treated forms the anode electrode of an electrical circuit.

Anodization of aluminium metal in an acidic environment causes the metal to etch in a fashion that leaves a porous structure. These pores have cylindrical shapes (with small barrel, waist or tapered defects) in a hexagonal array. Unlike the track-etch process, this process is systematic and generates an isolated, nonconnected pore structure. As mentioned before, the pore densities of these aluminium oxide membranes can be on the order of 10^{11} pores/cm^2, that is about 1000 times the density available in the track-etch polycarbonate membranes. The porosities (relative surface area available for electrodeposition) can be as high as 50%. In addition, aluminium oxide membranes have much greater mechanical stability and chemical resistivity than polycarbonate [2]. However, there is an extremely limited selection of commercially available pore sizes, and the smaller pores are branched (see the Figure 2.3).

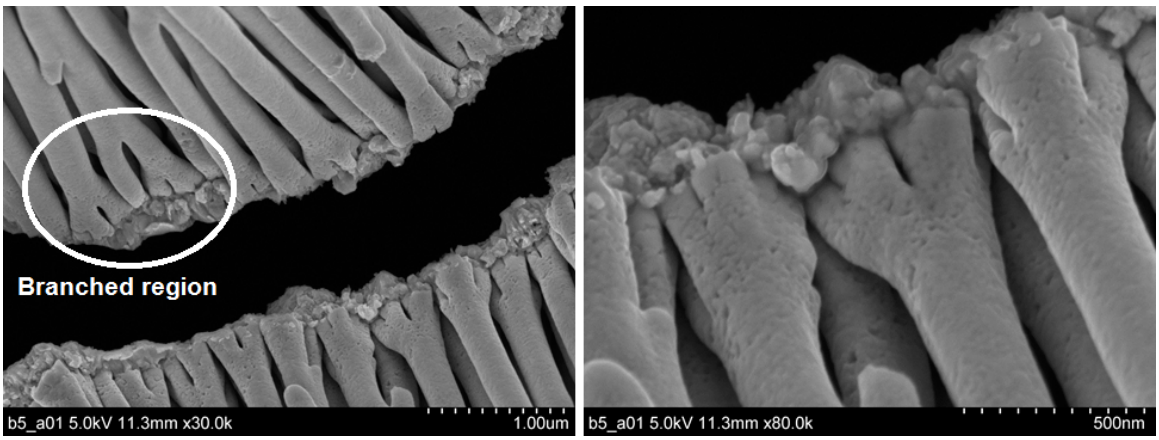

Figure 2.3: SEM images of silver electrodeposit inside a commercial aluminium oxide membrane reveal the existence of a branched region, which is a well-know issue for NW synthesis.

These membranes can be very thick (10-100 μm). It is also notable that this alumina structure is electronically insulating, which may be advantageous in certain situations such as electrochemical synthesis of NWs in this work. Whatman is perhaps the best known manufacturer of porous aluminium oxide filters commercially available. This company specializes in the so-called branched-pore aluminium oxide.

The pores of this type of alumina membrane are ∼200 nm in diameter for almost the entire length. However, near the tips of one face, the pores diverge into branches of diameters of either 100 or 20 nm. This is accomplished via a two-step anodization process , where parameters (specifically voltage) are changed during the etching process [2]. As these membranes are commercially intended filters, this pore branching allows the membranes to work as sieves.

Our results also show that in Whatman aluminium oxide membranes the branched region is normally found only on one side of the membrane and the other side is not similarly branched (see Figure 2.4).

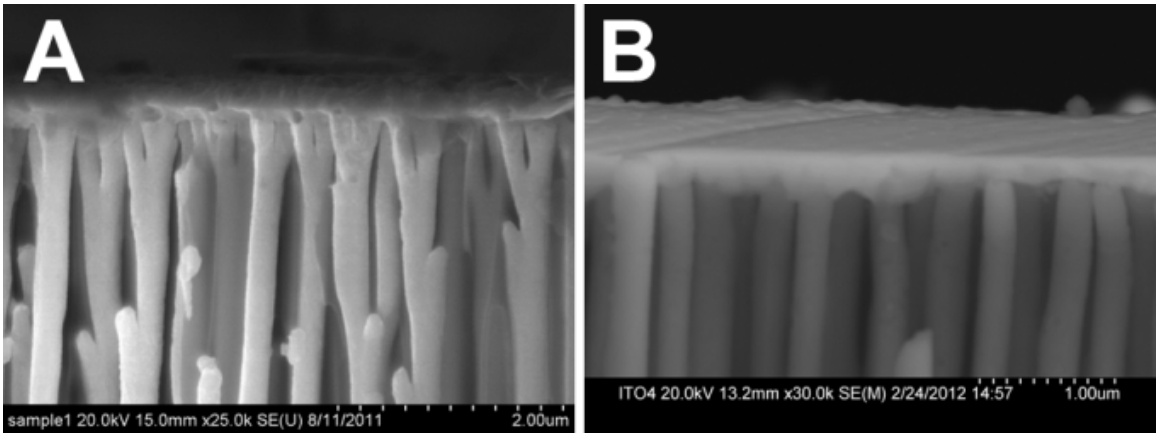

Figure 2.4: SEM results show that there is a (A) branched region side and (B) non-branched side of Whatman aluminium oxide template.

The Martin laboratory [2] synthesizes home-grown aluminium oxide templates that do not have any branched region. however, the uniformity of the cylinders obtained from aluminium oxide membranes in general is not as good as those obtained from track-etched polycarbonate membranes.

2.6 Template Preparation for Nanowire Electrodeposition

All NWs (gold and rhodium) were grown by electrodeposition in commercially available porous filter membranes as template. The commercial templates cannot be used "as-received". A certain preparation process is required to make the templates functional for NW growth. The preparation process includes contact layer coating, filling

the branched region if applicable, and sealing the pores to prevent leakage.

2.6.1 Contact Layer Evaporation

For the NWs to grow by electrodeposition, an electrical backing would be required to provide a working electrode. In order to make electrical contact, a silver layer, 500 nm thick was deposited on one side of the membranes. Figure 2.5 shows SEM images of a ~500 μm thick silver contact layer evaporated on one side of an anodized aluminium oxide template. The silver layer is broken as a result of SEM sample preparation for cross-sectional view.

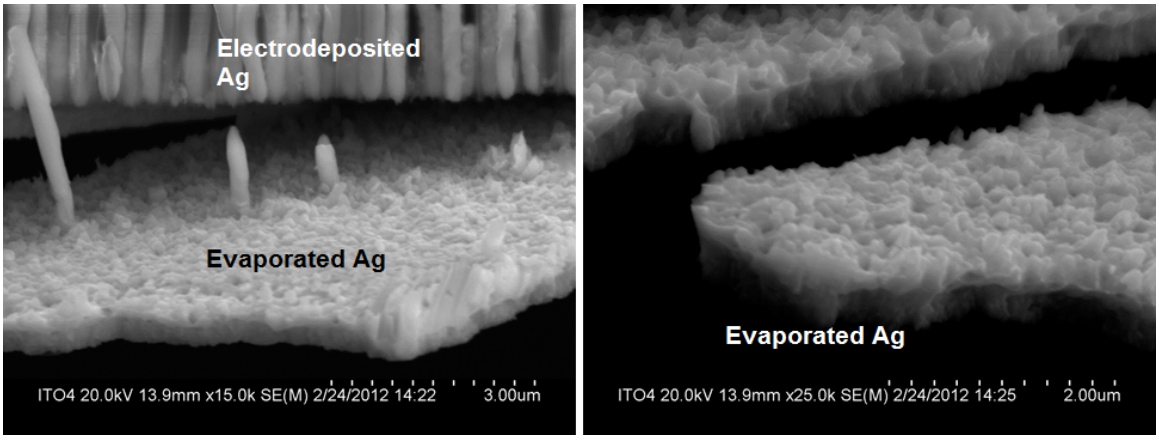

Figure 2.5: SEM images of an electron-beam-evaporated silver layer made as electrical contact for electrodeposition of NWs. The SEM sample preparation for cross-sectional view has broken the silver layer.

Early in this work, for the initial sets of experiments, a thermal evaporator was used to deposit the silver contact. The thermal evaporator, which is shown in Figure 2.6A, uses a tungsten boat for melting and evaporating silver pellets. More recently, a vacuum electron beam evaporator (Angstrom Engineering) was utilized, instead of the thermal evaporator, to fabricate the silver layer serving as the working electrode. The electron beam evaporator machine is shown in Figure 2.6B and C.

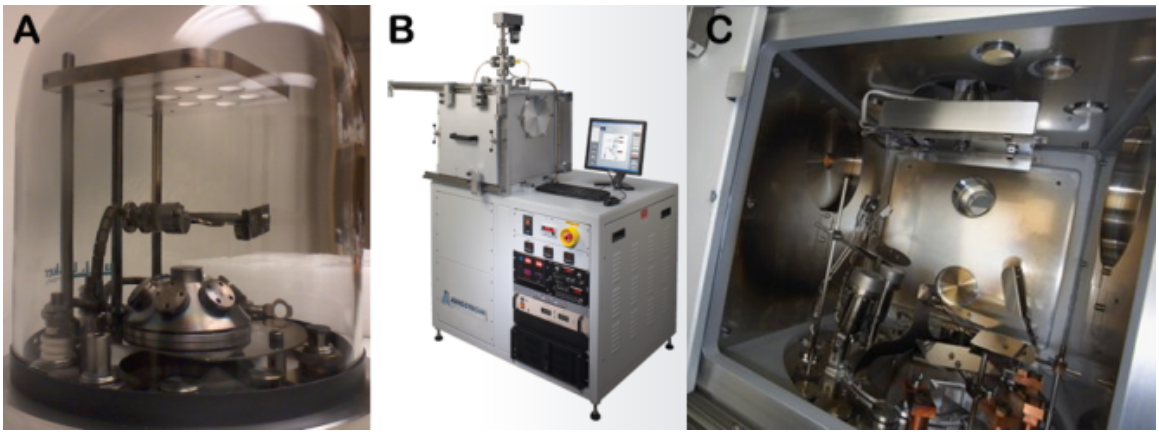

Figure 2.6: (A) Thermal and (B and C) electron beam evaporators used for fabrication of electrical contact layer. The contact layer is essential for transferring the electrical charge to the solution.

After the evaporation step, in all the experiments with the aluminium oxide membranes, silver was electrodeposited onto the branched region. This intermediate step was taken to electrodeposit silver into the highly branched pores of the anodized aluminium oxide membrane and fill the undesirable branched region. As shown in Figure 2.4A, a direct electropistition of gold or rhodium NWs in the branched region will result in wires interconnection and will not allow their separation upon removal.

Electrodeposition of silver was carried out at -500 mV potential versus the Ag/AgCl RE for one hour from commercially available Silver Cy-Less solution (Technic). Given the nominal pore density and average pore size, the nominal electroactive area of the silver electrode was calculated to be 1.385 cm^2 for anodized aluminium oxide templates. This calculation in case of polycarbonate membranes was not carried out, due to large uncertainties in the nominal pore density values.

Although the polycarbonate membranes do not have any branched region, the template preparation for polycarbonate templates also involves a sacrificial silver electrodeposition step prior to the gold or rhodium NW growth. The reason for this additional step is to prevent solution leakage related to an evaporation shortcoming. The leakage problem from polycarbonate membranes is discussed in section 2.6.3.

2.6.2 Uniformity of Evaporated Contact Layer

The uniformity of the evaporated electrical contact layer is important for various reasons. For instance, the uniformity of electrical current distribution in the elec-

trodeposition process, which determines the uniformity of NW growth, is a function of electrode uniformity. Also, if the thickness variation in the evaporated concat layer is large, the probability of having areas of membrane with insufficient metal coverage would be larger. Another issue with non-uniform evaporation is the development of an induced strain field in the evaporated film that can cause geometrical distortions in the template. A distorted template may not be adequately sealed in the electrochemical cell causing solution leakage or other secondary troubles.

For the evaporation process, an aluminium specimen holder was machined to hold the membranes in the evaporation chamber while exposing one face of the membranes for coating. The anodized aluminium oxide membranes are much harder and also thicker than polycarbonate membranes (60 μm compared to 6-25 μm). Therefore, the contact layer evaporation on aluminium oxide membranes is expected to be easier as they can resist the stress induced during the film growth without distortion.

However, silver evaporation on thin and soft polycarbonate membranes can be challenging as the material is not stiff enough to stand the stress induced during the evaporation process. Figure 2.7 shows an image of the polycarbonate membranes inside an evaporator holder after being coated with silver (intended thickness was $\sim$500 nm).

Figure 2.7: Soft and thin polycarbonate templates were curled during the silver contact layer evaporation step.

The thin and soft polycarbonate membrane gradually curled up as a result of the thin film evaporation strain. These membranes were non-uniformly coated due to the shadowing effects. In order to prevent the polycarbonate templates from folding

during the evaporation process, an O-ring was put on top of each template before the start of evaporation. Figure 2.8A shows the polycarbonate templates supported with the weight of an extra O-ring inside a holder.

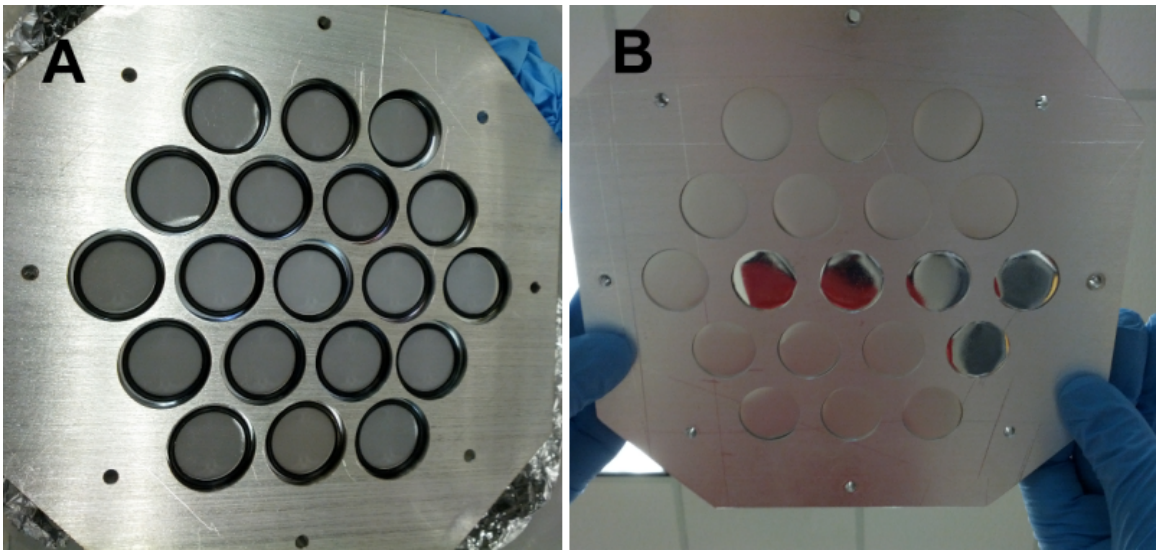

Figure 2.8: Images from the top and bottom of an evaporator specimen holder containing polycarbonate membranes coated with silver: (A) The weight of black O-rings provide sufficient mechanical support for keeping the membranes flat. (B) Silver-coated and flat polycarbonate membranes as-removed from the evaporator. Light reflection from the coated surface of some membranes suggests two distinctly different degrees of surface smoothness.

It turned out that the weight of an O-ring is sufficient for holding polycarbonate membranes flat during the entire evaporation process as shown in Figure 2.8B. The flatness of membranes is essential for obtaining uniform evaporated contact layer.

Figure 2.8(B) also revealed that the two sides of polycarbonate membranes are not identical. Mirror-like light reflection from five membranes (that were placed upside-down) compared to the matte reflections from the other membranes inside the holder, suggested the two sides of the polycarbonate membranes have distinct surface properties. For further explanation regarding the differnce between the two sides of the membranes see Figures B.6 and B.7 in Appendix B.

2.6.3 Leakage from Polycarbonate Membranes

For electrochemical deposition of NWs into a template material, a conductive layer must be coated on one side of the template to provide electrical contact and serve as cathode. As mentioned in section 2.6.1 this was regularly done by silver metal evaporation. We used an electron beam evaporation as well as thermal evaporation (only in the early stages of this work) for depositing the silver coat. Silver can be easily and selectively dissolved by nitric acid after the termination of NW synthesis. However, our SEM investigations on polycarbonate templates show that the evaporated silver layer, even after reaching a thickness of 500 nm, still has largely open pores in some regions. Figure 2.9 shows three SEM images of an evaporated silver layer on a polycarbonate membrane at three different locations of the template disk (spanning the disk center to the edge). Figure 2.9A, B and C are taken from a center region, a region in the middle of a center-to-edge line, and the edge of a silver-coated polycarbonate template, respectively. The template pores in the center region are almost closed, whereas the of pores in the edge region of the template disk are still, almost fully open. The pores located at the region between the center and the edge are partly open.

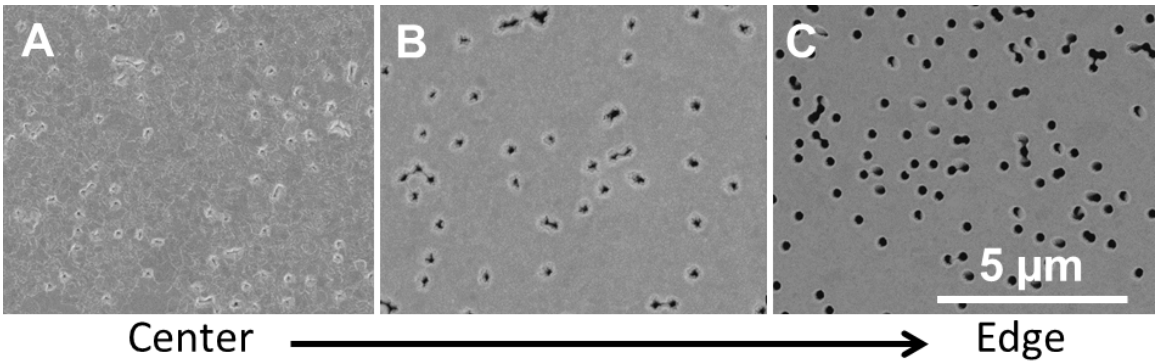

Figure 2.9: SEM images taken at three different locations, from the center to the edge of of a silver-coated polycarbonate template. The pore closure degree decreases from the highest value at the disk center to the lowest amount at the template edge.

Using templates with a notable fraction of open or partly-open pores, will be problematic in the electrochemical deposition process of nanomechanical resonators. Figure 2.10 schematically explains what would happen in the two cases where the membrane pores are effectively closed (A and B) and when they are not (C and D).

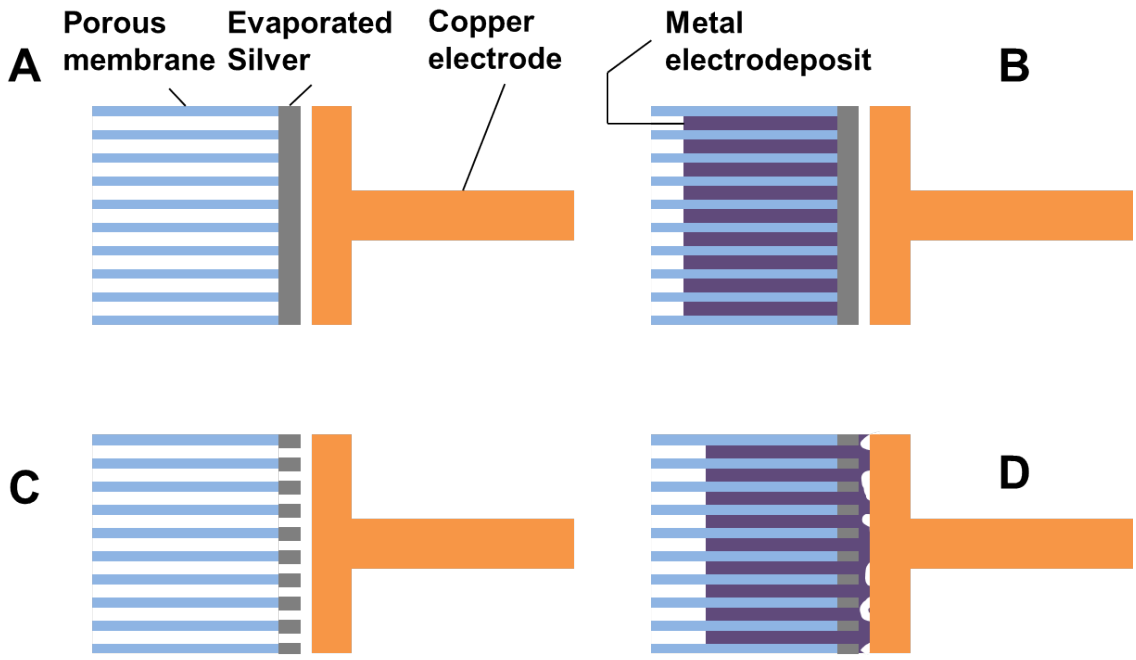

Figure 2.10: Schematic demonstration of electrochemical deposition process into nanoporous membranes when the pore are effectively closed (A and B) and when the pores are fully or partly open. A copper disk electrode is in contact with the evaporated silver layer to transfer the cathodic charge for NW growth. (A) When the pores of the membrane are effectively closed, the metal electrodeposit shown in (B), will only fill the empty pores. (C) When the membrane pores are open or partly open, the leakage of the electrolyte solution will wet the copper electrode as well as the back of the evaporated silver layer. Therefore, (D) the metal deposit will nucleate and grow on top the copper electrode and backside of the evaporated silver layer.

If the pores are not effectively closed, the electrolyte solution will leak out of the open membrane pores and come into contact with the copper disk electrode that supplies the potential from the potentiostat. The leakage would also wet the backside of the evaporated silver layer. Therefore, an attempt to deposit RhNWs into the template, will also create a rhodium film on top of the evaporated silver contact layer (Figure 2.10D).

This would cause a problem in the process of NW extraction where the rhodium film attached to the silver layer will remain intact upon exposure to the nitric acid. Figure 2.11 shows two polycarbonate template specimens with rhodium deposit inside that were left 2 minutes in 34% nitric acid for silver removal. After 2 minutes, the

specimen with effectively closed pores (left) is clean from silver and ready for the next step. However, the specimen with the pores not fully closed (right) is not cleaned and has a layer of rhodium and silver deposits on it (case of Figure 2.10C and D).

The intact rhodium metal deposits will crash in the centrifuge step and form relatively large particles mixed with RhNWs. Therefore, the batch of NWs obtained from this specimen will not be pure and clean causing a significant reduction in the yield of fabrication of functional resonator devices.

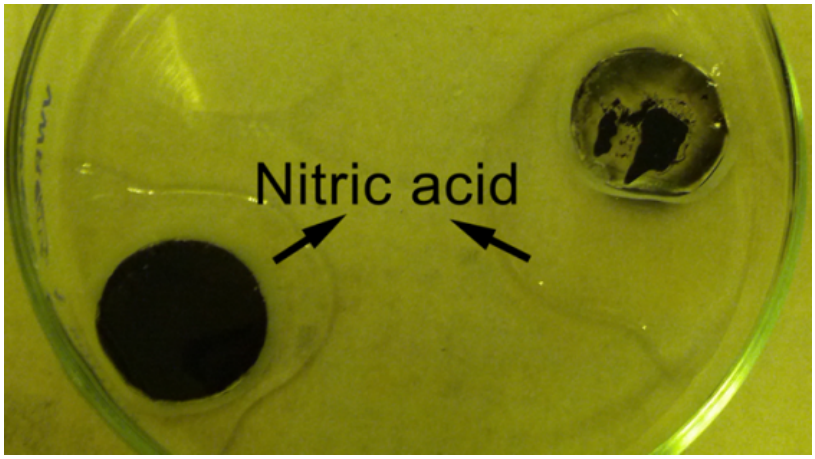

Figure 2.11: Two polycarbonate membranes after use for rhodium electrodeposition, are soaked for 2 minutes in 34% nitric acid to dissolve the silver layer. The template on the right was used as-evaporated. The pores of the specimen on the left have been closed by taking an extra step of silver electrodeposition.

Even when a polycarbonate membrane is well-supported in the evaporation chamber to remain flat, a notable fraction of pores will still be open to some extent and cause a leakage problem. In order to prevent NW electrolyte leakage and extract NWs without particle contaminants, the pores must be closed prior to NW electrodeposition. This can be done by a short-time (4 min at -500 mV vs RE) silver electrodeposition before rhodium or gold NW electrodeposition. The silver electrolyte will leak out of the pores and as a result some silver will be electrodeposited on top of evaporated silver and also partly into the nanopores. Eventually all the silver material (electrodeposited and evaporated) will be removed upon exposure to nitric acid. The only drawback of this extra step is that a part of "precious" nano-channels of the membrane will be occupied by silver and not available for NW growth. However, this loss can be minimized by choosing a just-enough (optimized) silver electrodeposition

time.

Chronoamperometric curves can be helpful for determining this optimized time of silver electrodeposition for closing the pores and preventing NW solution leakage. The chronoamperometry or current-time transient curves will be discussed in more depth in section (3.4.1). Figure 2.12 shows the current vs elapsed time curves for eight experiments of pore closing. Silver-evaporated polycarbonate membranes with nominal pore size of 400 nm were used under the same electrochemical conditions (-500 mV with respect to the RE). The current in all the curves begins to flatten after about 3 minutes and can be considered as almost steady after 4 minutes of silver electrodeposition. The steady current suggests reaching a stable electrodeposition condition with no considerable change in the electroactive area. This seems to be about the time that electrodeposition of silver is no longer continuing outside the pores as there is no unsteady current variation.

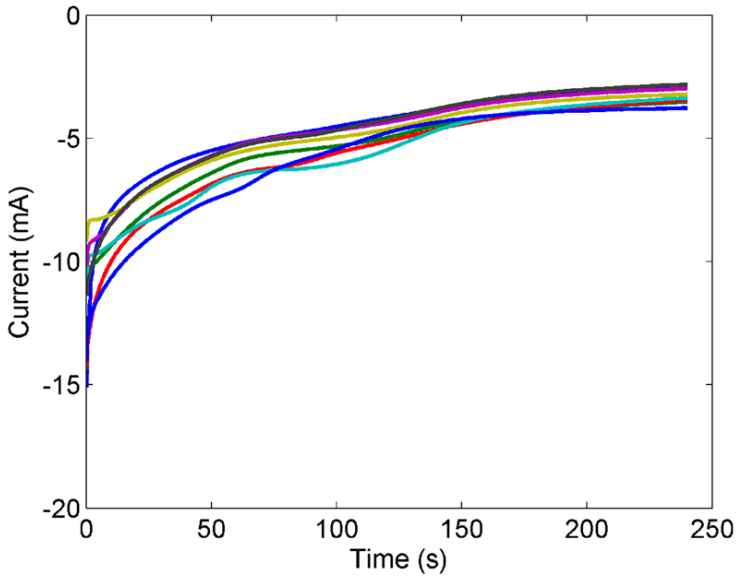

Figure 2.12: Transient current-time curves for pore-closing electrodeposition of silver into the PC400ST2525 membranes.

We have used 4 minutes of silver electrodeposition for this type of template as a standard step prior to NW deposition for all the NWs made in PC400ST2525[3] polycarbonate templates. Chronoamperometric curves are especially useful when working

[3]The list of all templates used in this work with their names and characteristics are given in Table 2.3.

with new templates or electrolyte solutions; or when working under a different electrochemical condition such as a different concentration, working potential, temperature, etc.

2.7 Templates Used in This Work

In this work both membrane materials discussed in section 2.5 have been used extensively. All the membranes were commercially produced and were purchased from three main manufacturers, namely, Whatman, Sterlitech and SPI Supplies. Table 2.3 summarizes the list of all template membranes used in this work[4]. The first two letters of each template name determines the material (AO for aluminium oxide and PC for polycarbonate). The material letters are followed by three digits for pore nominal size in nm; two letters for producers name (WT for Whatman, ST for Sterlitech and SP for SPI supplies); two digits for membrane thickness in μm; and finally, two digits for membrane disk diameter in mm. For instance, template PC400ST2525 is a polycarbonate membrane with nominal pore size 400 nm, produced by Sterlitech, 25 μm thick and 25 mm in diameter.

Table 2.3: List of all the templates used in this work for NW synthesis.

Template name	Material	Nominal pore size (nm)	Average NW diameter (nm)	Made by	Thickness (μm)	Circle diameter (mm)
AO200WT6025	Anodized aluminium oxide	200	250	Whatman	60	25
AO020WT6025	Anodized aluminium oxide	20	250	Whatman	60	25
PC400ST2525	Polycarbonate	400	450	Sterlitech	25	25
PC200ST1025	Polycarbonate	200	270	Sterlitech	10	25
PC010ST2525	Polycarbonate	10	40	Sterlitech	25	25
PC010SP0613	Polycarbonate	10	40	SPI	6	13
PC100WT2025	Polycarbonate	100	200	Whatman	20	25

[4]See Appendix B for pictures and ordering information.

All the membranes used in this work, except for PC010SP0613, were thin disks with diameter of 25 mm. This particular geometry is suitable for the main Teflon electrochemical cell particularly machined for this work (see section 2.2.4). The PC010SP0613, with 13 mm diameter, was used in another electrochemical cell described in the Appendix A.

The two anodized aluminium oxide templates AO200WT6025 and AO020WT6025 have nominal pore size of 200 and 20 nm, respectively. But, the pore size relevant to the NW synthesis for either of the two membranes were found to be the same and $\sim$250 nm. The reason is that these membranes are mainly intended to be used as filters and therefore, the nominal pore size reported by the manufacture is the pore entrance size designated for filtration purposes. Thus, the two membranes AO200WT6025 and AO020WT6025 are considered to have the same utility in the context of this work.

In general, the membranes with larger thickness (i.e., longer pores) are more desirable in this work because they could be used for making longer resonator wires. Longer wires are more useful due to the limitations in the resonator chip microfabrication process. NWs shorter that 9 μm have a very small chance of making a functional nanoresonator.

It must be noted that not the entire pore length would be used for NW synthesis. For reasons discussed in the previous sections, a portion of pore length is used for sacrificial silver electrodeposition. Also, a portion of the pore length on the top is left empty as a safety factor. If the pores get fully filled, the deposition of metal on the surface of membrane will connect the NWs and the entire batch will be become dysfunctional as NWs will not be separable. As a result, the membranes with small thickness ($<$20 μm) were less used for resonance NW fabrication.

Large pore size membranes such as 400 nm nominal diameter, are mainly used when long NWs are needed and the stiffness of NW is crucial. Small pore size membranes —specially those with 10 nm nominal size— have potential use in other works. For instance, they can be used for making nanoparticles to be used as catalyst or chemical sensor elements in applications such as fuel cells.

The polycarbonate membranes, in general, show entirely different structural features as compared to aluminium oxide membranes. Additionally, polycarbonate membranes manufactured by different companies show structural features that are different from those of made by other producers. Therefore, each of these membranes had to be used for several electrodeposition trials in order to identify their structure and suitability for NW resonator use.

The next two sections describe the structural characteristics of anodized aluminium oxide and track-etch polycarbonate membranes used in this work.

2.7.1 Structural Characteristics of Anodized Aluminium Oxide Membranes

Aluminium oxide is not electrically conductive and therefore direct imaging of the microscopic (and nanoscopic) structure of the anodized aluminium oxide membranes under the scanning electron microscope (SEM) is challenging (see section 3.3.1). The easiest and perhaps the most practical way of structural characterization of the template material is to image the metal electrodeposit that fills the membrane pores.

In this section, results showing a number of typical structural features common to the anodized aluminium oxide membranes will be discussed mainly based on the microscopic images obtained from the metal electrodeposit inside the pores. Anodized aluminium oxide membranes are very brittle and can be easily snapped apart by hand, without any cutting tools, to study their cross-section.

Figure 2.13A shows an SEM image taken from the top of an anodized aluminium oxide membrane. The pore structure is hexagonal and the pore density is relatively large compared to polycarbonate membranes. Figure 2.13B is taken from the cross-section of the membrane revealing the electrodeposited silver NWs on the bottom.

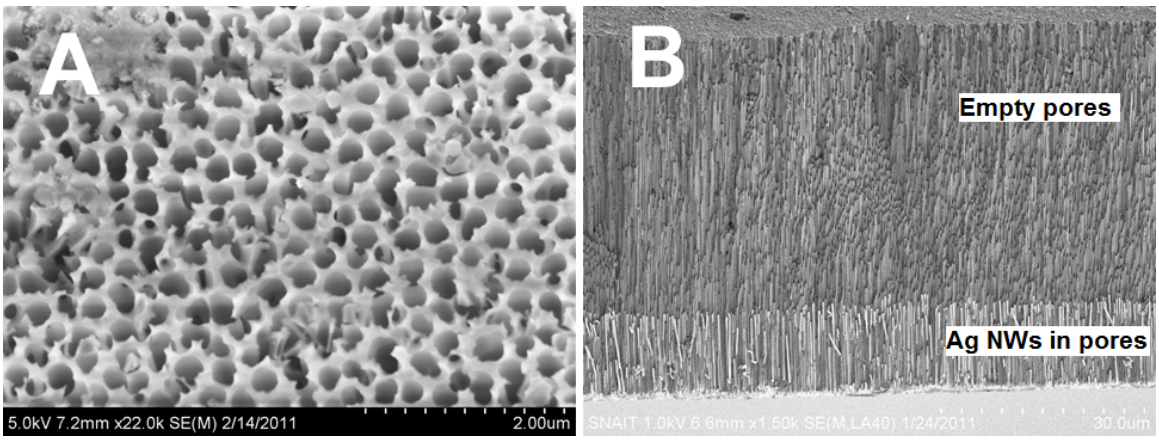

Figure 2.13: SEM image of (A) Top and (B) cross-sectional view of anodized aluminium oxide template AO200WT6025.

In section 2.5.2, the existence of a branched region in anodized aluminium oxide was explained. The term "branched region" is only used for a small region 3-5 μm

from one surface of the membrane, which is highly branched for filtration reasons. Our results obtained from scanning numerous anodized aluminium oxide membranes show that the branching is not only limited to the branched region but exists (less frequently) throughout the entire thickness of these membranes. Figure 2.14 obtained from a region close to the middle of an anodized aluminium oxide membrane, clearly shows the existence of the branches.

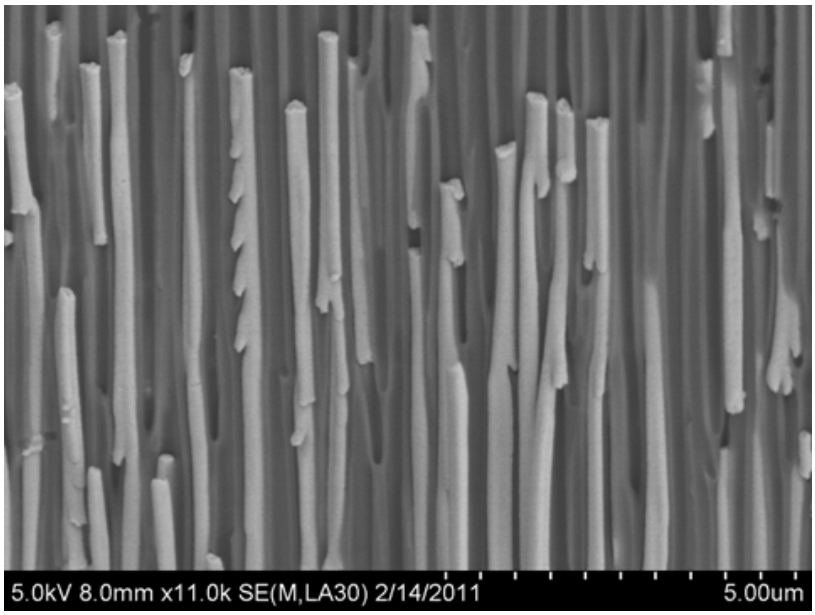

Figure 2.14: Electrodeposited silver inside the pores revealed that branching is not limited to the branched region and can be found throughout the entire thickness of anodized aluminium oxide membrane.

The existance of the branches in the areas of the pores that will be used for NW fabrication, will produce defected NWs that are not perfect cylinders. The deviation of NW shape from a perfect cylindrical shape is not only limited to the pore branching. Figure 2.15 shows SEM images of a number of defected NWs synthesized in an anodized aluminium oxide template. Many of the NWs seen in Figure 2.15 are branched but some of them show non-uniform diameter. The non-uniform diameter defect is another common problem in use of anodized aluminium oxide for resonator fabrication.

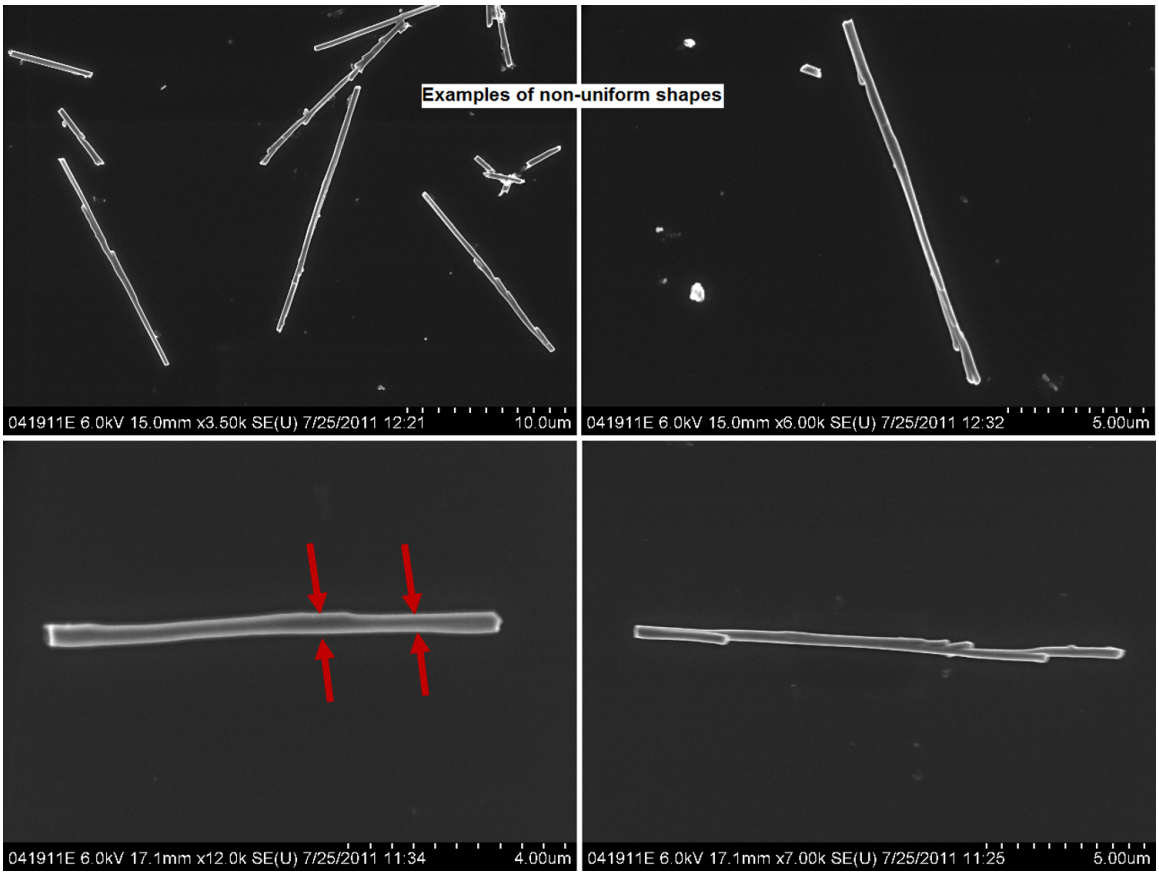

Figure 2.15: Typical NW defect mainly due to branching (not branched region) and non-uniform diameter of the anodized aluminium oxide membrane pores. Non-uniform diameter of NWs is not well-suited for resonance application.

Another less common defect found in anodized aluminium oxide templates is a deformed region as demonstrated in Figure 2.16. The pores in this deformed region are oriented at an angle from the usual vertical direction. The electrodeposited metal in these deformed zones produce small NW pieces and reduce the uniformity of NW length obtained from each batch.

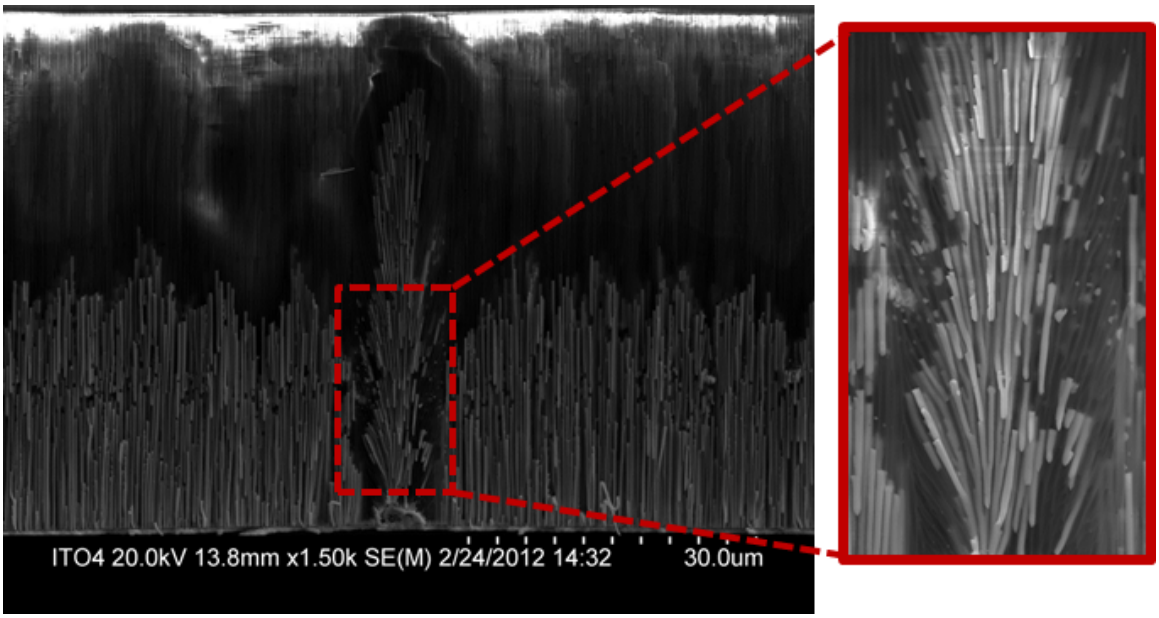

Figure 2.16: A deformed zone found in small fraction in anodized aluminium oxide templates.

2.7.2 Structural Characteristics of Polycarbonate Membranes

This section reviews the results obtained mainly from SEM images of NWs synthesized in the polycarbonate membrane. Many of the structural characteristics of polycarbonate membranes have been already discussed in section 2.5.1 with the reasons behind them. A general description of these structural features have been given in the literature by many (e.g., Martin [2]). However, in this work we have investigated all the structural defects in more depth, specifically in relation to nanoresonator fabrication.

As mentioned in Table 2.3, five different polycarbonate membranes were used in this work. The structural diversity among these five polycarbonate membranes is more pronounced as compared to aluminium oxide membranes. From the five polycarbonate membranes, PC010SP0613 and PC010ST2525 (nominal diameter=10 nm) were only used for synthesis of NWs and nanoparticles for applications other than nanoresonator. Also, PC200ST1025 was less useful for resonance NW fabrication due to the limitation of NW length. The use of PC100WT2025 was also limited due to more significant tapering defect observed in the NWs synthesized in this template.

The most frequently used polycarbonate template in this work was PC400ST2525

with 25 μm thickness allowing long NW growth and larger diameter providing higher stiffness to increase the chance of surviving the centrifuge and resonator preparation process.

As also mentioned in section 2.5.2, the lack of electrical conductivity in polycarbonate material, makes direct electron microscope imaging of the membrane difficult. Therefore, the easiest way to characterize the membrane is to explore the NW electrodeposits grown in these templates. Unlike aluminium oxide, the polycarbonate polymer is a very soft material and therefore, cannot be snapped apart by hand. Use of cutting tools for cross-sectional investigations is not easy either. Most readily available cutting tools such as surgery razors or scissors introduce a significant amount of deformation that will make the study of the structure very difficult. For these reasons, the results of structural studies are all based on SEM images obtained from the electrodeposits grown in polycarbonate membranes.

Figure 2.17 shows an SEM image of the top of a polycarbonate membrane coated with silver. The silver coating was performed to provide an electrical contact layer for electrodeposition, but, is also essential for high quality SEM imaging with no charging effects. Several important structural features of polycarbonate membranes can be identified from Figure 2.17. Firstly, the pore density of polycarbonate membranes is much less than the pore density of anodized aluminium oxide membranes (compared to Figure 2.13A). Secondly, the pores are not distributed uniformly. Thirdly, the pores are oriented at random angles and a considerable fraction of them are not vertical. Fourthly, some pores overlap. These characteristics are major sources of defects and low yield in NW synthesis process from polycarbonate membrane and need to be explored further.

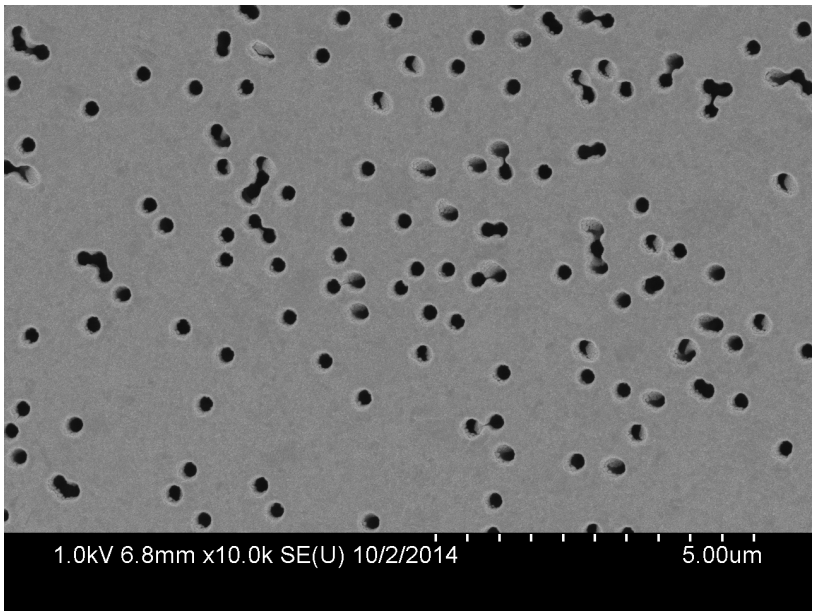

Figure 2.17: Top view of a silver-evaporated polycarbonate template used to estimate pore density and distribution.

In order to obtain structural information from more internal regions of the polycarbonate membranes, the templates were dissolved after NW growth inside the pores. Figure 2.18 shows the top view of NWs attached to the evaporated silver contact layer after dissolution of polycarbonate membrane. The dissolution process of polycarbonate membranes is discussed in details in Appendix C.2. The NWs angle clearly reveal the pore angles in all the directions. Although some overlap connections can be seen in Figures 2.17 and 2.18, it is not practical to estimate the degree of pore-overlap from these images since the three dimensional connections cannot be identified from the top view.

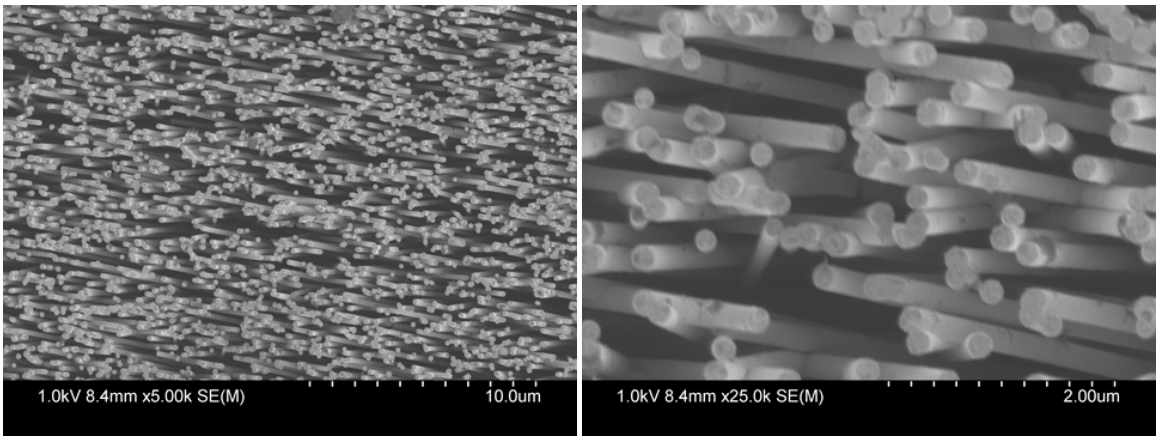

Figure 2.18: Top view of NWs after dissolving a polycarbonate template reveals pore angles and pore density. The image on the right shows a higher magnification for clarity.

In order to evaluate the structural connections between the pores in polycarbonate membranes, a batch of rhodium NWs grown in a membrane was extracted (extraction procedure is described in Appendix C) and dispersed on a Au-coated microscope slide. Under SEM, even at a low magnification, a number of large clusters made from connected NWs were observable. Figure 2.19 shows two clusters (top and bottom) of NW clumps found at two locations on the microscope slide. The inset shows a closer view of these pore connections and how it results in formation of NW clumps.

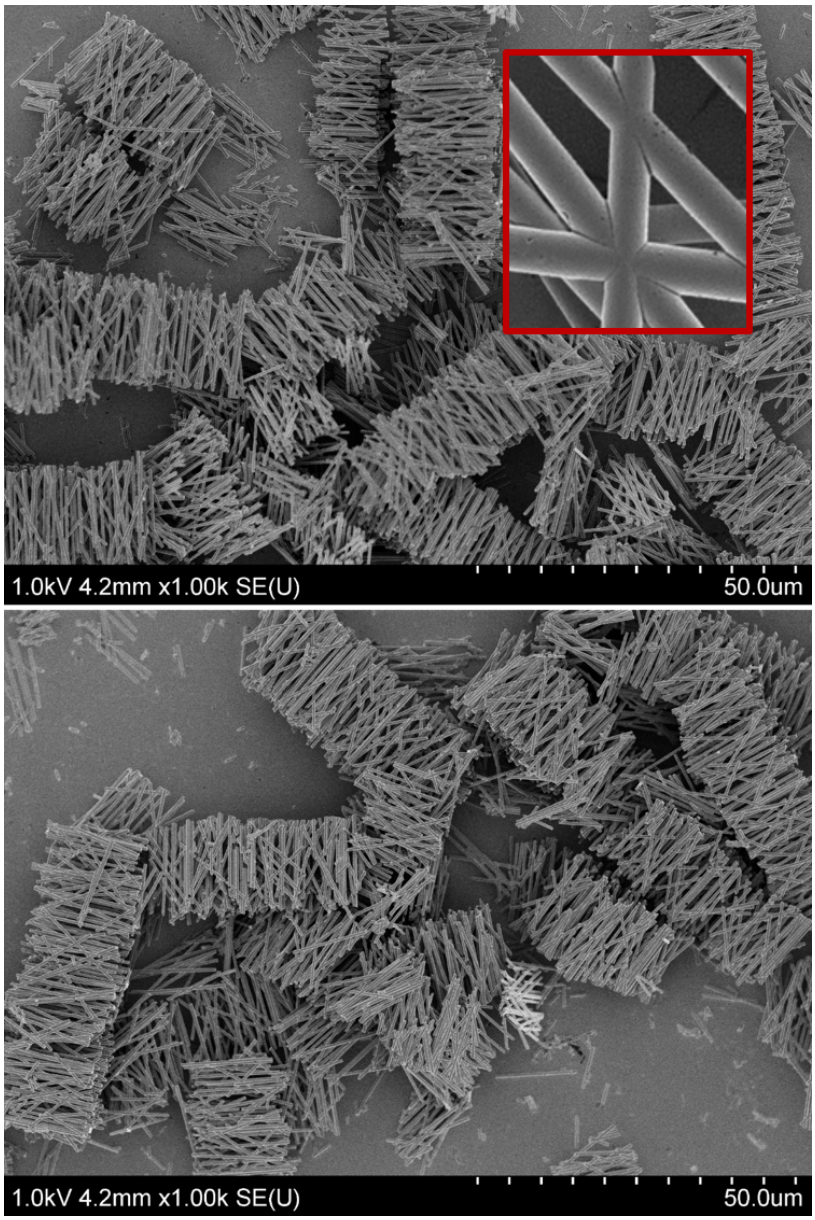

Figure 2.19: Numerous large NW clumps formation confirm systematic pore connections. The inset shows a closer view of these pore connections.

The large NW clumps show a specific repeated shape of connected NWs. This repeated pattern suggests the existence of a systematic connection between the pores of the polycarbonate membrane. The pore connection degree is high enough to permanently prevent separation of hundreds of NWs in each clump. This structural defect is perhaps the most significant problem associated with polycarbonate membranes for resonator synthesis.

Apart from the loss of many NWs for use as single resonators, the other aspect of this defect is making electrical shorts in microfabrication step (this will be discussed in Section 6.6). Briefly, when the NWs are dispersed on the chip for positioning, a number of these heavy clumps will remain present on the chip. Some of the clumps may be located in positions between gold pads or bars causing electrical shorts.

Another characteristic defect of polycarbonate membranes is the change in pore diameter (tapering). Figure 2.20 shows a long (∼13.5 μm) NW obtained from a PC100WT2025 membrane. The red arrows indicate a ∼40% change in the diameter of the NW between the two locations marked with the arrows. As discussed in section 2.5, the tapering defect is related to the fission fragments that create the pores. When tracks are being produced, secondary electrons are also generated, which contribute to the damage along the track, making some tracked areas larger in diameter than the others.

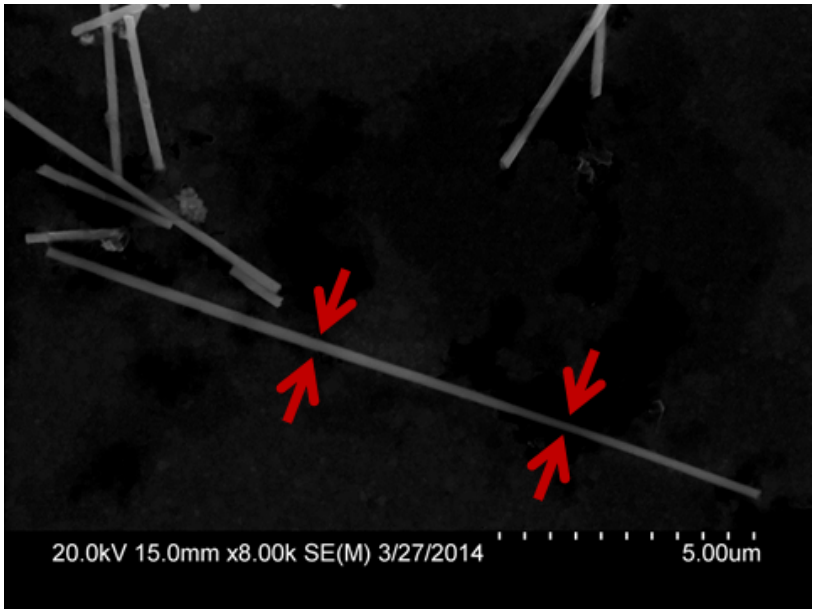

Figure 2.20: A ∼13.5 μm long, tapered NW synthesized in a PC100WT2025 template. The arrows indicate a change of ∼40% in the NW diameter between the marked locations.

Another reason for not using the PC100WT2025 template specifically in nanoresonator fabrication is that the high aspect ratio NWs made in these template have lower stiffness. Many single long NWs made in PC100WT2025 (see Figure 2.21) are bent after NW centrifugation and extraction step. The high aspect ratio NWs made

in PC100WT2025, compared to PC400ST2525, were found to be more vulnerable to the stresses induced in the centrifugation stage.

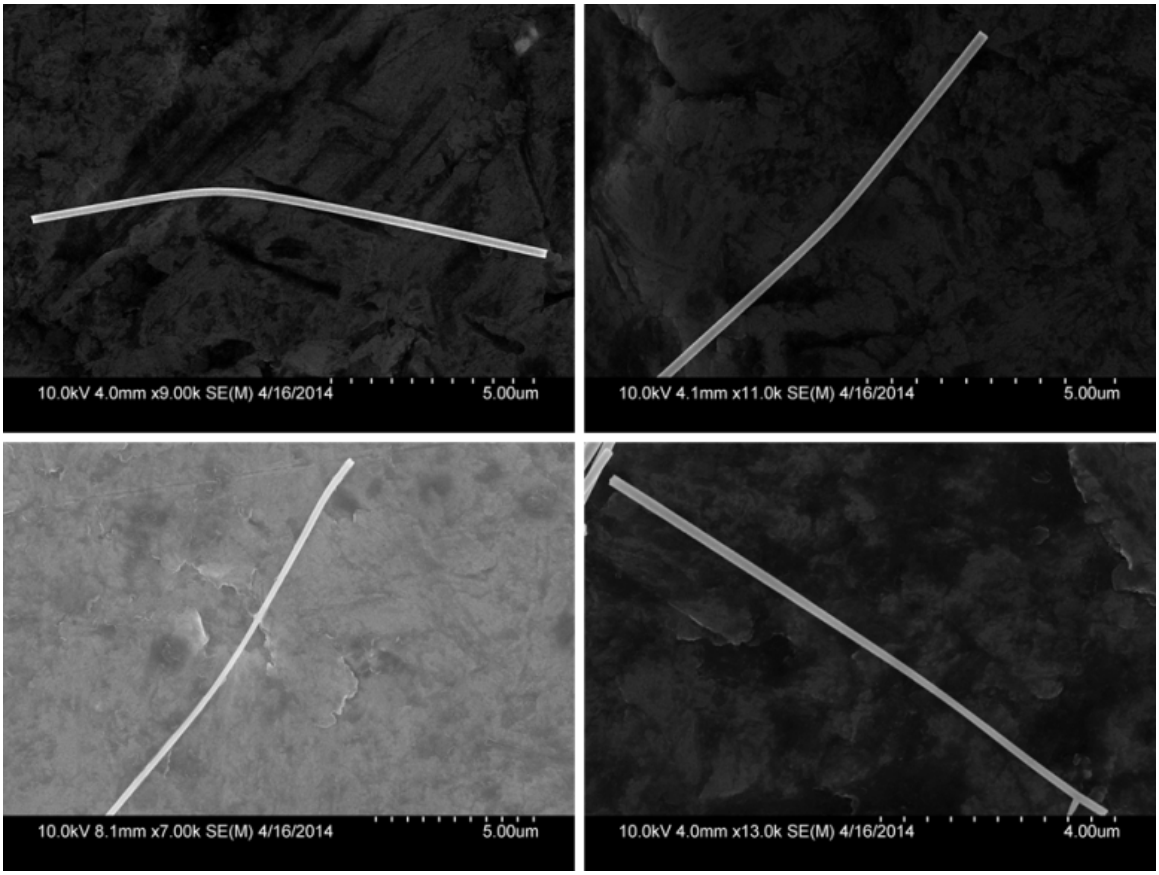

Figure 2.21: High aspect ratio single NWs made in PC100WT2025 template found to be mostly bent or folded after the centrifugation and NW extraction procedure, due to lower geometrical stiffness. Also, a considerable change in the diameter of some of the NWs can be observed.

In order to see the effect of NW aspect ratio on their mechanical resistance against the induced stresses in the centrifugation stage, several SEM images of NWs electrodesposited into PC010ST2525 template with nominal 10 and actual 40 nm diameter are shown in Figure 2.22. Although the 40 nm NWs made inside PC010ST2525 and shown in Figure 2.22 are shorter than the 200 nm NWs made inside PC100WT2025 shown in Figure 2.21, the 40 nm NWs are much more bent and folded than the 200 nm ones because their aspect ratio is higher. The average length:diameter aspect ratio of 200 nm NWs is $\sim$50 (10:0.2) compared to $\sim$175 (7:0.04) for 40 nm NWs.

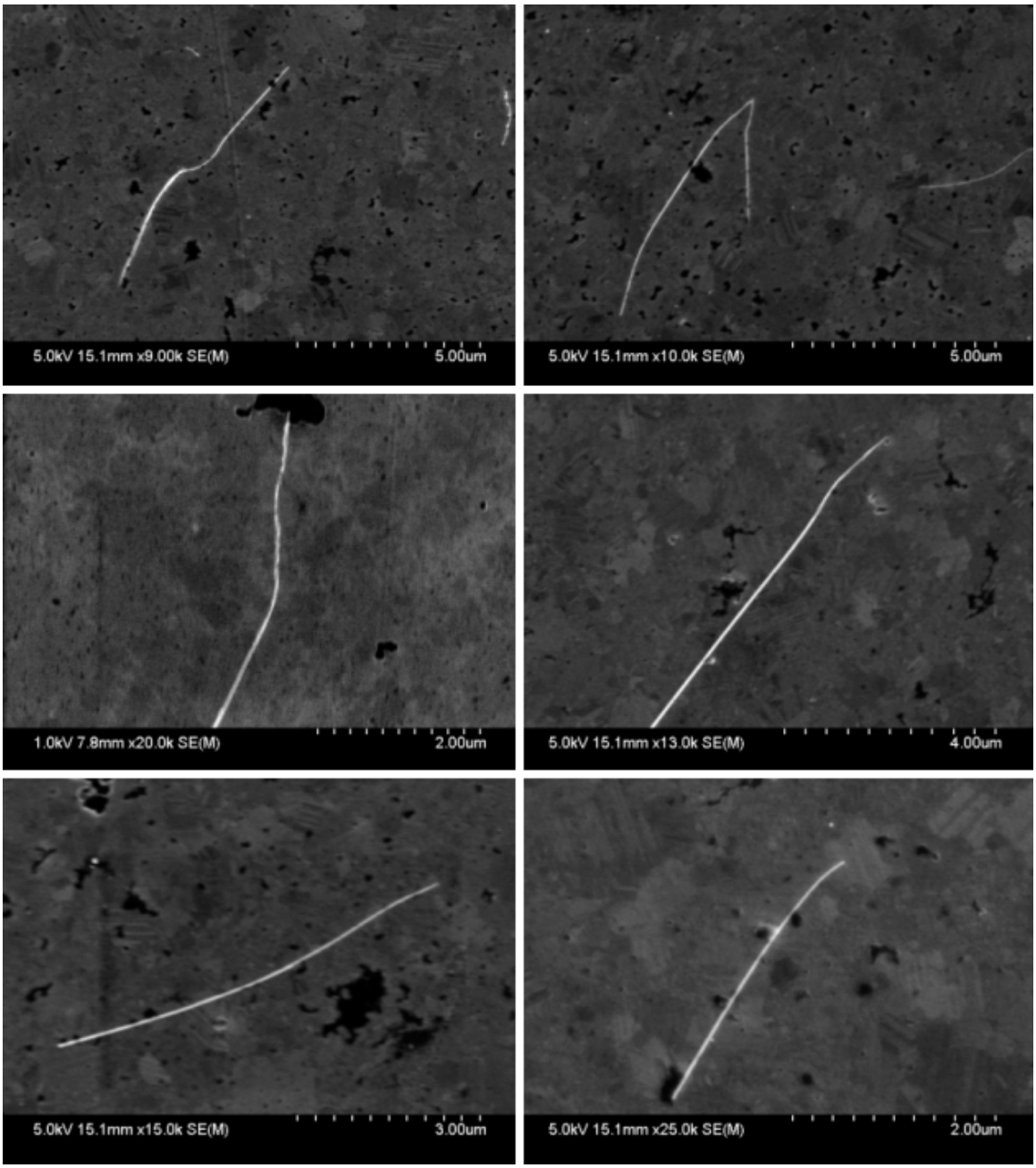

Figure 2.22: SEM images of RhNWs with average 40 nm diameter deposited into a PC010ST2525 template (nominal diameter 10 nm). NWs are highly bent and folded after centrifugation and NW extraction process and therefore, not suitable for cantilevered resonance application.

NWs made inside PC400ST2525 template with length:diameter aspect ratio of 20-35 have repeatedly shown high enough mechanical resistance to the stresses induced

during NW extraction (centrifugation) stage. Figure 2.23 shows images of four single NWs made inside PC400ST2525 with the diameter of ∼450 nm and length of >10 μm. These NWs are straight and long enough to make nanoresonator device.

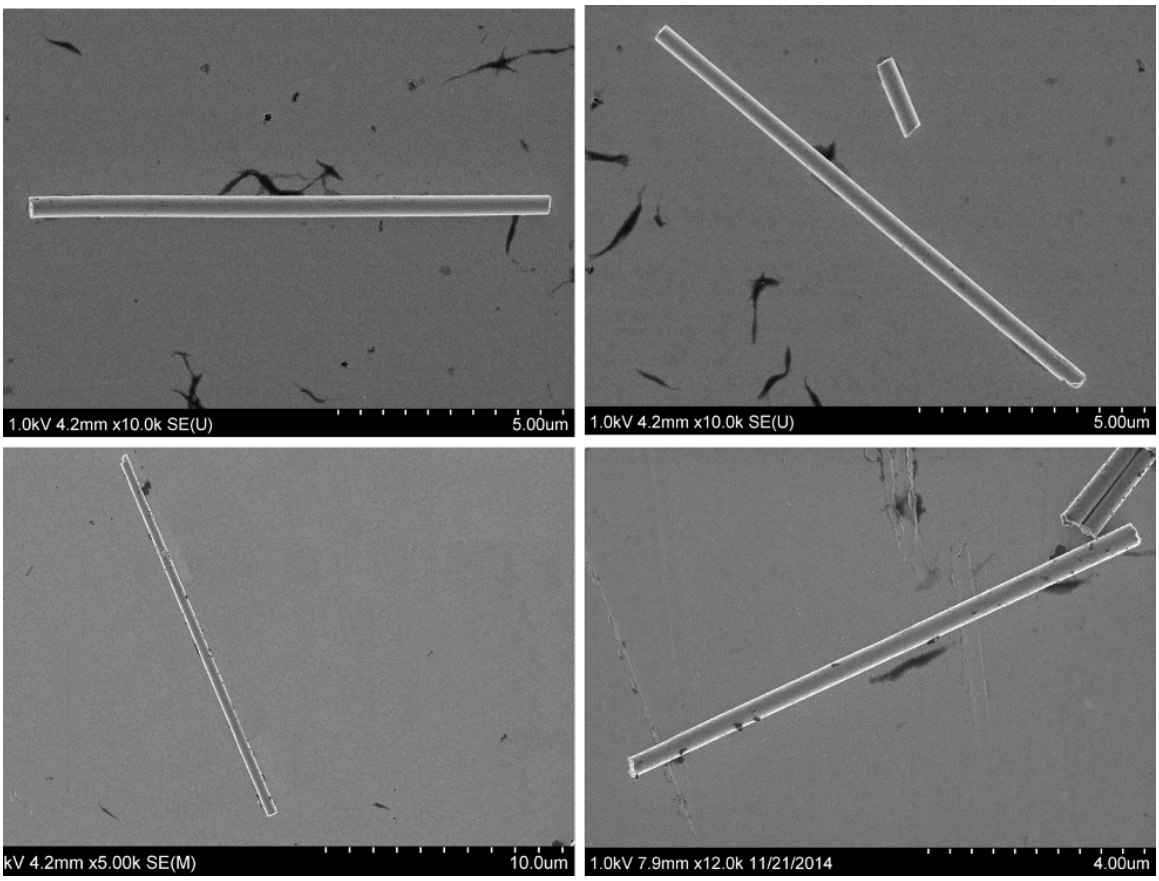

Figure 2.23: NWs made inside PC400ST2525 show high geometrical stiffness and can mechanically resist stresses induced during the centrifugation stage. These NWs are 10, 11.5, 12 and 16 μm long and not bent.

Considering the structural characteristics of polycarbonate membranes used in this work and their characteristic dimensions, the PC400ST2525 seems to be the most suitable one for making nanoresonator devices. However, the main structural defect of pore connections still remains an efficiency issue in the NW synthesis and device fabrication work. For straight and cylindrical NWs, the template synthesis yield efficiency depends on the ratio of single NWs to the NWs clumped by pore connections. Figure 2.24 shows two SEM images of dispersed NWs on a substrate that represent the regions with average mixture of single and clumped NWs regularly made inside PC400ST2525 template.

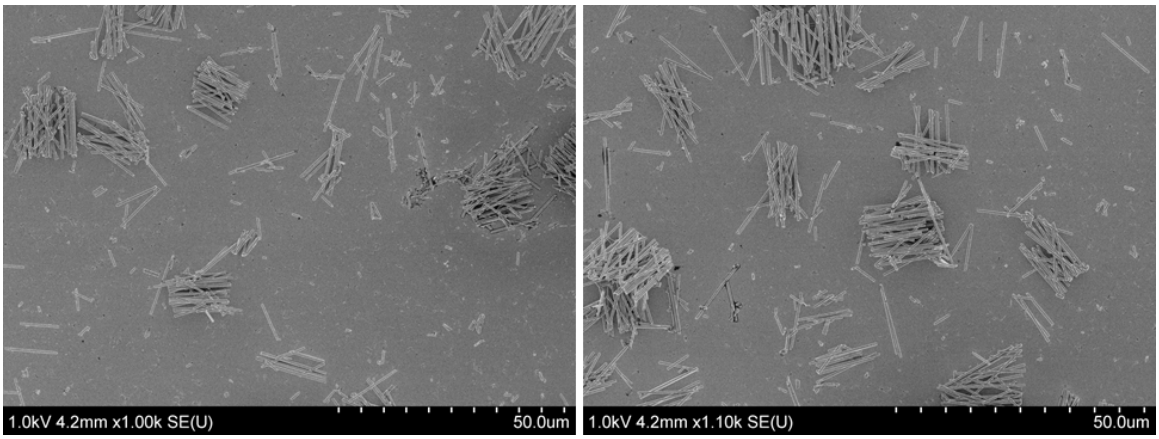

Figure 2.24: A small fraction of NWs obtained from PC400ST2525 template are single and therefore, can be used as resonators.

Figure 2.24 suggests that a particle filtration method would be required to increase the single NW yield efficiency. This has been addressed in a manuscript prepared through a joint work with my colleague Amin Ebrahiminejad.

2.8 A Critical Comparison of Templates

Anodized alumina pores are much more packed (higher pore density) and all aligned in the normal direction to the membrane disk plane. In the case of polycarbonate, not all the pores are aligned in the same direction. Moreover, the polycarbonate membrane pores show a much higher degree of cylindricity. There is one major problem associated with the use of each type of these templates for nanoresonator synthesis. NWs grown in commercially made anodized alumina are branched and not perfect cylinders. Although there is a branched region known for filter purposes close to the membrane surface, there are other random branching and pore distortions throughout the membrane. The main problem with polycarbonate membrane is that the numerous pore intersections make many groups of bundled NWs forming big clumps. The presence of these clumps can be an issue in the chip assembly process where the blocks bridge the pads and create short circuits. This will interrupt the NW dielectrophoretic positioning as well as the electrical drive for resonance frequency measurements.

Although single NWs grown from polycarbonate membrane have much higher quality (no-branching and better cylindricity), their fraction in a NW batch is much

smaller than single NWs obtained from the anodized aluminium oxide membrane. Therefore, further processes such as particle separation and enrichment methods are being investigated for high yield NW resonator chip fabrication.

When the overall yield of NW assembly on a chip device is mainly concerned, anodized aluminium oxide might be a better choice as it provides a much larger number of single NWs (also higher fraction in a batch of NWs). The pore cylindricity and the percentage of branch-free pores of these membranes can be improved by home-growing or getting an industrial manufacturer to produce special-order packs for these purposes.

Anodized aluminium oxide membranes are also a good choice for applications other than resonator devices. One of the main uses of gold and silver NWs made in this PhD work was in NW chaining project for production of highly-conductive transparent electrodes for photo-voltaic systems, included in the PhD work of Mahshid Sam in our laboratory.

When the total number of successfully assembled NWs on a chip device is not the most important criterion, the polycarbonate membrane can provide the best quality of NW on a nanomechanical resonator device. These devices are usually made for studying rarefied gas dynamics and other fundamental fluid mechanics problems. However, for the case of sensor devices such as hybrid multiplexed biosensor chips for early-stage cancer detection [8], the commercially available polycarbonate membranes as they are, may not be the best choice. The main reasons are low yield of single NWs and the presence of clump-making pore interconnections. It is possible and desirable to create a custom-made polycarbonate membrane by use of nuclear filters in a way that all the pores will be track-etched in one direction (with minimal angle scatter) so that the pore connections are minimized.

In summary, each membrane material, as they are currently available, can be useful for specific application or goal. For the main focus of this work, being the study of the effect of material electrochemical synthesis conditions on the mechanical properties of NW resonators, polycarbonate membrane was chosen. Although the yield of production may not be the best, this choice enables fabrication of highly-cylindrical NWs for reliable resonance measurement and deduction of material mechanical properties.

2.9 Conclusions

Electrochemical deposition was used as a low-cost and simple technique to make cylindrical and separable gold and rhodium NWs in porous membranes as template. Various commercially-made anodized aluminium oxide and track-etched polycarbonate membranes were used as template for NW electrochemical synthesis.

The NW templates were prepared by evaporation, coating one side of the membranes with silver to serve as an electrical contact layer (working electrode connection). Also, prior to the NW electrodeposition, extra silver was electrodeposited into all the template materials for different reasons. In the case of anodized aluminium oxide membranes, silver was electrodeposited to fill the branched region of the membrane preventing NW connections. In the case of polycarbonate membranes, the silver electrodeposition was carried out to close the open pores that were not closed in the evaporation stage. This prevented NW solution leakage from the open pores and helped obtaining a clean and pure batch of NWs.

The structural characteristics of different membrane products with various pore size, pore density, and membrane thickness were explored, mainly by looking at the metal electrodeposits obtained from them. The SEM characterization of metal electrodeposits revealed existence of several structural defects in the polycarbonate and aluminium oxide membranes. The most significant characteristic defect of the polycarbonate membranes was the presence of numerous pore interconnections creating NW clumps. Also some types of polycarbonate membranes were found to have tapered pores creating NWs with non-uniform diameters.

The main issue with commercially-produced anodized aluminium oxide membranes was found to be pores with distorted geometries and random branching outside the branched region. This defect creates NWs with non-uniform shapes and more geometrical uncertainties. However, single NWs made inside the PC400ST2525 polycarbonate membranes were found to be high-quality, straight cylinders for cantilevered resonator application. On the other hand, a higher fraction of NWs made inside anodized aluminium oxide templates were single and easily separable, making them more suitable for other applications such NW chaining for transparent electrodes in photovoltaic systems.

It should also be noted that despite the existence of defects in these membranes, they had successfully served as useful templates for studying the nucleation and growth of NWs under various electrochemical conditions used for altering the me-

chanical properties of NW resonators. The presence of defects is not a fundamental obstacle and can be solved by small changes in their manufacturing process. Therefore, the results of this PhD work will be essentially valuable to the future templated NW electrodeposition.

2.10 Future Work

Several routes can be taken to improve the templates used for electrochemical synthesis of the NWs, by removing or reducing the structural defects mentioned in this chapter. Given the need for costly track-etching equipments and the technical difficulties, home-growing the polycarbonate templates does not seem to be a practical way to make defect-free templates. Since the track-etching and anodization processes have been far industrialized, working with the manufacturers through collaborative projects might be a more reasonable choice. Alternatively, some manufacturers such as Sterlitech, seem to be ready to accept special orders for making specific types of the membranes (costs estimate ranging 3000-10000 CAD for a pack of 500 membranes from telephone conversation with Sterlitech technical staff).

Development of efficient and simple filtration systems for separating large NW clumps from the single ones might be a short-term solution to the low yield of single NWs from the polycarbonate templates.

In the template preparation work, use of sputtering instead of evaporation is likely to improve the pore closing power of the silver contact layer. Another method to significantly reduce the number of open pores in silver evaporation step could be use of an angled spinning evaporation method for leakage free fabrication of the contact layer. Angled evaporation is more likely to close the membrane pores by side-filling. Employment of this method requires some modifications in the evaporator specimen holding setup.

Chapter 3

Electrochemical Nucleation and Growth

This chapter provides introductory background and preliminary results on electrochemical nucleation and growth of metals from aqueous solutions. The information provided in this chapter will also serve as a basis for the nucleation and growth of clamp deposit for cantilevered NWs. The results on the electrochemical nucleation and growth of clamp material will be presented in Chapter 6.

Nucleation and growth of rhodium under various electrochemical conditions and from different solution chemistries is presented separately in Chapter 5.

3.1 Nucleation and Growth

Crystal formation during the formation of 1D nanostructures is the essence of their synthesis procedure. A new solid phase evolves from another phase, starting with a fundamental step of *nucleation*. In the second step, the crystalline solid formation continues by a *growth* mechanism. Although crystallization has been investigated for years, very little is known quantitatively about this process, especially at smaller scales [34].[1]

Unlike a bulk material, the kinetics and thermodynamics of crystal formation are complicated in the nanoscale regime where high surface-to-volume ratios increase the

[1] One of the well-known mechanisms especially for formation of single-crystal NWs and nanotubes is "screw-dislocation-driven" growth, where the axial screw dislocations provide self-perpetuating steps to enable 1D crystal growth [35]. This mechanism was mainly proposed for single-crystal NW growth relevant to CVD methods.

importance of surface energy considerations. Metal nanoparticles can accommodate relatively high amount of strain by developing irregular polycrystalline structures and lattice defects [36] resulting in exceptional mechanical, physical and chemical properties.

When a metal is immersed into a solution containing ions of that metal, equilibrium is set up between the tendency of the metal to enter solution as ions and the opposing tendency of the ions to lose their charge and deposit on or in the metal. Depending on the conditions of the system, this can occur in either direction. At equilibrium, the driving forces for metal ions being discharged and metal atoms being ionized are equal.

The potential difference between the metal and the solution phases under these conditions is the equilibrium potential difference. The equilibrium electrode potential is the electrical potential of an electrode measured against an RE when there is no current flowing through the electrode. It is also called open circuit potential (OCP) [16].

The equilibrium potential between a metal and a solution of its ions is given by the Nernst equation (3.1).

$$E = E^0 + \frac{RT}{zF} \ln a \tag{3.1}$$

In Eq. 3.1, E^0 is the standard electrode potential, which is a constant characteristic of the material of the electrode; R the universal gas constant[2] (8.3143 J/K·mol); T the absolute temperature (K); F the Faraday constant (96485 C/mol); z the valence change (positive for cations that reduce at the cathode and negative for anions that oxidize at the anode); a the activity of the metal ion. In approximation, for dilute solutions, the concentration of the metal ion can be used instead of the activity.

The equilibrium is dynamic with metal ions being discharged and metal atoms being ionized, but these two effects cancel each other and there is no net change in the system. For the realization of metal deposition at the cathode, the system must be moved away from the equilibrium condition. An external potential must be provided for the useful electrode reactions to take place at a practical rate.

Overpotential is the difference between the equilibrium potential of an electrode (half-cell reaction) and its operating potential when a current is flowing. The overpotential represents the extra energy needed to force the electrode reaction to proceed at

[2] $R = k_B N_A$, where k_B is Boltzmann's constant and N_A is Avogadro's number.

a required rate (or, equivalent current density). Consequently, the operating potential of an anode is always more positive than its equilibrium potential, while the operating potential of a cathode is always more negative than its equilibrium potential.

The overpotential increases with increasing current density. The value of the overpotential also depends on the inherent speed of the electrode reaction. A slow reaction (with small exchange current density[3]) will require a larger overpotential for a given current density than a fast reaction (with large exchange current density). Overpotential is also referred to as polarization of the electrode.

An electrode reaction always occurs in more than one elementary step, and there is an overpotential associated with each step. Even for the simplest case, the overpotential is the sum of the concentration overpotential and the activation overpotential. The activation potential is the potential difference above the equilibrium value required to produce a current that depends on the activation energy of the redox event. Concentration overpotential spans a variety of phenomena that involve the depletion of charge-carriers at the electrode surface. Bubble overpotential is a specific form of concentration overpotential in which the concentration of charge-carriers is depleted by the formation of a physical bubble. The diffusion overpotential can refer to a concentration overpotential created by slow diffusion rates.

Overvoltage is the difference between the cell voltage (with a current flowing) and the open-circuit voltage (OCV). The overvoltage represents the extra energy needed to force the cell reaction to proceed at a required rate. Consequently, the cell voltage of an electrolytic cell is always more than its OCV, while the cell voltage of a galvanic cell (e.g., a rechargeable battery during discharging) is always less than its OCV. Occasionally, it is also referred to as polarization of the cell. The overvoltage is the sum of the overpotentials of the two electrodes of the cell and the ohmic loss of the cell. Unfortunately, the terms overvoltage and overpotential are sometimes used interchangeably [16].

According to the theory of nucleation [37] for electrochemical systems, the size and number of nuclei depend on the overpotential (η). In the electrochemical version of Kelvin equation, r is the critical nucleation radius and σ, V, z are specific surface

[3]In electrochemistry, exchange current density is a parameter used in kinetic expressions such as Tafel and Butler-Volmer equations. The exchange current density is the current in the absence of net electrolysis and at zero overpotential. The exchange current can be thought of as a background current to which the net current observed at various overpotentials is normalized. For a redox reaction written as a reduction at the equilibrium potential, electron transfer processes continue at electrode/solution interface in both directions. The cathodic current is balanced by the anodic current. This ongoing current in both directions is called the exchange current density.

energy, atomic volume in the crystal, number of elementary charges (e_0), respectively:

$$r = \frac{2\sigma V}{ze_0|\eta|} \tag{3.2}$$

The critical nucleation radius is the cluster radius below which a phase or solid cluster is not stable and will not grow. The most important term in Eq. 3.2 is η that can be simply adjusted to reduce the critical radius r and therefore, lower the nucleation energy.

The first theoretical interpretation of the electrochemical crystal growth in terms of atomic models considered the substrate as a perfect crystal surface. Those perfect surfaces do not have sites for growth and therefore nucleation has to be the first step. It is known that real crystal surfaces have imperfections and a variety of growth sites. This consideration introduced a major change in the theoretical interpretation of the deposition process and resulted in a series of new models [1].

3.1.1 Formation and Growth of Adion Clusters

In the formation and growth of adion clusters, two processes are of fundamental importance: (1) the arrival and adsorption of ions (atoms) at the surface, and (2) the motion of these adsorbed ions (adions, adatoms) on the surface. An adion deposited on the surface of a perfect crystal stays on the surface as an adion only temporarily since its binding energy to the crystal surface is small. It is not a stable entity on the surface, but it can increase its stability by formation of clusters. The free energy of formation of a cluster of N_i ions, $\Delta G(N_i)$, has two components:

$$\Delta G(N_i) = -N_i z e_0 |\eta| + \phi(N_i) \tag{3.3}$$

The first term in Eq. 3.3 is related to the transfer of N_i ions from the solution to the crystal phase and the second term, $\phi(N_i)$, is the energy needed to create surface for the new cluster. This increase in the energy due to creation of new surface is equal to the difference of the binding energies of N_i bulk ions and N_i ions as arranged on the surface of the crystal [1].

Both terms in Eq. 3.3 are functions of the number of atoms in the cluster, N_i, and hence the cluster size.

3.1.2 Creation of Surface Nuclei

The nucleation law for a uniform probability with time t of conversion of a site on the metal electrode into nuclei is given by:

$$N = N_0(1 - \exp(-At)) \tag{3.4}$$

where N_0 is the total number of sites (the maximum possible number of nuclei on the unit surface) and A is the nucleation rate constant. Eq.3.4 represents the first-order kinetic model of nucleation [1]. There are two limiting cases for this equation at the initial stages of nucleation (small t). First, in the limit of large nucleation constants A such that $At >> 1$, Eq. 3.4 reduces to:

$$N \simeq N_0 \tag{3.5}$$

indicating that all electrode sites are converted to nuclei instantaneously. Thus, this is referred to as *instantaneous nucleation*. Second, in the opposite limit of small nucleation constant for small A such that $At << 1$, Eq. 3.4 reduces to Eq. 3.6 by a Maclaurin expansion of the exponential term.

$$N \simeq N_0 At \tag{3.6}$$

In this case, the number of nuclei N grows linearly with time t and the nucleation is termed *progressive*.

In many electrochemical systems, it is possible to distinguish between these two modes of nucleation experimentally, such as by use of potentiostatic current-time transients.

3.1.3 Growth of Surface Nuclei

In the initial stages of growth of the nuclei, it can be assumed that nuclei grow independent of each other. However, in succeeding stages, it is necessary to consider the effect of the overlap between the diffusion fields around growing nuclei. The result of this overlap is the development of local concentration and overpotential distribution in the neighborhood of the growing nuclei. Overlap areas are zones of reduced concentration and reduced nucleation rate. Growing nuclei cannot grow freely in all directions since they will impinge on each other. The growth will stop at the

point of contact, resulting in a limitation in the size of the growth center.

When the charge transfer step in an electrodeposition reaction is fast, the rate of growth of nuclei crystallites is determined by either of two steps: (1) the lattice incorporation step or (2) the diffusion of electrodepositing ions into the nucleus (diffusion in the solution). In order to study the first case, simple models of nuclei are usually considered such as 2D cylinder, 3D hemisphere, right circular cone and truncated four-sided pyramid. The diffusion of ions are usually described using Fick's laws.

The early stages of electrochemical phase transformations are usually associated with two- or three-dimensional nucleation processes. The rate and hence the number of nuclei so formed, are strongly dependent on the overpotential. Thus, the relationship between the overpotential and the kinetics of nucleation is significant and should be established by either direct microscopic observation of the electrode or by indirect procedure of relating the current to the electroactive surface area and to the total number of nuclei.

In many cases of metal electrodepositon from aqueous solutions, the charge transfer step is found to be fast and the rates of growth of mature nuclei are well described in terms of control by mass-transfer of electrodepositing ions to the growing centers [38].

3.1.4 Nucleation and Growth from Aqueous Solution

In the electrodeposition of metals, generally a metal ion is transferred from the solution into the ionic metal lattice. The reaction is accompanied by the transfer of electrons from an external electron source (e.g. potentiostat) to the electron gas in the metal.

Surfaces may be divided into ideal and real. Ideal surfaces exhibit no surface lattice defects such as vacancies, impurities, grain boundaries, dislocations, etc. Real surfaces have a variety of defects. While an ideal surface is atomically smooth, the real surface may have steps, kinks, vacancies and cluster of adatoms. The defects especially kink sites, play an important role in any nucleation process including electrochemical nucleation.

The atomic processes that make up the electrodeposition process, can be viewed considering the structure of the initial (solution) and the final state (lattice). Since the metal ions are in an aqueous solution, they are hydrated. Therefore, the structure of the initial state in Eq. 2.1 should be represented in by $[M(H_2O)_x]^{z+}$ instead of

M^{z+}. The structure of the final state is an M adion (adatom) at a kink site, since it is generally assumed that atoms (ions) are attached to a crystal via a kink site [39]. Thus the final step of the overall reaction is the incorporation of the M^{z+} adion into the kink site:

$$[M(H_2O)_x]^{z+}(solution) \longrightarrow M^{z+}(kink). \tag{3.7}$$

The growth form (i.e., the microstructure development) depends on the working potential of the cathode (overpotential) [39]. This stems from the competition between nucleation and growth processes being strongly dependent on the working overpotential. The effect of working potential on the structure of electrodeposit will be shown at several sections of this dissertation.

Another important phenomenon related to the electrodeposition from aqueous solutions is the hydrogen evolution reaction due to presence of hydrogen ions. Section 3.1.5 introduces the hydrogen evolution phenomenon.

3.1.5 Hydrogen Evolution from Aqueous Solutions

A hydrogen evolution reaction is the production of hydrogen gas through the reduction of hydrogen ions in the solution. Hydrogen evolution is a significant side reaction in the electrodeposition of metals from acidic aqueous solutions such as rhodium solution used in this work. The phenomenon has been observed in several instances throughout our electrodeposition experiments. For example, in the process of rhodium NW growth inside PC100WT2025 polycarbonate template, hydrogen evolution manifested itself as small surface intrusions on the NWs (see Figure 3.1). Hydrogen bubbles trapped between the growing NW and membrane wall are most likely to be the reason for formation of these tiny surface intrusions.

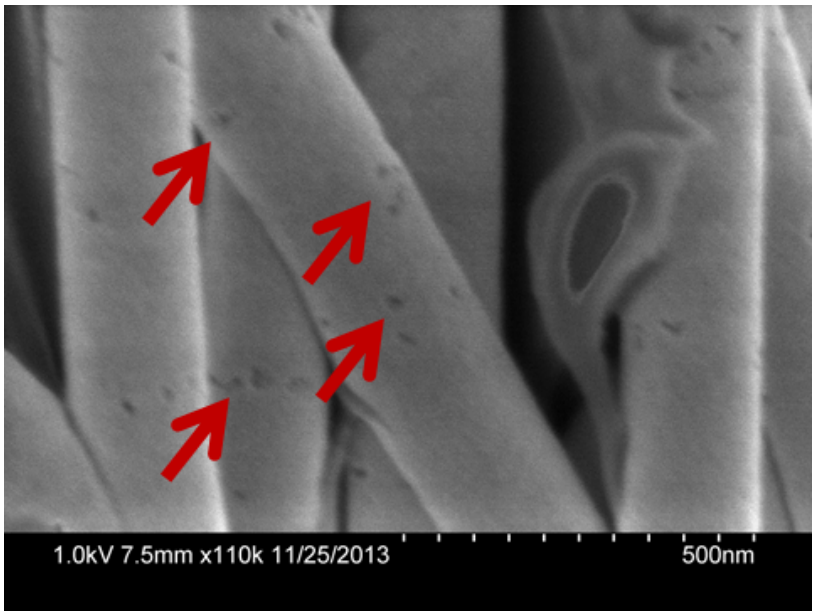

Figure 3.1: Small intrusion found on the side surface of some rhodium NWs most probably due to hydrogen bubbles being trapped between the growing NW and the PC100WT2025 polycarbonate surface.

The co-reduction of hydrogen in the NW electrodeposition process, reduces the current efficiency by consuming a fraction of charge available for ion reduction. Several other phenomena observed in the NW growth from aqueous solutions in this research, were found to be related to the hydrogen evolution process. Hydrogen evolution during gold NW deposition was found to be responsible for the formation of gold pellets [9] (discussed in Chapter 4). Moreover, we have shown [10] that hydrogen evolution can be used for tailoring the grain structure of rhodium NWs, as discussed in Chapter 5.

3.1.6 Effect of Additives on Nucleation and Growth

Additives can alter nucleation and growth mechanisms through various routes. For instance, additives can become adsorbates (adsorbed substances) at the surface of the cathode [39].

There are two basic types of adsorption: chemisorption and physisorption. In chemisorption, the chemical attractive forces of adsorption act between the surface and the adsorbate (usually there are covalent bonds). Thus, there is a chemical combination between the substrate and the adsorbate where electrons are shared

and/or transferred. New electronic configuration may be formed through this sharing of electrons. In physisorption, the physical forces of adsorption, Van der Waals or electrostatic forces, act between the surface and the adsorbate; there is no electron transfer and electron sharing [39].

Considering the transfer of hydrated metal ion to the lattice sites, adsorbed additives affect the concentration of growth sites on the growing surface. They can also change the concentration of adions on the surface or alter their diffusion coefficient and the activation energy of the surface diffusion of adions [1]. Additives can also influence the propagation of microsteps and cause bunching [39].

When intended to enhance the brightness of the elecctrodeposit surface, the additives are sometimes called *brighteners*. The brightness of a surface is defined as the optical reflecting power of the surface. Three possible mechanisms for bright deposition by brighteners have been suggested [39]: (1) diffusion controlled leveling, (2) grain refining and (3) randomization of crystal growth. Some fundamental aspects of brightening and leveling are reviewed by Oniciu and Muresan [40].

An additive may also be consumed at the cathode by incorporation into the deposit and/or by the electrochemical reaction at the cathode or anode [39]. Additives can significantly influence processes such as hydrogen evolution during NW growth, as will be shown in Chapter 5. Additives can also disable the formation of unwanted nanoparticles and encourage one dimensional growth of NWs as will be discussed in Chapter 4.

3.2 Structure and Mechanical Properties of Electrodeposits

Nucleation and growth processes are important in nanoresonator fabrication because they determine the structure and hence, the mechanical properties of the NW resonator. The two most relevant mechanical properties of electrodeposited NWs for resonator application are the modulus of elasticity and the intrinsic dissipation. These determine the frequency values of the resonance peaks and the quality factor of the resonator, which affects the signal to noise ratio, as well as the accuracy of experimental resolution of the peak frequency. Other mechanical properties include the yield, tensile and fatigue strengths, and the ductility.

The moduli of elasticity of electrodeposits reported in the literature generally show

significant deviations from those of same material formed by other methods. One main reason for this is the difficulty of obtaining accurate values [39] for different geometries of the electrodeposited material with minimal measurement error.

Mechanical properties are related to the structure of the electrodeposit. For instance, the primary sources of tensile strength are impediments to the movement of dislocations. In electrodeposits impediments are grain boundaries. Therefore, refining the grains by controlling the electrodepositon parameters or use of additives is a way to alter the density of grain boundaries and hence, the strength. The structure of the substrate —being the silver contact layer for NW synthesis— can also alter the structure of the electrodeposit. Several factors can influence this dependence. If the inter-atomic distance in a particular crystal plane of the substrate closely matches that of the deposit, the structure of the former may be continued into the latter. Such condition is called *epitaxy*. Even in the absence of epitaxy, the morphology of the substrate can affect the structure of the deposit.

Electrodeposition conditions such as high overvoltages or high current densities or certain additives can favor the formation of three-dimensional nuclei, that is, the start of new grains. In this case, the relationship between the substrate and the electrodeposit tends to be lost [39].

On the other hand, elevated temperatures of the electrodeposition solution and low current densities, which permit migration of atoms to sites where they can be incorporated into an existing structure, favor epitaxial growth. Elevated temperatures lead to a decrease of the cathode polarization, to a more efficient transport of ions towards electrodes, and to an increase of the surface diffusion [41].

The shape and the size of the grains is determined by the electrodeposition conditions and the composition of the solution. Simple, pure electrodeposition solutions such as acidified copper sulfate produce large, columnar grains that generally exhibit a fiber axis. Solutions based on complex compounds such as copper cyanide or solutions containing active addition agents tend to yield fine-grained deposits that usually do not exhibit a texture [39].

Almost all metal deposits are made of grains whose structural-physical nature can be divided into five types[4]: (1) columnar, (2) equiaxed, (3) dendritic, (4) nodular and (5) fibrous [1].

1. *Columnar*: these types of grains are most common in compact thin films. They

[4]There are other grain-structural classifications such as: (1) columnar, (2) fine-grained, (3) fibrous, and (4) banded [1].

are the result of preferred growth in certain crystal directions, Randomly oriented grains are usually small in comparison to the film thickness.

2. *Equiaxed*: these grains may, and do, grow to relatively larger sizes than columnar grains.

3. *Dendiritic*: in electrodeposited films, dendritic-type grains result from mass-transport-controlled growth, and the individual crystals may vary in shape.

4. *Nodular*: because of their appearance, nodular structures are often referred to as "cauliflower type". Although the phenomenon has been attributed to a number of factors (such as impurities), the origin and the growth mechanism of this feature are still not well understood.

5. *Fibrous*: this type of grain is the result of oriented growth of grains that cover the substrate only incompletely.

In electrodeposition there is a competition between the rates of new crystalline formation and existing crystal growth [1]. For instance, for the creation of single crystals the first process should dominate [41]. Specifically, the effect of deposition conditions during the process is such that the deposition close to limiting current (maximum current that can be reached before the process becomes limited by mass-transport) leads to dendritic growth, as the effect of transport is more pronounced in systems exhibiting low activation overpotential. Well below the limiting current, an increase in the activation overpotential tends to favor formation of equiaxed smaller-grained deposits because nucleation is facilitated [1].

It is worth remembering that a large number of variables in the electrodeposition process have bearing on the structure. These include metal-ion concentration, additives, current density, temperature, agitation, and polarization. These variables need to be studied for every solution-substrate system.

3.3 Characterization of the Deposit Structure

Various characterization techniques can be used for revealing the structure of electrodeposition. Light microscopes[5] have very limited resolution for structural analysis. A light microscope provides color information, but it has a limited depth of focus.

[5] We avoid using the phrase optical microscope because all the microscopes are optical [42].

The resolution of light microscopes is limited by the wavelength of light being up to five orders of magnitude larger than electron wavelength. In this work we have used a light microscope as a part of a probe-station machine (Signatone 1160) for quick checks on NWs shape and sizes. This microscope was also used for controlled NW positioning and bottom-up assembly of resonator devices, but not for systematic structural analysis of NWs.

The most frequently used instruments to reveal the structure of electrodeposits are electron microscopes. Electron microscopes are available mainly in a scanning electron version (SEM) and a transmission electron version (TEM). The SEM is used particularly for observing the fine structure of a specimen surface at high magnification, whereas the TEM is used mainly for observing the inner structure of a specimen at very high magnification.

In the following sections, SEM, TEM and their uses will be briefly described. Also, a chemical composition spectroscopy technique (EDX), used commonly in this work, will be mentioned. In this study, we have occasionally collected X-ray diffraction (XRD) patterns with resolution of 0.05° (2θ) and a scan speed of 1°/min using a Cr source diffractometer (Rigaku Miniflex) with Kα radiation, λ=2.890 nm operating at 30 KV and 15 mA.

3.3.1 Scanning Electron Microscopy (SEM)

The main disadvantage of the SEM is that it is not possible to produce electron diffraction patterns. Thus, the crystal structure and orientation of the grains cannot be determined. Great care has to be taken when the SEM is used to determine the grain size [39]. When secondary electrons are used for imaging, nodules consisting of many crystallites can have the appearance of grains and be easily mistaken for them.

For historical reasons, fairly high accelerating voltages i.e., 15-20 kV used to be a common setting for SEM operation. Now, thanks to improvements in electron optics, the routine mode of SEM operation is the low-voltage mode [43].

The low-voltage mode of operation is crucial in observation of non-conductive and/or beam sensitive specimens such as template materials. Because the emission of secondary electrons increases as the accelerating voltage decreases, there is a chance to find a beam energy where no charging occurs. That is when the number of electrons (secondary and backscattered) leaving the specimens equal to the number of incident electrons entering the specimen. Additionally for beam sensitive specimens, lower

electron beam energies reduce the the chance of beam damage.

One of the most obvious consequences of decreased accelerating voltages is reduced interaction volume. The secondary electron signal produced from a smaller sized volume, which is closer to the surface, contains more surface information. e.g., contamination. Many kinds of surface contamination can become fully- or semi-transparent at higher voltages. Not only contamination but also any small surface details could be smothered or completely wiped out by higher accelerating voltages.

In this work, a Field Emission Scanning Electron Microscopy (FESEM, Hitachi S-4800) was used to obtain information about size, shape, defects, morphology and grain structure of deposited silver, gold and rhodium. FESEM uses a tungsten electron gun whose cathode operates at room temperature and provides a very high brightness source.

3.3.2 Transmission Electron Microscopy (TEM)

The TEM has better resolution than the SEM and the capability to obtain electron diffraction patterns. It is possible to obtain atomic resolution with the TEM. The main disadvantage of the TEM is that only very thin specimens can be examined. Therefore, extensive preparation is required for characterization of the electrodeposits with TEM.

With the TEM it is possible to unambiguously determine the grain size. The determination of grain size is possible by placing the field-limiting aperture around an area believed to be a grain. An electron diffraction pattern is then obtained from the area defined by the aperture. If the pattern is that of a single crystal, the area is a grain [39]. The orientation of the grain can be determined from the diffraction pattern. Additionally, several features of interest in electrodeposits such as twins, grain boundaries, dislocations and other defects can be identified under TEM.

In this work, Hitachi HF-3300 TEM was used as an operating mode of Hitachi HF-3300V Scanning Transmission Electron Holography Microscope (STEHM). However, preparing thin-enough specimens for electron diffraction studies from NWs with diameters greater than 200 nm still remains challenging (see Appendix D).

3.3.3 Energy-Dispersive X-ray Spectroscopy (EDX)

SEM machines are usually combined with an X-ray analyzer permitting compositional analysis of a microscopic area. In this work, chemical status of NWs was confirmed

using an Energy Dispersive X-ray Spectroscopy (EDX, Bruker Quantax) operating as a part of the S-4800 FESEM.

3.4 Potentiostatic Electrodeposition and Diagnostic Techniques

Electrodeposition can be operated in two main modes: potentiostatic and galvanostatic. Since the nucleation process is a direct function of overpotential (see Eq. 3.2), fixing the potential can provide a better control over the electrodeposition process. Potentiostatic deposition governs the depositing morphology by providing necessary energy for formation of a single morphology across the whole substrate. In galvanostatic deposition, since no control is exercised over the resulting cathode potential, obtaining uniform morphology throughout the substrate is difficult [44]. In this work, for electrodeposition of silver, gold and rhodium into the porous templates, potentiostatic mode was chosen.

Diagnostic techniques such as linear potential sweep (voltammetry) and current-time transient (chronoamperometry) will be briefly introduced in this section. Before explaining these methods and how they can be useful in electrochemical nucleation and growth studies, it is necessary to describe the main steps involved in a typical electrochemical deposition process. A general Red/Ox electrochemical reaction can be written as:

$$Ox + ze \Longleftrightarrow Red \tag{3.8}$$

This reaction proceeds in at least five steps [1]:

1. Transfer of Ox from bulk solution to the interphase.
2. Adsorption of Ox onto the electrode surface.
3. Charge transfer at the electrode from Red.
4. Desorption of Red from the surface.
5. Transport of Red from the interphase into the bulk of the solution.

Steps (1) and (5) are mass-transport processes. Study of the charge transfer processes (step (3)), free of the effect of mass transport, is possible by use of transient

techniques. In transient techniques, the interface at equilibrium is changed from an equilibrium state to a steady state characterized by a new potential difference. The analysis of the time dependence of this transients is a basis of transient electrochemical techniques. The next section, briefly introduces potentiostatic transient (chronoamperometry) and potential sweep (linear voltammetry) methods as two examples.

3.4.1 Chronoamperometry

In the potentiostatic transient technique, the potential of the test electrode is controlled while the current, the dependent variable, is measured as a function of time. The potential difference between the test electrode and the RE is controlled by a potentiostat [1]. The input function (a constant potential) and the response function $i = f(t)$ are shown in Figure 3.2.

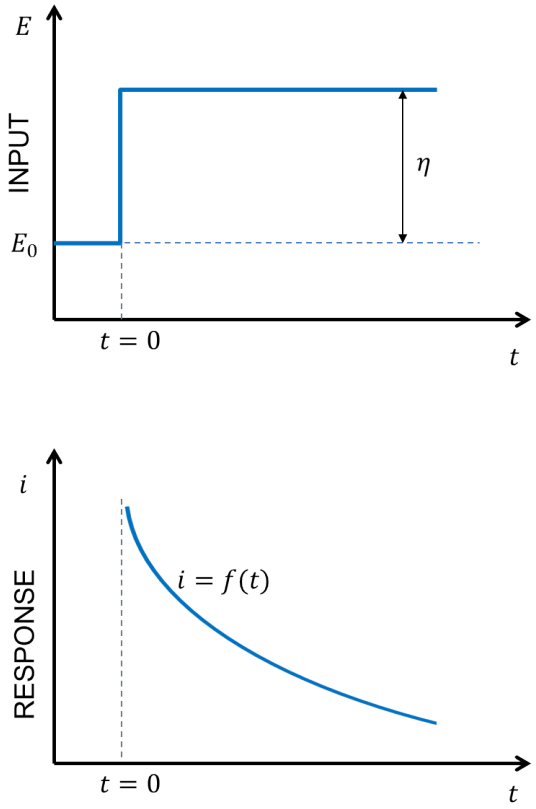

Figure 3.2: Variation of current (response) with time during potentiostatic step (input) reproduced from [1].

In the simplest case, the Cottrell equation describes the change in electric current

with respect to time in a controlled potential experiment, such as chronoamperometry. Specifically, the Cottrell equation describes the current response when the potential is a step function:

$$i = \frac{zFA_pD^{1/2}c}{\pi^{1/2}t^{1/2}} \tag{3.9}$$

where i is current, D and c are the diffusion coefficient and the bulk concentration of the target ion, respectively. A_p is the electroactive surface area of the planar electrode (Eq. 3.9 is specifically derived for planar electrodes). However, Cottrell equation does not directly show the effect of overpotential on the current.

For studying electrochemical kinetics, Butler-Volmer equation is one of the most fundamental relationships. It describes how the electrical current on an electrode depends on the electrode potential:

$$i = i_0(\exp\frac{(1-\alpha)zF\eta}{RT} - \exp\frac{-\alpha zF\eta}{RT}) \tag{3.10}$$

where i_0 is the exchange current and α is the transfer coefficient that changes between 0 and 1. For large positive values of overpotential, Eq. 3.10 reduces to Tafel equation:

$$i \approx i_0 \exp\frac{(1-\alpha)zF\eta}{RT} \tag{3.11}$$

and for large negative values of overpotential, Eq. 3.10 reduces to:

$$i \approx -i_0 \exp\frac{-\alpha zF\eta}{RT} \tag{3.12}$$

Butler-Volmer equation is valid when the electrode reaction is controlled by electrical charge transfer at the electrode (and not by the mass transfer to or from the electrode surface from or to the bulk electrolyte). Nevertheless, the utility of the Butler-Volmer equation in electrochemistry is wide. When the electrode process is mass-transfer controlled, the value of the current is limited by diffusion. The limiting current i_L is given by:

$$i_L = \frac{zFDc}{\delta} \tag{3.13}$$

where δ is thickness of the diffusion layer and c is the bulk concentration of the target ion.

Chronoamperometry is a technique for studying the kinetics of electrochemical

reactions. One way chronoamperogramms are useful is to determine if the electrodeposition is mass-transport controlled (mentioned in section 3.6.2). Another way chronoamperogram can be useful is in determining how long it will take to fill the pores of a membrane. As an example, Figure 3.3 shows a case were silver was electrodeposited into a polycarbonate template for a long time such that all the pores were filled and a silver film grew on top of the template (right side of the image). By comparing the SEM image in Figure 3.3 to a corresponding chronoamperogram in Figure 3.4 obtained during the electrodepositon process, the pore filling time can be found.

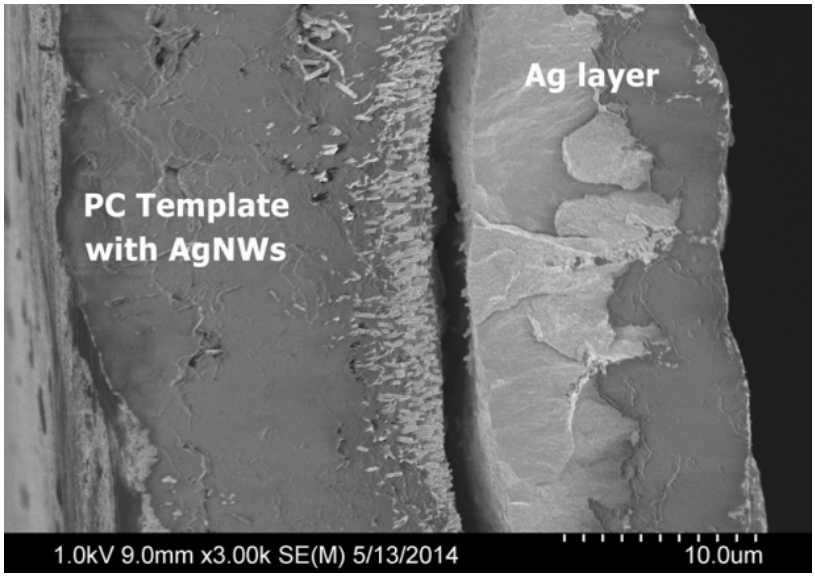

Figure 3.3: Cross-sectional SEM image of a polycarbonate template filled with NWs and formation of an Ag layer on top of the template. Silver was electrodeposited into a polycarbonate template with 200 nm pore size at -500 mV vs RE for a prolonged time to find the optimal electrodeposition time.

Figure 3.4 shows four distinct regions. Initially (region I) there is a sharp current peak immediately after the inception of the experiment followed by rapid decrease in the current. This region corresponds to the double layer capacitor charging [45] and a diffusion drop. In the region II, the template pores are being filled with silver and the current is linearly increasing. This linear decrease (small-slope) in current at region II happens as a result of a linear increase in the electroactive surface area, which is specifically related to pore structure of PC100WT2525 templates.

In the region III, a transition region (between 1000 to 1600 s) is observed corre-

sponding to a transition from NW to film growth. After ∼1000 s, the template pores were filled with silver. The electrodeposit that has reached to the top surface of the template is now free to grow in three dimensions until coalesces with other growing electrodeposit parts. At this point (∼1600 s), a silver layer will cover the template surface and will be uniformly growing. The steady current in the region IV (after ∼1600 s) corresponds to the silver layer growth. An steady current is also predicated under potentiostatic conditions from Bulter-Volmer equation (Eq. 3.10).

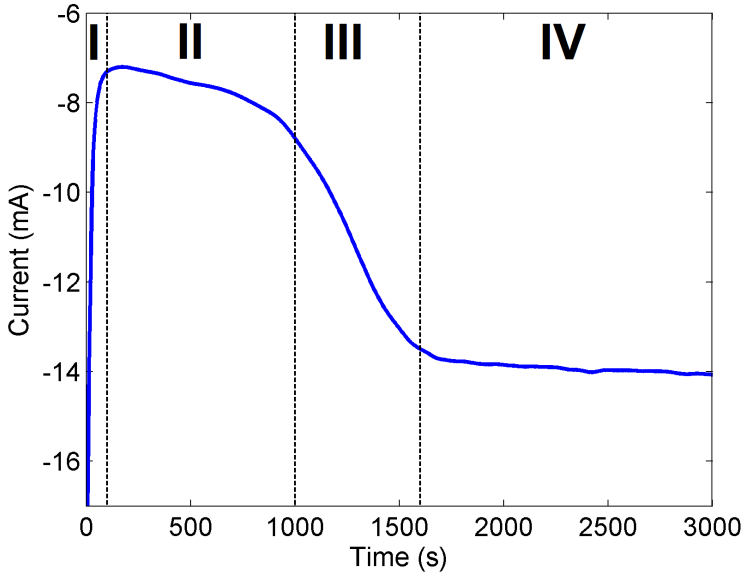

Figure 3.4: Chronoamperogram obtained during the electrodeposition of silver into a polycarbonate PC100WT2525 template at -500 mV vs RE shows four distinct regions. The transition region III corresponds to transition from NW to film growth. After ∼1000 s all the pores were filled with silver. The increase in the electroactive surface area is most probably the main reason for the change in the curve slope. After ∼1600 s (region IV) indicating uniform growth of the silver layer, the current becomes steady.

As briefly mentioned in section 2.6.3, chronoamperometric curves can be helpful for determining the optimized time of silver electrodeposition for closing the pores and preventing NW solution leakage. Figure 2.12 shown in section 2.6.3 plots the potentiostatic current vs elapsed time curves for several pore-closing experiments. The current in all the curves begins to flatten after about 3 minutes and can be considered as almost steady after 4 minutes of silver electrodeposition. A steady current suggests that a stable electrodeposition condition was reached with no considerable change in

the electroactive area. This seems to be about the time that electrodeposition of silver is no longer continuing outside the pores as no unsteady current variation was observed.

The ratio of the current in region II to the current in region IV ($\frac{i_{II}}{i_{IV}}$) estimates the relative surface area available for electrodeposition inside the membrane (porosity). This ratio is approximately equal to $\frac{7.6}{13.7}$ or 55% from Figure 3.4.

Chronoamperometry can be used for other purposes such as determining electrochemical nucleation mechanisms based on known models. For instance, Scharifker and Hills [38] have developed models for instantaneous and progressive electrochemical nucleation in 2D and 3D. They use chronoamperometric curves as a diagnostic technique for determining the nature of nucleation and growth. In this work, the chronoamperometric curves obtained are far from what is expected from these models. The main reason probably is that the template confinement significantly alters the geometry of the diffusion zones.

3.4.2 Linear Voltammetry

In the potential sweep technique, the $i = f(E)$ curves are recorded directly in a single experiment. This is achieved by sweeping the the potential with time. In linear sweep voltammetry, the potential of the test electrode is varied linearly with time (as shown schematically in Figure 3.5).

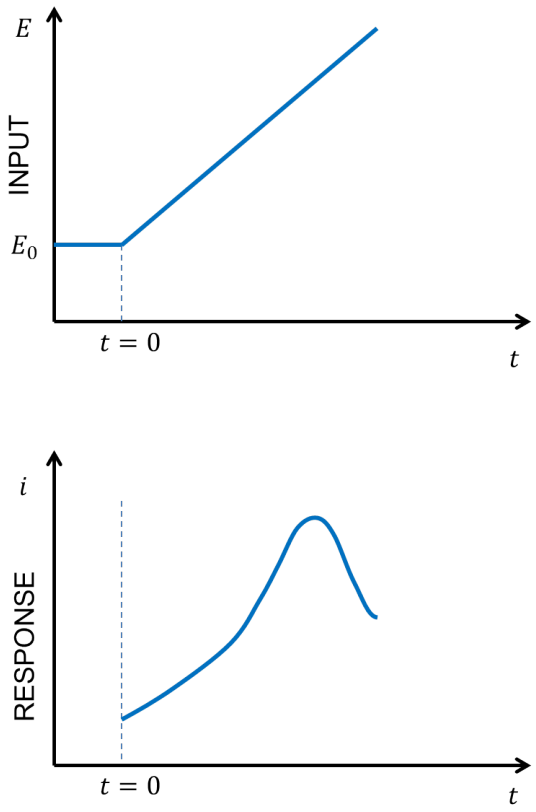

Figure 3.5: Linear potential sweep voltammetry showing the input and response function. Schematic image reproduced from [1].

If the sweep rate is ν mV/s, then the potential E_t of the test electrode at time t, in the cathodic polarization is given by:

$$E_t = E_{t=0} + \nu t \tag{3.14}$$

where $E_{t=0}$ is the initial potential. The sweep rate is usually in the range of 1 to about 1000 mV/s (depending on application). A typical current response curve is shown in Figure 3.5. Butler-Volmer equation (Eq. 3.10) predicts linear current-potential relationship at low overpotentials and exponential curvatures at higher overpotentials. However, the charge transfer or mass-transport limits cause deviations from Butler-Volmer equation and result in formation of current peaks. That is why voltammetry is a powerful diagnostic technique for electrochemical studies.

A common way of choosing the operating potential is to look at the linear potential sweep curves (voltammograms). Figures 3.6, 3.7 and 3.8 show the voltammograms

obtained for typical silver, gold and rhodium solutions used in this work. The NW electrodepositon potential was chosen by consulting these Figures. There can be several other uses for these voltammograms especially if obtained systematically for various solution concentrations and scanning rates. In this work, the voltammograms were mainly used to find a suitable electrodeposition operating potential.

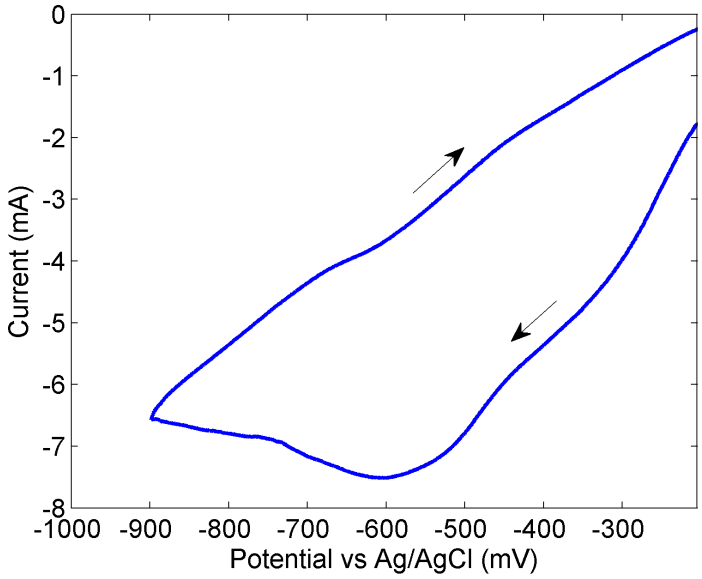

Figure 3.6: Linear sweep voltammogram obtained at 5 mV/s from a silver Cy-less solution (SOL5). The directions of the reverse and forward scans are marked with arrows.

The voltammogram for silver electrodeposition shown in Figure 3.6 marks a clear cathodic peak at E≈-600 mV vs RE. Using higher potentials (more negative) than -600 mV will not increase the deposition rate because the reaction rate is limited by diffusion. Based on this curve, for silver electrodeposition into the template, a potential of -500 mV was chosen. This working potential is large enough to speed up the growth of the silver without making the deposition purely diffusion-controlled.

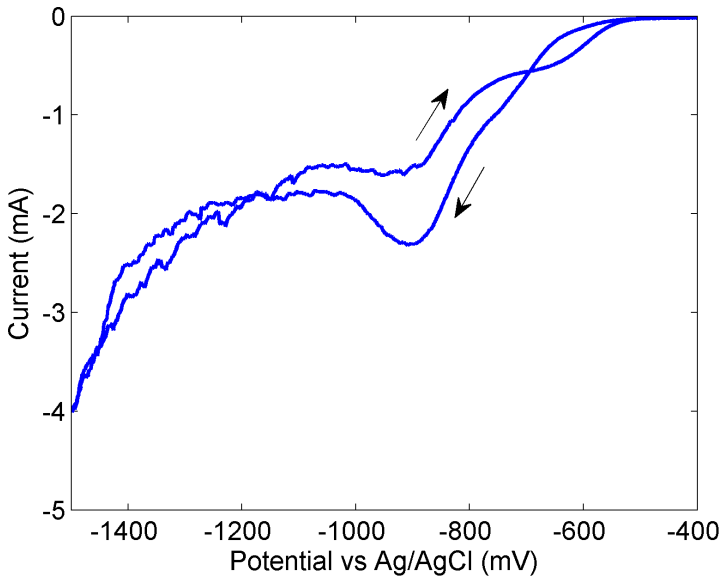

Figure 3.7: Linear sweep voltammogram obtained at 5 mV/s from a gold sulfite solution without additive (SOL1). Current fluctuations observed due to intense hydrogen evolution at potentials more negative than -1000 mV. The directions of the reverse and forward scans are marked with arrows.

In Figures 3.7 and 3.8 the disturbing effect of hydrogen evolution is more dominant at higher cathodic potentials and manifest itself as fluctuations in current. In the case of rhodium, the voltammetry peaks are completely masked due to a very high rate of hydrogen reduction from the acidic solution SOL6 (pH=0.7). Table 3.1 summarizes the working potentials used for all the materials involved in NW growth process.

The lower limit of working potential can be easily found from the voltammograms obtained. For instance in the case of gold (Figure 3.7), potentials more positive than -500 mV cannot be used as the measured current is almost zero (zero reaction rate).

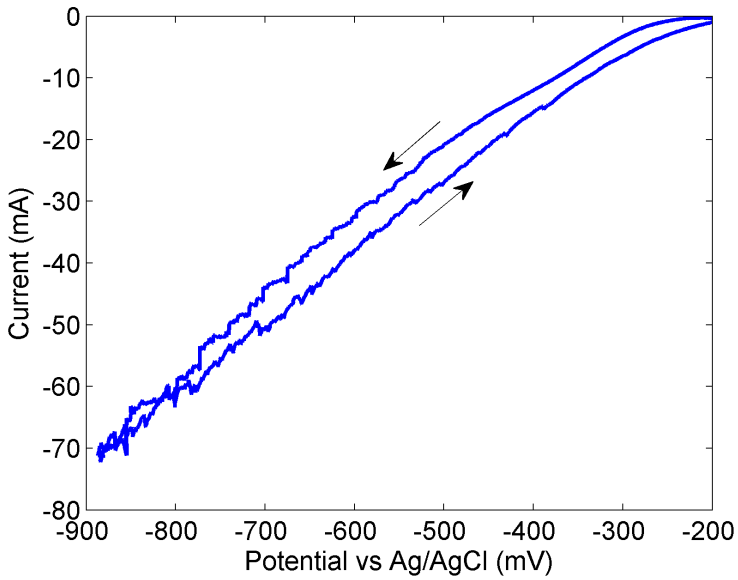

Figure 3.8: Linear sweep voltammogram obtained at 5 mV/s from rhodium sulfate solution (SOL6) with pH=0.7. Current fluctuations observed due to intense hydrogen evolution starting at potentials more negative than -400 mV. The directions of the reverse and forward scans are marked with arrows.

Table 3.1: The working potentials used for the electrodeposition of silver, gold and rhodium towards NW growth in this work.

Material	E vs RE (mV)
Ag	-500
Au	-700 to -950
Rh	-250 to -400

Linear voltammetry was also used for studying the effect of PEI as an additive in the nucleation and growth of gold NWs, which will be discussed further in Chapter 4.

3.5 Nucleation and Growth of Silver

As discussed in various sections of Chapter 2, silver electrodeposition into the template is an essential step before electrodeposition of NW materials in order to obtain single and separable or clean and pure batch of NWs. Silver electrodeposition in the case of anodized aluminium oxide template, sacrificially fills the branched region of the template. In the case of polycarbonate templates, silver electrodeposition solves the solution leakage problem from the open pores.

The electrodeposited silver in both cases, will be dissolved in nitric acid in the NW extraction process. However, the nucleation and growth of the electrodeposited silver should be studied as it serves as the substrate for NW growth. The silver deposit needs to be compact and uniform to make a suitable substrate for gold or rhodium NW growth in this work. Figure 3.9 shows SEM images of a silver electrodeposit grown to fill the branched region of an anodized aluminium oxide template after template dissolution. The silver electrodeposit has the form of NWs as it was grown to $\sim$8 μm length.

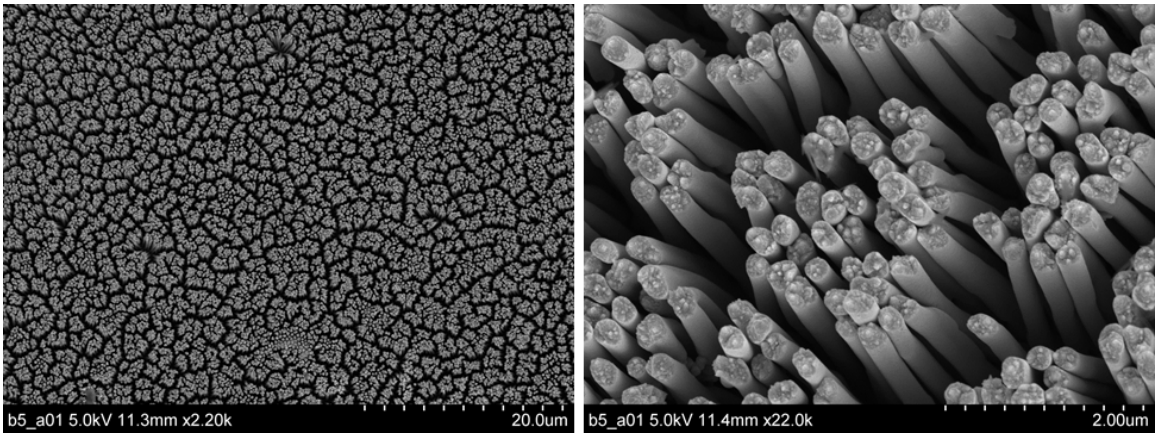

Figure 3.9: SEM images of electrodeposited silver inside anodized aluminium oxide template obtained after template dissolution.

The silver was electrodeposited from SOL5 at -500 mV vs the RE for one hour at room temperature. Figure 3.9 shows that silver grows uniformly under these conditions and provides a compact deposit that can be used as a substrate for NW electrodeposition. Other electrochemical working conditions have been used for electrodepsition of silver as NW clamp, which will be discussed in Chapter 6.

3.5.1 Chemistry of Silver Solution

Silver forms a number of water-soluble species, both simple and complex, any of which in principle might serve as the basis for electrodeposition solutions. The first group of compounds are simple salts (compounds in which silver is the sole cation.) In general, silver salts are stable only up to a pH of about 4. Above that, hydroxides or other species precipitate. Additionally, acid solutions are often corrosive; and since silver is noble with respect to other metals in the electromotive series, it is very prone to immersion deposition. Silver salt solutions are often photosensitive as well [46].

Silver complexes (forms in which silver is in the anion) are generally more stable than the simple salts, and thus less susceptible to photosensitivity and immersion deposition. They are also usable over wider ranges of solution pH. In this work, we have used commercially available Cy-less (from Technic) silver solution, which is based on silver succinimide $Ag(C_4H_5NO_2)_2$. Silver solubility of succinimide is less but close to silver cyanide and higher than thiosulfate and dimethyl-hydantoin [46].

Most reports on the structure of electrodeposited silver in the literature focus on deposits from cyanide. There are very limited number of published articles on the microstructure and grain morphology of the silver electrodeposits from succinimide complex and therefore, we chose to study the structure of the silver deposits, using SEM.

3.5.2 Grain Size and Morphology of Silver

It is usually expected that the electrodeposition of silver from non-cyanide solutions form a finer-grained deposit as compared to cyanide solutions [39]. The structure of the deposit from a given solution at fixed temperature, depends primarily on the current density, as mentioned in section 3.2. The potentiostatic deposition of silver at -500 mV vs Ag/AgCl RE typically gives a current density in the range of 2–4 mA/cm^2 at room temperature.

Figure 3.10 shows the grain morphology of silver surface grown in an anodized aluminium oxide template. The grain structure based on Figure 3.10 was characterized to be nodular. Small nodules ranging mostly from 30 to 50 nm can be observed at the higher magnification SEM image.

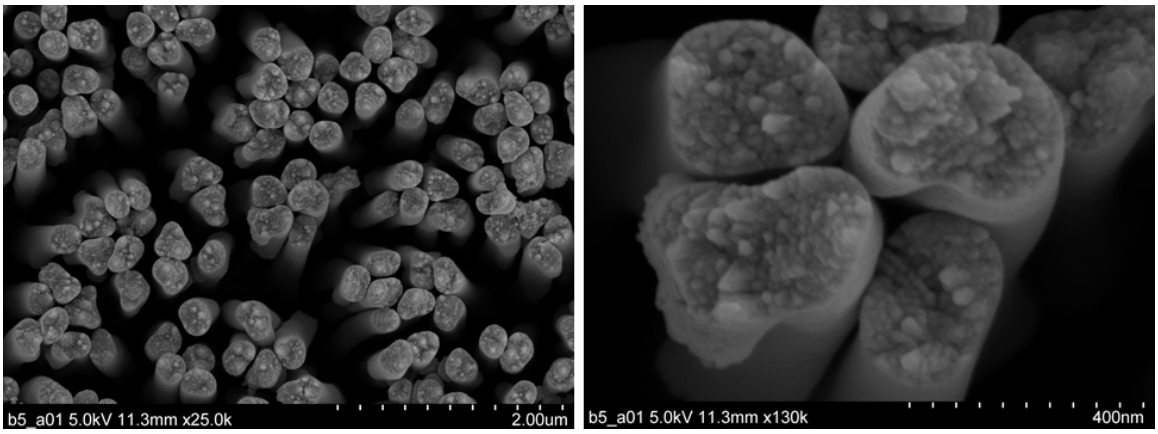

Figure 3.10: SEM images show nodular grain morphology obtained from silver electrodepositon inside an aluminium oxide membrane at -500 mV vs the Ag/AgCl RE.

The small nodule size may be attributed to the current densities close to limiting current (or large overvoltage) based on the cathodic potential used for silver electrodeposition. The voltammogram obtained in Figure 3.6 shows a current peak at -600 mV. The working potential for silver electrdeposition was -500 mV that is relatively close to the max -600 mV for mass-transport limit of the working potential.

In summary, the compact, non-dendritic and uniform electrodeposition of silver from succinimide solution into the templates was found to be suitable for gold and rhodium NW growth.

3.6 Nucleation and Growth of Gold

Electrochemically deposited gold has satisfied many of the demands of the electronics industry. Gold has the third best electrical and thermal conductivity of all metals at room temperature. It also has high ductility and excellent wear resistance, which are important for electrical contacts [39]. However, obtaining a desired structure of gold electrodeposit for electrical or mechanical use, especially from non-cyanide solutions is not easy.

The nucleation and growth of gold electrodeposit needs to be understood and controlled for obtaining a suitable electrodeposit that can be used for making NW resonators. While a detailed discussion about the nucleation and growth of gold NWs from a non-cyanide solution is presented in Chapter 4, the next two sections describe our learning from several initial attempts to electrodeposit gold NWs from

non-cyanide solutions and their results.

3.6.1 Chemistry of Gold Solution

Numerous proprietary gold electrodeposition baths and additives are used industrially, most of which contain cyanide. Traditionally, gold has been electrodeposited from gold cyanide electrolytes due to the exceptional stability of the gold cyanide complex [47]. The stability of the Au(I) cyanide complex is reflected in the shift of reduction potential for Au(I) in aqua complex from 1.71 V to -0.61 V in cyanide complex [39]. However, due to concerns about safety and disposal of process waste, there is a growing concern regarding the use of cyanide based processes [9, 47–51]. In this work, we have used a gold sulfite solution (SOL2) for electrodeposition of gold NWs. Gold sulfite is a plausible, well-studied alternative to gold potassium cyanide and poses considerably lower risk from toxicity [9, 51–53].

The chemical composition of the main gold electrodepotion solution used in this work is given in Table 2.2.2. This solution was used with organic additive polyethylenimine for NW growth, which has been discussed extensively in our paper [9] presented in Chapter 4. Also for comparison in a few experiments, a simple gold chloride salt in water (SOL5) was also tried for making gold NWs.

In order to show the effect of the chemistry of gold solution on the NW growth process, the analysis of SEM images was mainly used. SEM images revealed the main challenge in the gold electrodeposition from SOL1: formation of pore-blocking pellets.

Figure 3.11 shows an SEM image taken from the cross-section of an anodized aluminium oxide template used for gold electrodeposition. The SEM image has been false-colored for chemical analysis using an EDX X-ray detector. In all the three images of Figure 3.11, the silver contact layer is on the bottom and the pore entrance side of the template is seen on the top. Red in the EDX color-mapped image corresponds to silver. Based on this image, silver is only present on the bottom where it is expected to be. But, the green color representing gold, shows the presence of gold nanoparticels in most of places across the template but more intensely in the regions close to the silver contact layer and the pore entrance (top) of the template.

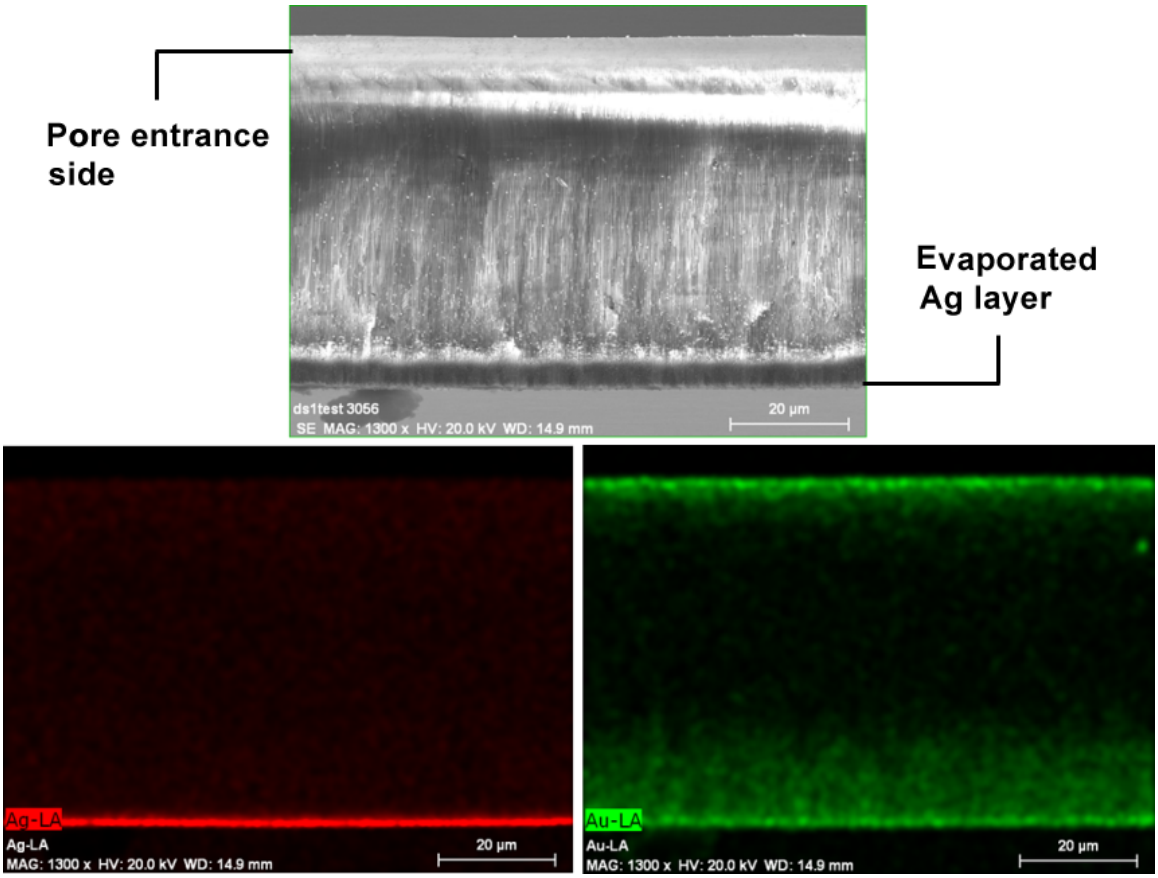

Figure 3.11: An SEM and two EDX color-mapped images taken from the cross-section of an aluminium oxide template. The silver layer shown in red is present at the bottom of the template. Gold electrodeposits, shown in green, are dispersed mostly in the regions close to the bottom and top of the template.

Figure 3.12 shows a closer look at the interface of silver contact layer and the pores, where the gold NW growth was expected to start from. It was observed that gold nanoparticles are formed in place of NWs. The gold nanoparticles are aggregated and formed small tubular structures in the regions close to the silver contact layer, as shown in Figure 3.12.

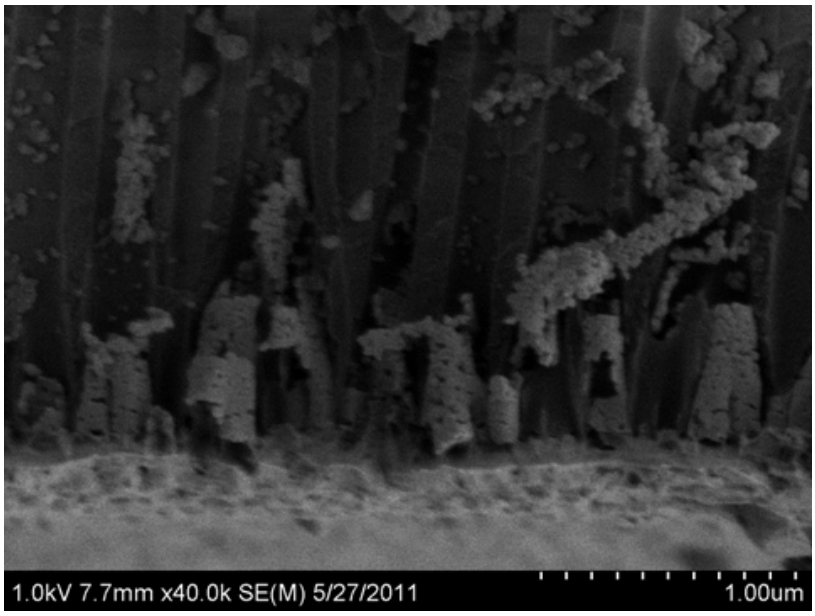

Figure 3.12: The aggregation of spherical gold nanoparticles forming small tubular structures at the pore-silver interface.

This pattern of gold nucleation and growth was observed in all the attempts made with the PEI-free non-cyanide solution (SOL1). Using this solution and changing several parameters (one at a time) such as the working potential and the temperature did not remove the nanoparticles (pellets). Figure 3.13 shows two SEM images obtained after electrodeposition of gold under two different conditions. Figure 3.13A shows the gold electrodeposit (room temperature) taken after silver and template removal. Only gold pellets were observed and no NW or nanorod particles.

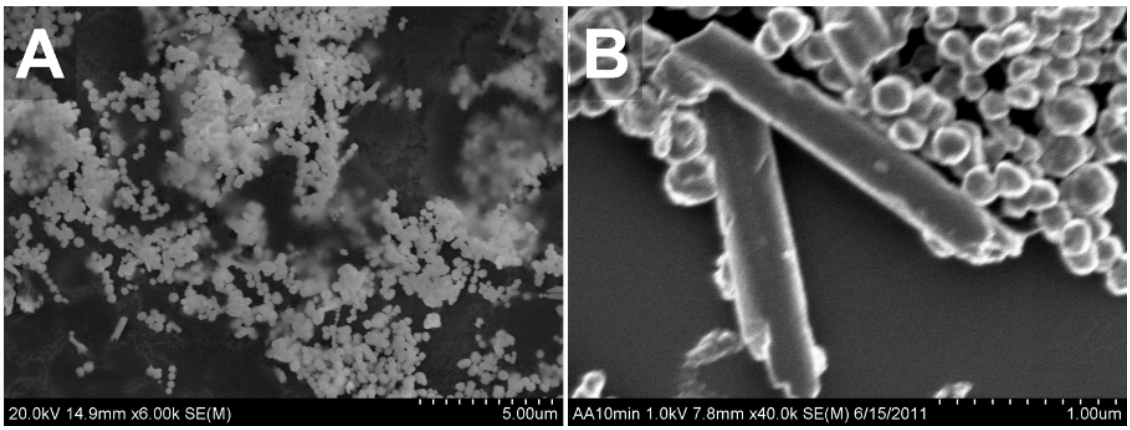

Figure 3.13: Formation of gold (A) pellets and (B) rods and pellets under two different electrochemical conditions using SOL1.

Figure 3.13B shows pellets as well as rods 1-2 μm long obtained by electrodeposition form the same solution at 40°C. The rods shown in Figure 3.13B are the longest rods that could be electrodeposited by the same solution under all the reasonable electrochemical working conditions that were tried. The reason that rods could not grow longer than $\sim$2 μm is the formation of growth-arresting gold pellets discussed thoroughly in Chapter 4. This problem was solved by addition of polyethylenimine in very small quantities to the solution.

Also, as mentioned earlier, in an effort to make gold NWs from a cyanide-free solution, a simple gold chloride solution (SOL5) was also used. Figure 3.14 shows the structure of gold elecrodeposit obtained at -700 mV vs the open circuit potential. The wire-like electrodeposit was found to be porous and non-compact. In general, most electrodeposits made using solutions containing no additives (simple salts such as the one used here) are noncompact. These types of deposits are of no practical value in most applications [39].

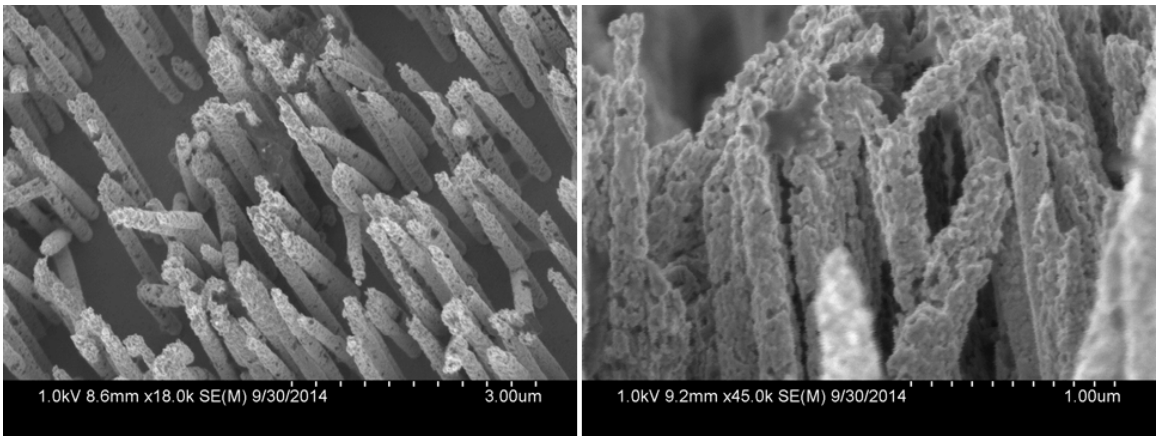

Figure 3.14: Non-compact, wire-like structure of gold electrodeposited from the gold chloride SOL5 at -700 mV vs the open circuit potential at room temperature.

Another example highlighting the importance of the solution chemistry in the nucleation and growth of gold is when the ratio of bath component slightly changes. In one experiment, the gold content of the sulfite solution (SOL1) was doubled while keeping the content of the other components the same. Figure 3.15A shows a tilted cross-sectional view of a template after silver electrodeposition followed by gold electrodeposition from the solution with the unbalanced gold content. In Figure 3.15A, silver NWs are seen on the top, empty template pores in the middle, and the dendritic gold deposit on the bottom of the image. Figure 3.15B shows a closer look at the gold dendrites formed on the surface of the template (bottom of the Figure 3.15A). This shows the key role of complexing agents whose concentration must be adjusted to grow NWs.

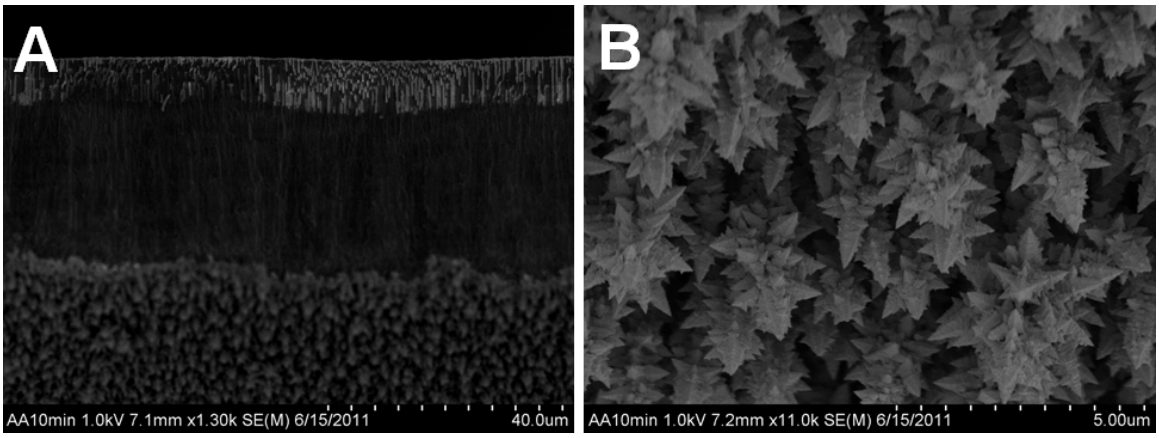

Figure 3.15: Formation of gold dendrites on the surface of template during the electrodepositon of gold from a gold solution with unbalanced gold content (a fraction of gold ions expected to be uncomplexed). (A) From top to bottom: silver NWs in branched region, empty pore of template, and gold dendrites. (B) Gold dendrites formed on top of the template surface.

Dendrite nucleation and growth is a result of a different gold solution chemistry. The gold ions in the solution that are not complexed by sulfite groups, may even electrolessly deposit on the template surface. A more detailed description about the electroless growth of gold can be found in the paper [9] in Chapter 4.

3.6.2 Grain Size and Morphology of Gold

The Young's modulus of a resonator affects its resonance frequency and Q-factor (see section 7.5 and Eq. 7.1). The Young's modulus of a NW is influenced by its grain structure and can be significantly different from the Young's modulus of bulk polycrystalline material. For instance, Li and coworkers [4] have measured an elastic modulus of 44±12 GPa for resonator gold NWs made from a cyanide solution. This value is 54% of 82 GPa quoted for bulk polycrystalline gold [4, 54]. In another study [5], Young's modulus of gold NWs measured by AFM deflection was reported to be 70±11 GPa. Other values have also been reported by other groups [4].

The grain size and structure, texture, and the synthesis method of the NWs are considered to be the main factors determining the Young's modulus of metal NWs, and hence, their Q-factor [3, 4]. The grain size of gold NWs made in this work was measured by use of SEM. Figure 3.16 shows four images (A:D, low:high magnification) revealing the grain size and morphology of the gold NWs made from a sulfite-based

solution by use of PEI as an additive (SOL2) [9]. The Figure 3.16D shows a number of grain size measurements. The average grain size for these gold NWs is ∼12 nm.

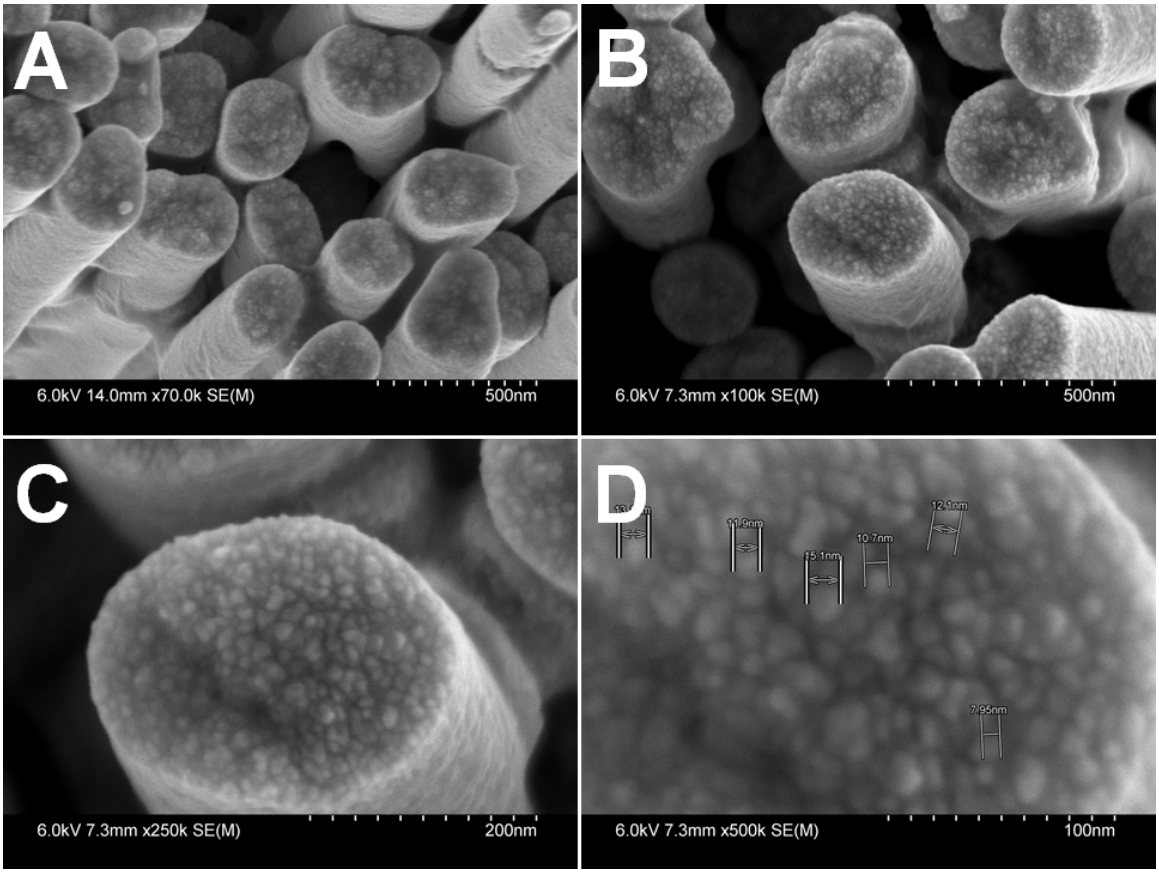

Figure 3.16: SEM images showing the grain size and morphology of gold NWs grown from a sulfite-based solution (SOL2), at various magnifications (from (A) to (D) magnification increases). The grain size measurements determine an average size of ∼12 nm.

The small grain size can be attributed to the high overpotential used in the electrochemical synthesis. A higher working potential can be useful to accelerate NW growth up to the diffusion-limited current. Typical current density transients for gold electrodeposition are shown in Figure 3.17, in a negative potential region from -0.925 to -1 V with respect to the RE. In each transient, a sharp current density peak recorded instantly after potential application (peak inception not apparent in the Figure) occurs due to the double layer charging. The peak is followed by a sharp fall because the concentration is depleted within the pores [45].

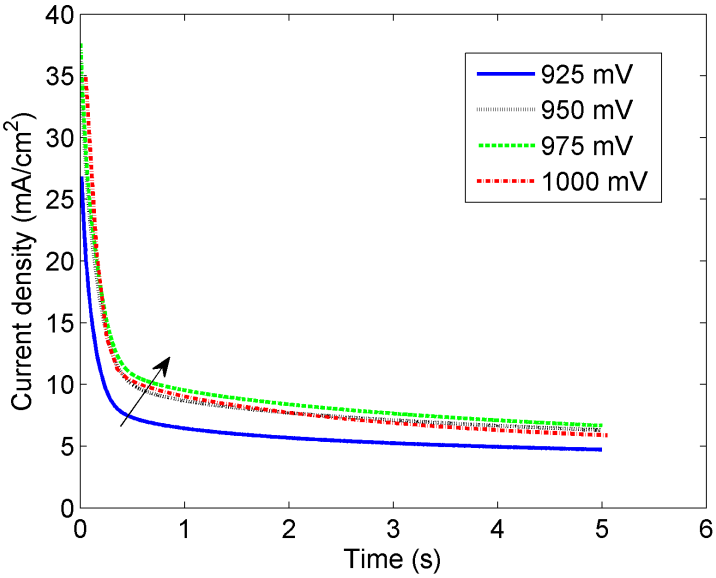

Figure 3.17: Current transients for gold reduction from a sulfite-based solution indicating diffusion-controlled electrodeposition at negative potentials higher than -0.95 V from a solution with PEI vol.% of 0.1.

Figure 3.17 reveals that by increasing potential up to -1 V, chronoampermetric curves show little further change and practically overlap, indicating that NW growth is mass-transport restricted (diffusion-controlled) at potentials over ∼0.95 V. Similar curves obtained from solutions with PEI concentrations of 0.001 to 0.1 vol.%, showed the same behavior. It can be concluded that the diffusion-limited current did not change significantly by varying PEI concentrations below the proper range of the additive (less than 0.1 vol.%).

In separate preliminary study for synthesizing gold particles and wires by use of an electrospinning device, micron-size spherical particles of gold were deposited on a substrate by use of ethanol as an reducing agent. A brief discussion of this work is presented in Appendix E (see Figures E.1 to E.3).

3.7 Nucleation and Growth of Rhodium

Nucleation and growth of rhodium from a commercial sulfate-based solution with various additives such as PEI, EDTA, sulfuric acid, and a commercial stress reducer (containing sulfamic acid) has been explored in this work. A more detailed discussion is given in the paper [10] presented in Chapter 5.

The main motive for using various chemistries was to be able to alter the nucleation and growth mechanism of rhodium NWs to obtain nanoresonators with higher elastic modulus and hence, a higher resonance frequency and Q-factor.

3.8 Early-stage Tube-to-rod Growth

Examination of several templated electrodeposition specimens at the initial stage of growth were imaged by SEM in order to check for void-free growth. Several SEM and TEM images of a gold specimens, electrodeposited for a long enough time to reach 1 μm height and over, revealed that nanostructure formation does not entirely follow a tubular growth sequence and has no visible voids. Several similar analysis confirmed that for lengths of NW over $\sim$1 μm, the nanostucture grows effectively in a layer-by-layer fashion. However, our investigation illustrates that in the very first steps of gold solid formation, a tubular structure forms, which rapidly merges into a rod structure. Figure 3.18 shows the formation of gold nanotubes in the early stage of the electrodeposition (when the length of nanorods is less than $\sim$0.5 μm).

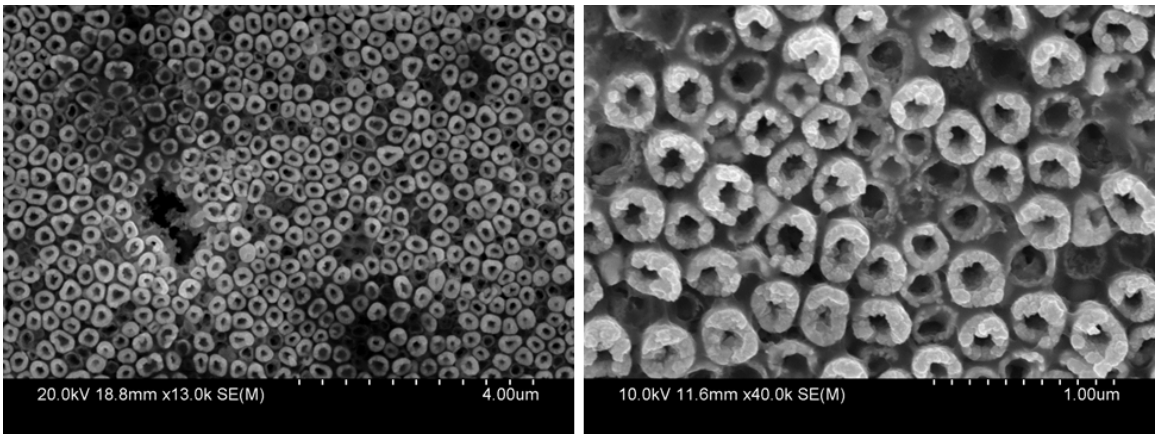

Figure 3.18: Early-stage ($<$1 μm tall) gold electrodeposit inside aluminium oxide template is tubular.

Figure 3.19 shows the tube-to-rod conversion of gold electrodeposit occurs when the length of the electodeposit is between $\sim$0.5-1 μm. This growth pattern at the early stages of NW growth has been observed repeatedly for both gold and rhodium NWs (see Figure 3.20 for rhodium). The reason for this type growth in electrodeposition process has not been reported in any studies so far. Although there are many studies published on the nucleation and growth of one dimensional nanostructures, e.g., [35,

36, 55], they mostly cover nucleation and growth of single crystalline particles not polycrystals. Also, most studies in these areas concern CVD and surfactants-assisted wet chemical methods for making nano-crystalline particles.

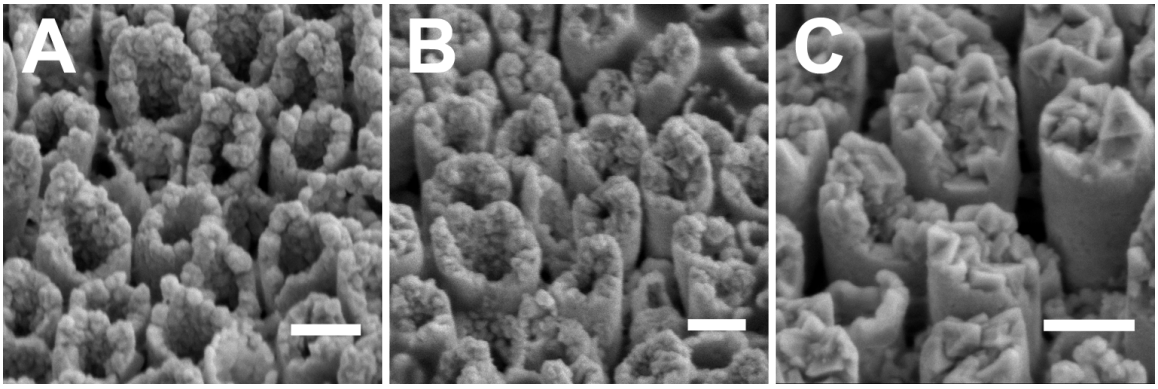

Figure 3.19: Structural conversion of gold nanotubes to nanorods shown from (A) to (C). Gold nanotubes turn into NWs rapidly by about 0.5-1 μm length. Scale bars mark 250 nm.

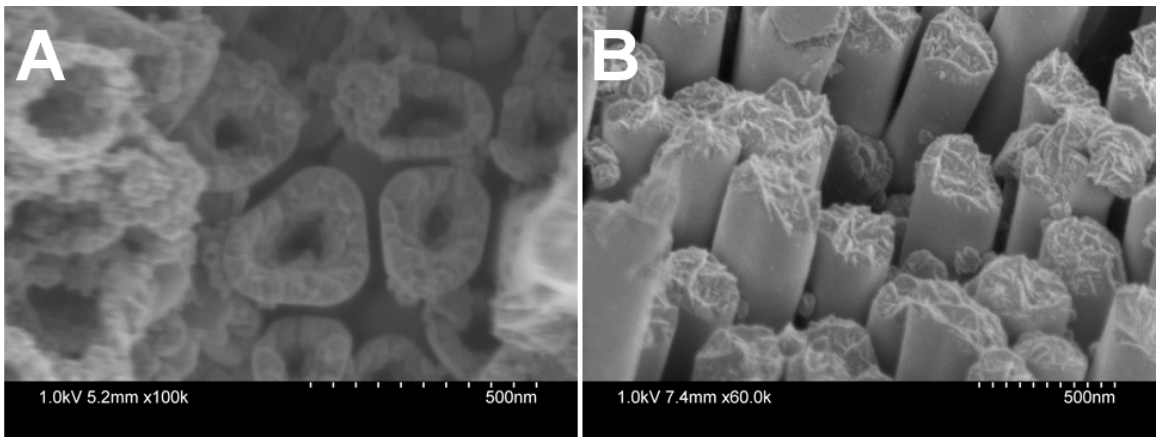

Figure 3.20: Structural conversion of rhodium (A) nanotubes to (B) nanorods. Rhodium nanotubes turn into NWs rapidly by about 0.5-1 μm length.

In this particular example of polycrystalline nanotube formation, the inception of the growth from the pore-substrate interface may be attributed to the higher surface energy available for heterogeneous nucleation. The critical nucleation radius nucleation r (see section 3.1) and thus, the nucleation energy ΔG would be smaller for the nuclei forming at the corners (pore-substrate interface). Therefore, the probability of nucleation of a ring on the silver substrate is higher than other locations on the

silver. Nonetheless, after the gold tube formation, the electrodeposition continues by polycrystalline nucleation and growth of gold on gold, which is of a different nature compared to nucleation of gold on silver.

The fact that the same pattern of polycrystalline NW growth has been also observed in the case of Rh electrodeposition, suggests that a more general mechanism might be found by more investigation. Moreover, since the NW growth effectively continues in a layer-by-layer fashion even before reaching 1 μm size, long enough NWs (>10 μm) can be considered as deposits without voids. Our TEM studies have also confirmed void-free deposition of long NWs.

3.9 Nanowire Growth Time and Charge

In an engineering laboratory it is important to be able to roughly estimate the time required for growing a batch of NWs to a certain length. However, there are many parameters affecting the time scale of NW growth. For instance, NW length does not linearly change with growth time as the solutions is depleted from the metal ions (concentration reduces over time). Even at a given working potential and electrode distances, there are other factors influencing the NW growth time. These mainly include the chemistry of the solution and additives, current efficiency, pore structure of the template, and temperature fluctuations.

Current efficiency is an important figure in electrodeposition and connected to many factors including deposition potential and hydrogen evolution. When two or more reactions occur simultaneously at an electrode, the number of coulombs of electricity passed corresponds to the sum of the number of equivalents of each reaction. For example, during the electrodeposition of gold or rhodium from an aqueous solution at least two cathodic reactions occur: the deposition of rhodium and the reduction of hydrogen ions producing hydrogen bubbles. The current efficiency of an electrochemical reaction is defined as the number of coulombs required for that reaction divided by the total number of coulombs passed. Current efficiency calculation have been done for rhodium electrodeposition from sulfate-based solutions with two different pH values (see Chapter 5).

In order to provide a general guideline for estimating the NW deposition time, coulombometric curves were used together with the SEM results to generate electrodeposition guide curves for two most frequently-used templates. In these plots, length vs charge were drawn instead of time because many parameters can change

the deposition time. Using the total passed charge is especially useful for combining the effect of several parameters such as the working potential, current efficiency and time into one. The structural characteristics of the template such as branching, pore connections, pore density, etc., can also change the filling time. Therefore, for each template a different curve might be expected.

Figure 3.21[6], for example, can be used for estimating the electrodeposition time required for making gold NWs inside aluminium oxide templates. The potentiostat software provides a charge counter for the electrodeposition processes.

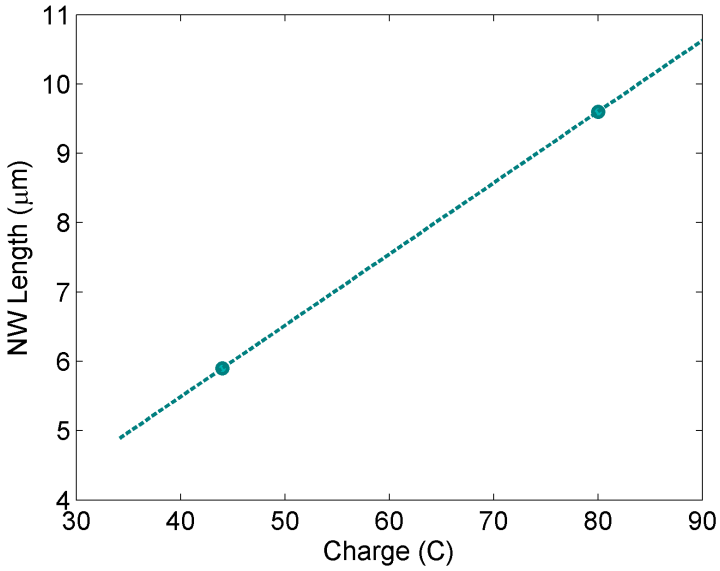

Figure 3.21: Guide curve produced for estimating gold NW deposition time inside anodized aluminium oxide templates. The curve was produced by combining SEM results with coulombometric data obtained from the electrodeposition software.

Figure 3.22 shows that the total charge required for making longer NWs does not increase linearly when working with aluminium oxide template and a regular rhodium solution at -400 mV vs RE. A single data point obtained at a lower working potential of -250 mV follows a linear trend with the first two data points at -400 mV. The reason for this might be related to the higher current efficiency at lower working potentials [10] (see Chapter 5).

[6]Only two data-points were available for this plot.

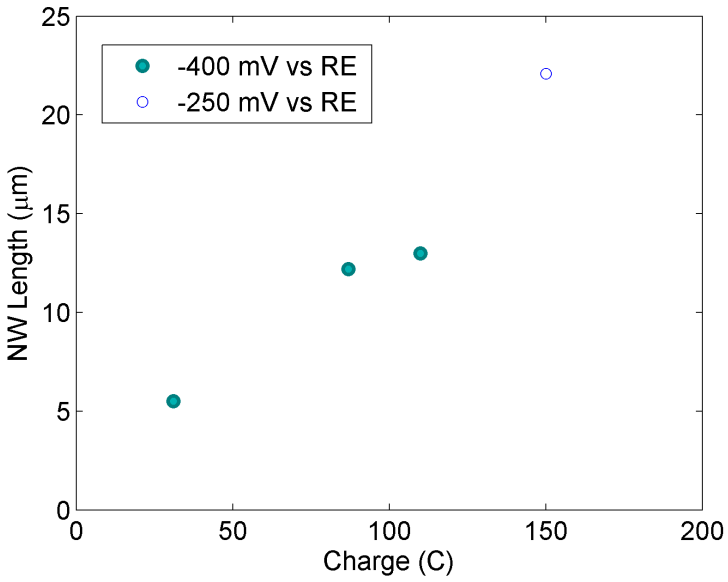

Figure 3.22: Guide plot produced for estimating rhodium NW deposition time inside anodized aluminium oxide templates. The curve was produced by combining SEM results with coulometric data obtained from the electrodeposition software.

Figure 3.23 shows the effect of rhodium stress reducer as an additive in the total charge required for NW growth to a certain length. For a given amount of charge, the length of rhodium NWs obtained from a regular rhodium solution is longer than those obtained from a solution with commercial stress reducer.

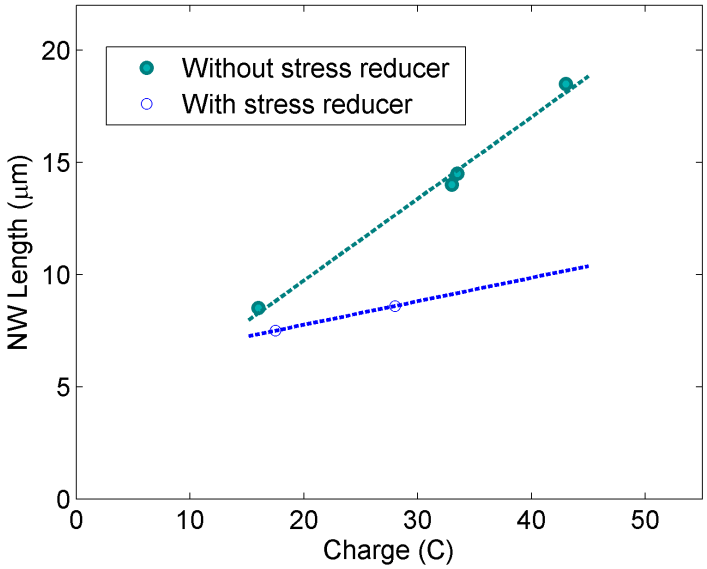

Figure 3.23: Guide curves produced for estimating rhodium NW deposition time inside PC400ST2525 templates from an additive-free solution and a solution with commercial stress reducer. The curves were produced by combining SEM results with coulombometric data obtained from the electrodeposition software.

Additionally, comparing the green curve in Figure 3.23 with the curve in Figure 3.22 shows that the charge-length relation remains almost linear when working with polycarbonate PC400ST2525 template even after reaching ∼19 μm length, whereas, for the anodized aluminium oxide the curve becomes non-linear after ∼13 μm.

3.10 Conclusions

The electrochemical nucleation and growth of gold and rhodium NWs strongly depends on overvoltage applied in the electrodeposition. The grain size and structure of the obtained electrodeposit (important for mechanical properties) is also a function of overvoltage. Electrochemical nucleation and growth from aqueous solution is influenced by the presence of hydrogen and hydronium ions and therefore reduction of hydrogen at the cathode. The additives can change the chemistry of electrodeposition process and therefore, alter the nucleation and growth process. The structure of the electrodeposit in this work has been mainly studied by use of SEM at low acceleration voltages. The grain size of gold NWs was measured to be ∼12 nm at

high potentials, which bring the electrodeposition current close to the mass-transport limiting current. Chronoamperometry and linear voltammetry were introduced and used for several purposes. Effect of complexing agents and various chemistries of the solution for gold NW deposition were investigated by use of SEM characterization. A tube-to-rod growth pattern was observed for early stages of NW electrodeposition. It was shown that metal nanotubes are formed initially and merge into nanorods before reaching 1 μm length. Guide curves were produced to for NW growth time estimation based on the total charge passed from the cell.

3.11 Future Work

A more in depth study of nucleation and growth of early-stage rhodium and gold nanotubes may suggest a path to synthesize longer nanotubes that can be used as resonators. For a given length, the Q-factor of nanotubes is higher than NWs.

NWs made inside aluminium oxide templates can undergo annealing or other heat-treatment processes to alter their grain structure and hence their mechanical and physical properties.

TEM measurements for determining the grain structure of thick NWs is challenging. Additionally, using FIB for TEM sample preparation has several disadvantages such as melting or recrystallizing the structure. A gentle specimen preparation method should be developed for studying the grain structure and the texture of deposited NWs with TEM.

Chapter 4

Gold Nanowire Synthesis from Sulfite Solution

This chapter presents an article published [9] under the title of *Suppressing electroless growth allows cyanide-free electrodeposition of straight separable gold nanowires*. The article (Electrochimica Acta 114 (2013), 643-648) is reproduced with permission from Elsevier.

Abstract

Gold cyanide is strongly complexed in solution and works well for the electrochemical synthesis of separable nanowires. Straight single axisymmetric nanowires are significant for many applications, but particularly so for sensors based on nanoelectromechanical systems (NEMS) such as nanoresonators. The toxicity of cyanide solutions makes non-cyanide alternatives desirable. However, electrochemical synthesis of gold nanowires in templates from non-cyanide solutions suffers from serious drawbacks. These include growth-arresting pellet formation, poor length control and defects such as inclusions. Here we present the first electrochemical synthesis of straight, cylindrical, separable gold nanowires from a sulfite solution. We demonstrate a scheme that suppresses electroless particle growth in the weakly-complexed gold in solution. We discuss a mechanism for this scheme, which suggests that this approach has potential for better controlled electrodeposition in separable nanowire synthesis.

4.1 Introduction

Template-synthesized metallic nanowires (NWs) are of interest to diverse communities of nanoscience research and nanosensor development. Our interest in this paper is in the synthesis of long, straight, separable, cylindrical, non-porous NWs with good length control. These attributes are important for many mechanical applications of NWs, such as resonant NW sensors [56]. For this reason and for brevity, in this paper we will use the term *mechanics-grade* to describe such NWs. Mechanics-grade NWs are important for sensing applications including sensitive multiplexed biosensors [8, 57, 58], gas damping force sensors for transition regime studies in rarefied gases [3, 59, 60] and devices to evaluate mechanical behavior of nanostructured materials -elastic modulus [4, 61], dissipation and plasticity studies [62]. Applications using NW propulsion [63] or electrorotation [64], as well as directed-assembly techniques [3, 65, 66] enabling large-area, low-cost fabrication of device chips, have created new opportunities for the use of mechanics-grade NWs.

Among metal NWs, our interest in gold stems from its chemical stability and the well-known strength of its bond with the thiol group [18] which enables a range of surface functionalization chemistries [8]. As a versatile and inexpensive tool, electrodeposition provides the most suitable synthesis path for mechanics-grade NWs.

Starting from the significant body of pioneering work by Martin [27], Natan [67] and others [68, 69] we found that all mechanics-grade AuNW synthesis reports use cyanide-complexed gold solution, due to its stability and minimal defects of the NWs produced. However, potassium gold cyanide, the most commonly used electroanalyte for gold electrodeposition, is highly toxic [48–51]. Although the strength of the cyanide complexes gives the electroplating bath a long life, its resistance to decomposition, disproportionation and substitution reactions [70] leads to environmental concerns.

Gold sulfite is a plausible, well-studied alternative to gold potassium cyanide and poses considerably lower risk from toxicity [47, 51–53]. The use of solutions of gold sulfite or hydrogen tetrachloroaurate ($HAuCl_4$) has been the subject of several reports on "AuNW synthesis" by electrodeposition [71, 72] or electroless means [73, 74], but a thorough search did not reveal any studies that were able to produce mechanics-grade NWs. Examples in Figure 4.1A-D show that NWs from non-cyanide solutions are tangled (A, B, C), porous (C) or branched (B, C, D). While applications such as catalysis could be well served by such nanostructures, they clearly will not serve the

mechanics-grade NW applications discussed here.

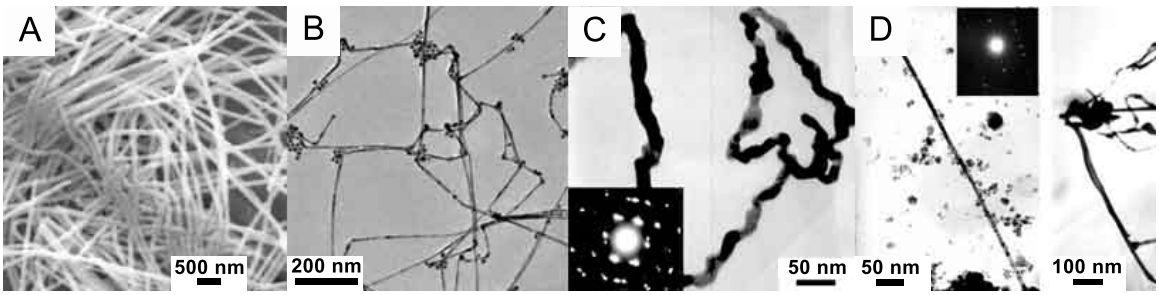

Figure 4.1: Gold NWs synthesis reported by (A) using soduim disulfitoaurate solution [75], (B) reduction of $HAuCl_4 \cdot 4\,H_2O$ with different alkylamines [71], (C) reduction of $HAuCl_4 \cdot 4\,H_2O$ using ethanol [74] and (D) reducing gold from $HAuCl_4$ solution inside monolithic mesoporous silica [73].

Huang *et al.* [76] have shown that during electrochemical deposition of gold from aqueous sulfite solution in alumina template, gold nanoparticles are formed electrolessly as a result of hydrogen evolution. Gold nanoparticle (*pellet*) formation prevents growth of high aspect-ratio NWs.

Here we present a scheme that inhibits gold electroless particle growth leading to the first successful electrochemical synthesis of mechanics-grade AuNWs from a gold sulfite solution. We provide experimental evidence from earlier unsuccessful attempts, including some of our own, which indicate that electroless gold nucleation and growth from the weakly complexed gold solution accounts for various defects and failed attempts. In this work, we demonstrate how mechanics-grade AuNWs free of voids and inclusions can be repeatably electrodeposited with good length control.

4.2 Experimental

4.2.1 Template Preparation

Gold was electrodeposited into nanoporous anodized alumina membranes (Anodiscs from Whatman), with a thickness of 60 μm and with nominal pore diameter of 200 nm. A silver layer, 500 nm thick, was deposited on one side of Anodiscs using an electron beam evaporator (Angstrom Engineering) to serve as the working electrode. To prevent interconnections of deposited AuNWs in the Anodisc branched region, prior to gold, silver was electrodeposited into the branched region at -0.5 V cathodic potential with respect to reference electrode (RE) for 1 hour from commercially available

Silver Cy-Less solution (Technic).

4.2.2 Electrodeposition

Electrodeposition was performed at room temperature in a custom-made Teflon cell with a standard three-electrode configuration using platinum gauze as counter electrode and NaCl-saturated Ag/AgCl as RE. The Anodiscs were rinsed three times with DI water and dried before gold deposition. AuNWs were electrodeposited into pores by applying voltages ranging from -0.9 to -1 volt with respect to the RE from the following aqueous solution [77] with pH=7.0: 5 g/L $HAuCl_4 \cdot 3\,H_2O$ as primary gold source, 2 g/L EDTA for complex stabilizing, 65 g/L Na_2SO_3 to form gold sulfite complex, 12.5 g/L K_2HPO_4 as buffering agent and auxiliary electrolyte. Controlled amounts of polyethylenimine (PEI solution from Sigma Aldrich) were added to the solution to study the growth mechanism and passivation effect. All electrochemical experiments were controlled by a potentiostat/galvanostat VersaSTAT 3 (Princeton Applied Research).

4.2.3 Template Dissolution

The evaporated and electroplated silver was dissolved using nitric acid and the alumina template was dissolved in 3M sodium hydroxide solution and rinsed with distilled water. The remaining AuNWs were extracted by removing supernatant through pipetting after several centrifugation steps.

4.2.4 Characterization of NWs

After AuNW electrodeposition, the Anodiscs were snapped apart without use of any cutting tools, taking advantage of their brittleness. The cleaved Anodisc cross-sections were observed using Field Emission Scanning Electron Microscopy (FESEM, Hitachi S-4800) and color mapped with Energy Dispersive X-ray Spectroscopy (EDX, Bruker Quantax) for elemental composition analysis.

To confirm the purity of NWs, X-ray diffraction (XRD) patterns were collected for one of the specimens with resolution of 0.05° (2θ) and a scan speed of 1°/min

using a Cr source diffractometer (Rigaku Miniflex) with Kα radiation, λ=2.890 nm operating at 30 KV and 15 mA.

Transmission Electron Microscopy (Hitachi H-7000) was also performed at 100 KV acceleration voltage to check for void-free growth of NWs.

4.3 Results and Discussions

We begin by noting the function of each component in the solution, as used in previous reports [70, 77–80] of electrodeposition from gold sulfite. The gold in the solution is contained in the form of a gold sulfite complex. EDTA serves to stabilize the gold complex in sodium gold sulfite [80]. In order to prepare the aqueous gold solution, $HAuCl_4$ is used as the source of initial Au^{III}. Some of the Au^{III} immediately forms Au^{I} upon dissolution in water [78]. A sulfite complex is formed by the addition of sodium sulfite [70]. Some ${SO_3}^{2-}$ groups are consumed to form colorless $[Au(SO_3)_2]^{3-}$ complexes [78]. The change from original yellow to colorless was clearly observed during addition of Na_2SO_3. K_2HPO_4 mainly acts as auxiliary electrolyte and buffering agent [79], to maintain the pH close to 7. The discharge of the gold sulfite complex consists of the following two steps [52]:

$$[Au(SO_3)_2]^{3-} \longrightarrow AuSO_3{}^- + {SO_3}^{2-}. \tag{4.1}$$

$$AuSO_3{}^- + e^- \longrightarrow Au + {SO_3}^{2-}. \tag{4.2}$$

where the charge transfer of Equation 4.2 is the rate-determining step [52].

4.3.1 Observations Using Gold Sulfite Solution Without PEI

In our attempts at AuNW synthesis, the intent was for reduction of gold ions to be initiated at the top of the electroplated Ag and continue filling the pores in a layer-by-layer fashion along the pore axis. We made several attempts at growing AuNWs using the sulfite solution without PEI. We used various gold reduction potentials in a range from -0.7 to -1 V with respect to the RE. Our observations show that some gold reduction from the additive-free solution does occur at the bottom of nanopores, but random gold nucleation occurs all through the pores, resulting in the formation of gold pellets as seen in Figure 4.2A. This has also been observed in the work of Huang *et. al* [76] with a slightly different gold sulfite solution. That study showed

that electrochemically evolved hydrogen nanobubbles are responsible for electroless reduction of gold pellets. When attempting to grow gold NWs, pellet formation eventually causes pore obstruction and halts further growth of NWs.

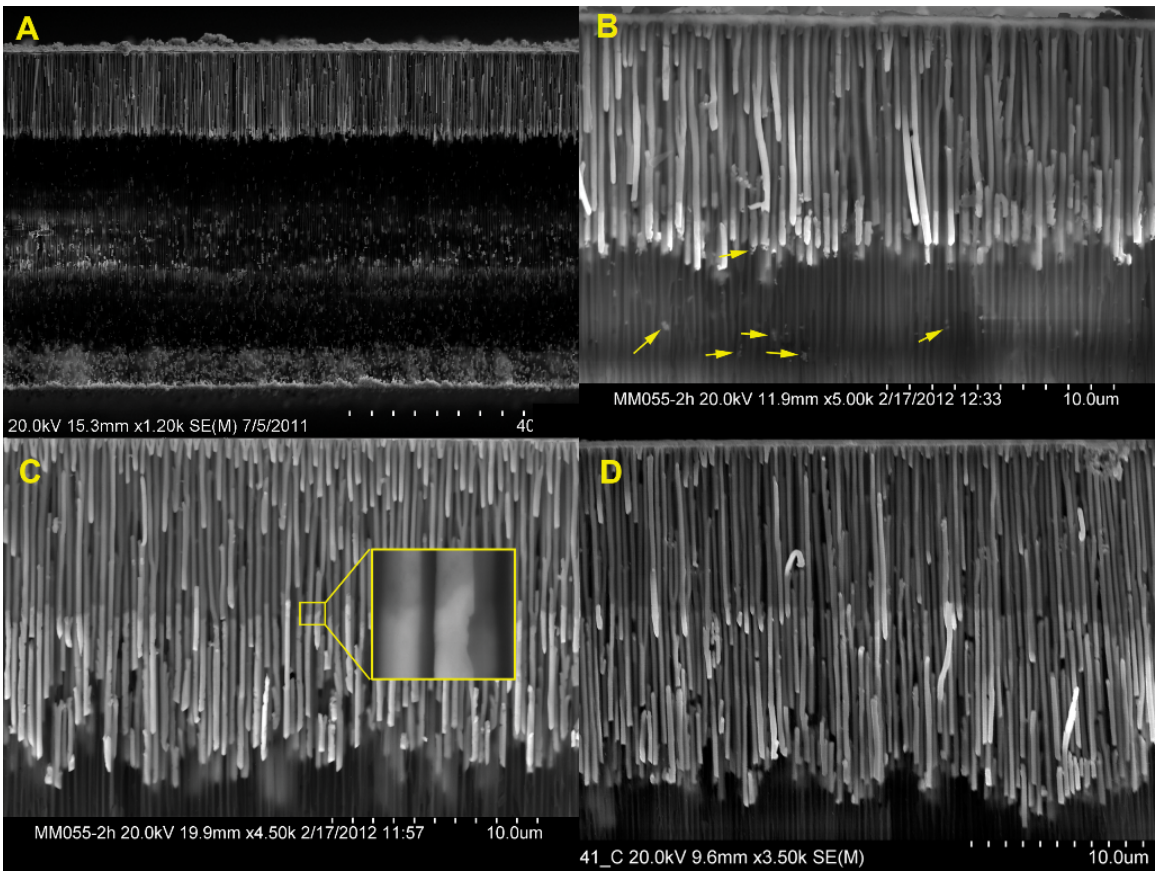

Figure 4.2: (A) Random electroless gold nucleation through the template channels and Anodisc surface obstacle occurs in additive-free solution. (B) Poor quality AuNWs electrodeposited on top of AgNWs from the solution with 0.001vol.% PEI; arrows mark small pellet formation. (C) Pellets avoided by using 0.01 vol.% PEI; AuNWs still show defects even at $\sim$7 μm length. (D) PEI at 0.1 vol.% allows the growth of long ($\sim$12 μm) mechanics-grade AuNWs with better quality and uniformity in length than in C, again with unfilled part of channels showing the absence of pellets. See text for comments on Figures B to D.

It is important to note that such electroless deposition of gold does not occur with gold potassium cyanide, which is more strongly complexed than gold sulfite. This has been a significant motive for the widespread use of cyanide-based solution in gold NW synthesis. We attempted to inhibit gold electroless reduction when working

with sulfite complexes of gold. In order to avoid gold deposition on undesired sites and suppress the growth mechanism, we investigated the effect of PEI addition.

4.3.2 Observations of the Effect of PEI on Gold Deposition

PEI is a water-soluble polymer with repeating unit composed of the amine group and a two-carbon aliphatic CH_2CH_2 spacer. It is a common [81] *brightener*, an additive used for yielding a brighter surface in the electrodeposition of thin films due to its physisorption and strong film-adhesion promoting properties [68]. It is well-known for its high cationic-charge-density and non-toxicity that makes it suitable for gene-delivery [82, 83]. It has also found application as a surface passivator to increase quantum yield of quantum dots [84].

To investigate the effect of PEI, three solutions with 0.001, 0.01 and 0.1 vol.% PEI content were prepared. Adding a trace of PEI with concentration of 0.001 vol.% results in formation of pellets considerably smaller than those obtained from the additive-free solution. The smaller pellets, marked by arrows are seen in Figure 4.2B. By increasing the additive amount to 0.01%, pellet formation is significantly reduced (Figure 4.2C). However, the grown NWs showed imperfections such as intrusions and cavities, as seen in the inset of Figure 4.2C. Finally, as seen in Figure 4.2D, AuNWs synthesised from 0.1% PEI solution showed minimal defects as pellet formation appears to be completely suppressed by adding a suitable amount of additive. Some apparent anomalies in Figures 4.2B, 4.2C and 4.2D are artifacts of the inspection process. Snapping apart the template produces a non-planar cleaved surface with missing, bent (bright ends) or broken nanowires. Our experiments showed that further increase in the concentration of PEI lowers the deposition rate drastically and makes gold reduction impractical even at higher overvoltages. At still higher concentrations ($\sim$0.2 vol.%), gold reduction stopped completely. These observations of the effect of PEI concentration on the electrodeposition process of AuNWs are summarized in Table 4.1.

Table 4.1: Effect of various concentrations of PEI on AuNW electrodeposition process

PEI range (vol.%)	Result
0 to 0.001	Pellets formation
0.001 to 0.05	NWs with voids and inclusions
0.05 to 0.1	Mechanics-grade NWs
0.1 to 0.2	Impractically slow deposition
>0.2	No deposition

It shows a range of concentration-dependent outcomes for PEI over three decades of additive concentration. Eight sets (discs) of mechanics-grade NWs of different lengths were successfully grown with PEI concentration in the 0.05 to 0.1 vol.% range.

4.3.3 Characterization of Synthesized AuNWs

In order to check for the size and the chemistry of deposited metals, a cleaved Anodisc cross-section after electrodeposition was observed using FESEM and color-mapped with EDX, as illustrated in Figure 4.3. This Figure indicates that there is aluminium and oxygen, but no discernible gold, below the NW growth boundary. It was found that approximately 10 μm of silver was deposited in the pores after one hour of plating. The specimen was electrodeposited potentiostatically at $-0.95V$ with respect to the RE for four hours from a gold solution containing 0.05 vol.% PEI. The average diameter of both AgNW and AuNW was found to be $\sim$250 nm, somewhat larger than the 200 nm nominal pore size reported by the Anodisc manufacturer. This is consistent with other studies [85] since these filtration-intent Anodiscs have pore diameter quoted for the reduced pore openings near one face of the discs.

Our intent was to grow AuNWs to a desired length of at least 10 μm with the goal of creating cantilevered resonators for use in sensing applications [8]. Pellets or pore obstruction were successfully suppressed in NW lengths over 10 μm. Dissolution of evaporated and electroplated silver, followed by template removal, provides separable NWs which can easily be transferred to a designated target chip. Figure 4.4A shows that long, straight NWs constitute a large fraction of the AuNWs dispersed on an SEM aluminum stub. Figure 4.4B shows a free single straight cylindrical AuNW of length 11 μm. Figure 4.4C shows several TEM images of the same batch of AuNWs confirming the absence of any kind of significant void or hollow structure. Such separable uniform AuNWs were not reported in any other studies using non-cyanide

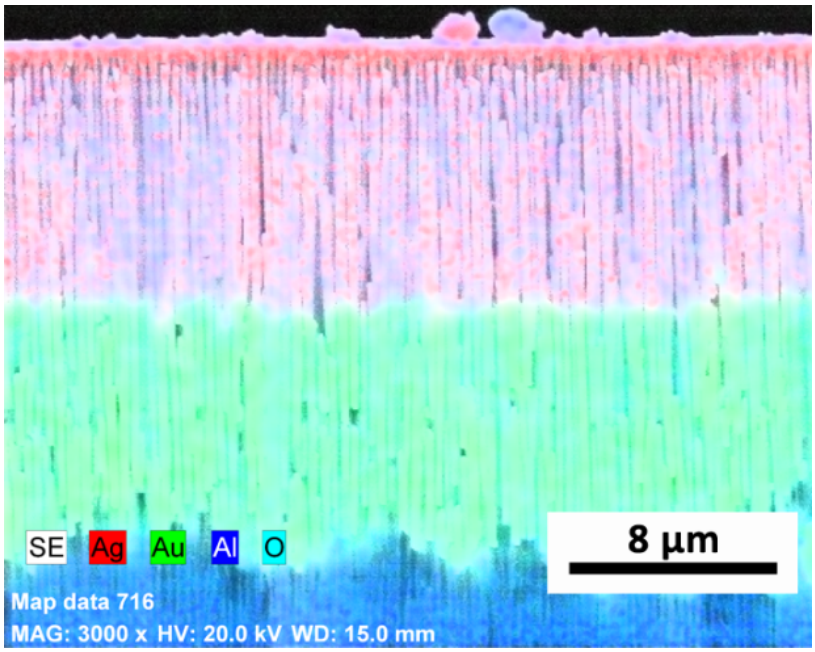

Figure 4.3: Anodisc cross-section: EDX color-mapped FESEM image taken after gold deposition. AuNWs are grown from a solution with 0.05% PEI at -0.95 V.

solutions. These separable NWs can be individually positioned into devices at target locations. As an example, directed assembly by dielectrophoresis has been used for positioning NWs [8, 65, 86] in large arrays.

In order to investigate the purity of AuNWs, powder XRD patterns were obtained from free standing wires with analysed crystallographic information. Figure 4.5 illustrates the distinct diffraction peaks collected at 29.1°, 34.2°, 52.6° and 68.6° corresponding to face-centered-cubic lattice planes of gold (111), (200), (220) and (311) respectively, indicating high purity of the NWs.

4.3.4 The Role of PEI

Repeatable growth of mechanics-grade NWs has been achieved, but only in a small range of PEI concentration, ∼0.05 vol.% to ∼0.1 vol.%. We have described the random nucleation of gold below a threshold of PEI concentration of ∼0.05 vol.% which prevents the growth of mechanics-grade NWs. What role could PEI play in disabling pellet formation (desirable) above 0.05 vol.% and then disabling NW growth beyond the upper threshold of 0.1 vol.%?

Huang *et al.* [76] have shown that electrochemically evolved hydrogen nanobubbles

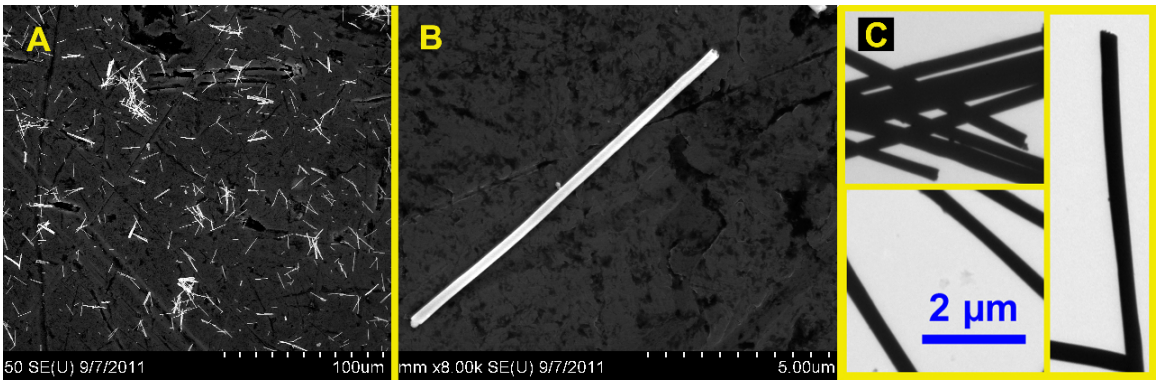

Figure 4.4: (A) FESEM image showing high AuNWs yield after silver dissolution and template removal. (B) Single AuNW made from a solution with 0.05 vol.% PEI at -0.95 V. (C) TEM images of AuNWs confirm the absence of major voids in the synthesized NWs.

in gold sulfite solutions are responsible for formation of hollow nanoparticles of gold which were also observed as pellets in our experiments. The hydrogen bubbles serve both as reducing agent and template to form gold pellets. Additionally, we observe the presence of PEI suppresses electroless gold deposition within the channel walls. The concentration of PEI determines the amount of electroless deposition *i.e.* the size and abundance of pellets. Two main mechanisms for the role of PEI were postulated: *(i)* PEI can increase the pH of the solution, so that there is no significant hydrogen reduction, or *(ii)* PEI could cover electrolessly nucleated gold pellets and prevent their further growth. To examine the mechanism *(i)* we measured the effect of PEI content on solution pH as shown in Figure 4.6. It can be seen that the increase in the gold sulfite solution pH is not strongly pronounced in the operational range of the additive concentration (*i.e.* <0.1 vol.%PEI). The increase in pH from 7.0 to 7.2 favors AuNW electrodeposition by slightly lowering hydrogen evolution rate but still cannot predominantly stop pellet formation and growth. PEI's stabilizing effect on gold nanoparticles has previously been reported [87]. Our experimental results also strongly suggest that the passivation of the electrolessly nucleated pellets is the reason for the electroless reduction suppression.

Voltammetry can be used to obtain a better understanding of PEI's role in AuNW growth. Voltammograms were recorded at -20 mV/s for electrodeposition baths with varying PEI, as shown in curves C1 through C4 of Figure 4.7. Curve C1, for the solution containing no PEI, shows a peak at -0.91 V with respect to the RE, corresponding to gold cathodic reduction. C2 is drawn for the maximum PEI concentration, 0.1

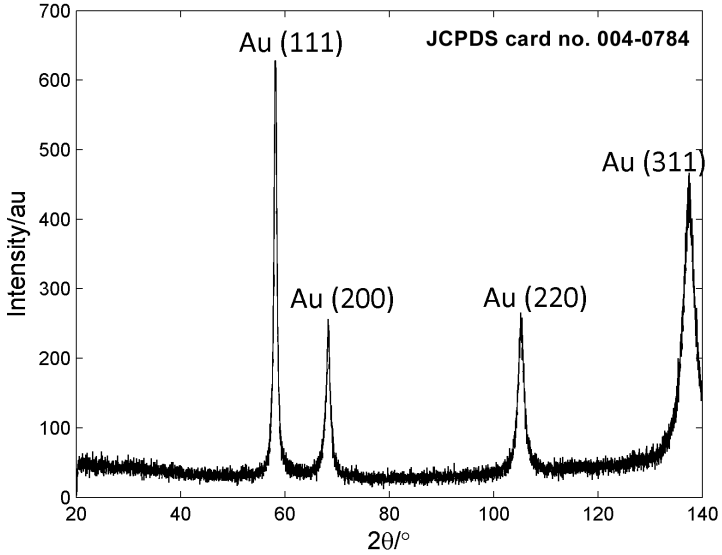

Figure 4.5: Powder XRD data for AuNWs taken from specimen electroplated at -0.95 V and PEI content of 0.05 vol.%.

vol.% at which AuNWs could successfully be grown. The bath with 0.1 vol.% PEI concentration revealed a peak at -0.95 V indicating a shift to more negative potential. This increase in potential is required to overcome the partial passivation of the electrode surface due to coverage with a very thin layer of PEI. This interpretation is strengthened by evidence from curves C3 and C4. C3 obtained at a somewhat higher PEI concentration of 0.2 vol.% and C4 at a much higher value of 1.0 vol.%, both do not show a cathodic current corresponding to the initiation of reduction, until a much larger negative voltage is applied. Also, FESEM/EDX results for specimens with the PEI concentrations of C3 and C4 show no gold deposition (neither electroless nor electrodeposition) over the entire voltage range from -0.7 to -1 V. This set of results is consistent with the picture of gold surface passivation increasing with PEI concentration. Indeed, based on voltammetry curves, the surface of the electrode appears still able to reduce H^+ ions even when gold reduction from the large complex has stopped. This seems reasonable considering the size and diffusivity of protons compared to the gold sulfite complex.

When working with solutions containing <0.1 vol.%PEI, we observed that the surface of the Anodiscs turns black after gold electrodeposition, intensifying with an increase in plating time. A related observation is that of a dense black streak rising from cathode to the liquid surface. In earlier plating studies with gold sulfite

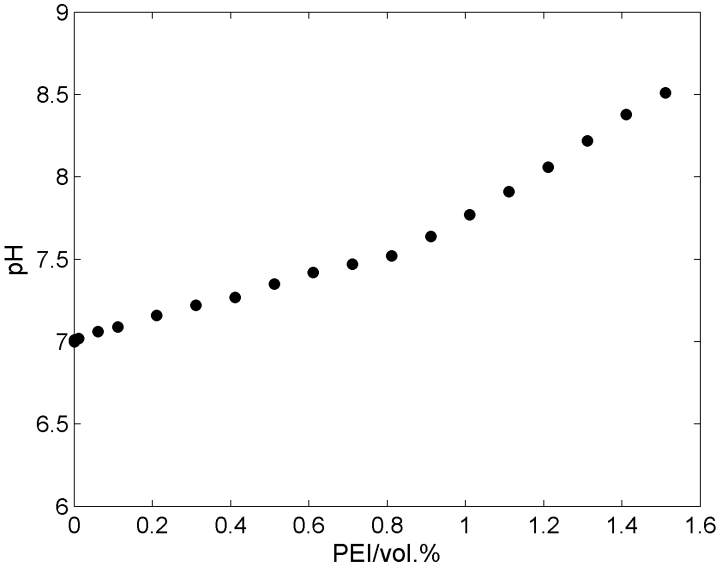

Figure 4.6: Measured pH values showing the effect of PEI concentration on the hydrogen activity in gold sulfite solution 5 g/L $HAuCl_4 \cdot 3\,H_2O$, 2 g/L EDTA, 65 g/L Na_2SO_3, 12.5 g/L K_2HPO_4.

solutions, Honma *et al.* [52, 53] show that a black colloidal precipitate of gold occurs as a result of disproportionation reaction of free Au^I in the solution:

$$3\,Au^+ \longrightarrow 2\,Au + Au^{3+}. \tag{4.3}$$

Equation 4.3 is an autocatalytic reaction [39, 76] for addition of metallic gold to the existing gold surface. This reaction is facilitated by the presence of hydrogen nanobubbles [76]. The black streak is locally concentrated gold (III) [52], which is formed on the surface of the cathode (AuNWs) and continuously snakes upwards to the surface of the solution. The only plausible explanation for this is that the buoyant stream of evolved hydrogen bubbles is carrying the black streak. This implies that pellet nuclei growth is inhibited, although there is a considerable evolution of hydrogen (also revealed in voltammograms). It appears likely that PEI passivates the newly formed pellet surfaces, preventing hydrogen bubbles from reaching the pellet nuclei surface and causing further pellet growth. Such electroless reduction has been described in detail in the report [76] of gold sulfite use without PEI. The higher the concentration of PEI, the smaller and less abundant the pellets.

Moreover, the black streak (or any turbidity) was not observered in experiments

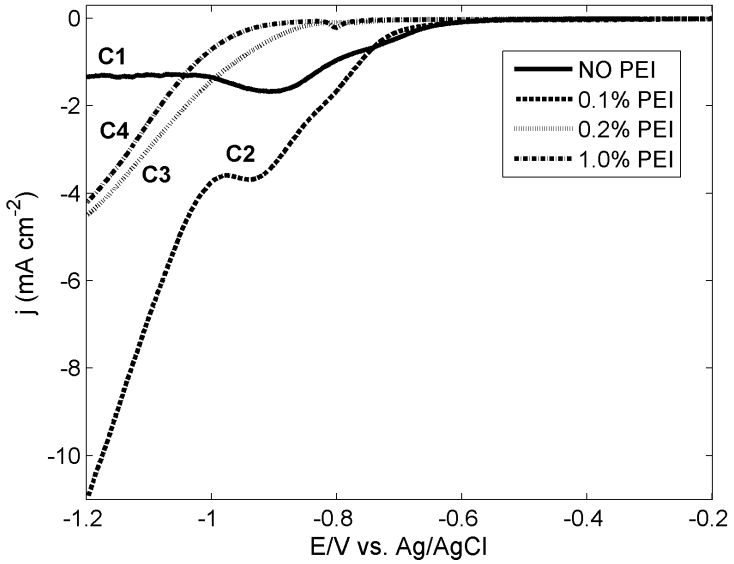

Figure 4.7: Voltammograms obtained from sulfite solutions with 0, 0.1, 0.2 and 1 vol.% PEI concentrations. Curves C3 and C4 show the clear effect of surface passivation of AuNW electrodes at increased concentrations of PEI.

with the solution containing more than 0.2 vol.% PEI, even at long times (over 4 hours) and high overvoltages where hydrogen evolution is noticeable. This suggests that at high concentrations of PEI, both electroless and electrochemical deposition of gold has been suppressed. This can be attributed to surface passivation of the Au pellet nuclei as well as the electrode by PEI. The passivation of the electrode surface with respect to gold reduction and its relatively higher activity for hydrogen reduction is also in agreement with the voltammetry results.

Our experiments establish that NWs of high quality can be repeatably produced, though only in a small fraction of the entire additive concentration range we have studied -such a window could be missed without careful experimentation. As an aside, the variable pellet size obtained by varying PEI concentration below 0.1 vol.%, shows that PEI can also be used in small amounts as a powerful tool to tune the size of pellet-like nanoparticles for applications of interest. The methods in this study of targeted additive concentration may serve as a starting example for improving electrodeposition of NWs and nanoparticles of other materials, particularly noble metals.

4.4 Conclusions

In this paper, we have presented results of successful growth of long, straight, separable, cylindrical AuNWs from a gold sulfite solution. It was shown that undesired hydrogen-evolution-driven electroless nucleation and growth create pellets all over the template surface. This prevented growth of NWs. Our experiments show that this problem can be overcome with repeated success by the addition of PEI, but only within a small window of concentration. AuNW electrodeposition ceases at higher concentrations. PEI concentration should be chosen so that it acts only as a surface passivator and does not interfere with the activity of the gold electrode in the process.

We found that the concentration range of $\sim$0.05 to 0.1 vol.% PEI can effectively control the nucleation and growth mechanism, resulting in growth of AuNWs without pellet formation. This additive range enables good control over the length of wires and prevents defects and cavities, making these NWs suitable for use in mechanics applications.

4.5 Acknowledgement

We gratefully acknowledge helpful discussions with D. Harrington, R. Herring and J. Austing, R. Sacci; and the use of A. Brolo's chemistry facility. This work was supported by Canadian funding agencies: NSERC, CFI, BCKDF and by the University of Victoria.

Chapter 5

Rhodium Nanowires

This chapter presents an article published [10] under the title of *Rhodium nanowires: Synthesis and nanostructure tailoring by controlling hydrogen evolution.* The article (Materials Letters 113, 152-155) is reproduced with permission from Elsevier.

Abstract

We report the use of rhodium sulfate solution for electrochemical synthesis of straight separable cylindrical rhodium nanowires that can be used as nanoresonators. We studied the effect of pH on the length uniformity and the effect of EDTA and polyethylenimine as additives on the development of the wire nanostructure. Multiscale frequency hydrogen bubble trapping and release was observed in the special case of a sulfate-based solution with 0.1 vol% polyethylenimine as an additive which results in formation of nanowires with ultrafine grain structure. The control over hydrogen co-reduction on the electrode surface and its bubble transport rate allowed for tailoring the nanostructure of the grown nanowires. Electrodeposition was performed at room temperature to avoid dissolution of the porous alumina template.

5.1 Introduction

Rhodium nanowires (RhNWs) benefit from desirable mechanical properties as resonant mass sensor as they can retain high quality factor (Q-factor) from high vacuum to near atmospheric pressures [3]. Moreover, rhodium's chemical stability [17] and the relatively high strength of its bond with the thiol group [18] enables a range of

surface functionalization chemistries [8] particularly for biomolecular diagnosis.

Rhodium is also a well known catalyst in petrochemical industry [88]. Electrolessly fabricated RhNPs have been used on glassy carbon modified electrodes [89] and also on the surface of multiwall carbon nanotubes [90] for improving hydrogen peroxide detection. Porous rhodium nanotubes have also been synthesized electrolessly and used for the same application [91]. As a route to enhance catalytic properties as well as physical and mechanical properties, in this work we also show that the surface morphology, roughness and the nanostructure of RhNWs can be modified by changing the chemistry of the synthesis.

Straight, separable, cylindrical NWs with good length control are requested for mechanical applications such as nanoresonators [56] as well as for many sensing applications [3, 4, 8, 57–64]. Additionally, recent advances in directed-assembly techniques [3, 65, 66] has enabled large-area, low-cost fabrication of device chips, creating new opportunities for the use of these NWs.

Here, we demonstrate the electrochemical synthesis of RhNWs for the first time from a sulfate solution. We show that the nanostructure of these NWs can be tuned for various range of applications. We investigated the effect of polyethylenimine (PEI) and ethylenediaminetetraacetic acid (EDTA) on the nanostructure development of the grown NWs. We show that the pH of the bath can change the NW length uniformity which is a concern in mass production of NWs for directed assembly and many sensing platforms.

5.2 Material and Methods

5.2.1 Template Preparation

Nanoporous AAO membranes (Whatman), 60 μm thick with nominal pore diameter of 200 nm were used as templates. A silver layer, 500 nm thick, was deposited on one side of Anodiscs using an electron beam evaporator to serve as the working electrode. As commonly practiced, to avoid the undesirable branched region, silver was electrodeposited at -0.5 V cathodic potential with respect to reference electrode (RE) for 1 hour from commercially available Silver Cy-Less solution (Technic).

5.2.2 Electrodeposition

Electrodeposition was performed at room temperature in a custom-made Teflon cell with a standard three-electrode configuration using platinum gauze as counter electrode and NaCl-saturated Ag/AgCl as RE. RhNWs were electrodeposited into pores by applying voltages ranging from -75 to -400 mV with respect to the RE from a aqueous rhodium sulfate solution (RH221D from Technic). The dilutions were made so that all the final solutions contained 60 mM rhodium. Controlled amounts of sulfuric acid were added to the solution as recommended by the make-up solution manufacturer to enhance smoothness of the deposit. To alter the surface roughness of the RhNWs, EDTA (Caledon) at 5 g/L concentration was added to the solution for a number of experiments. PEI water solution (Sigma-Aldrich) was purchased to use as additive for enhancing hydrogen bubble formation. All electrochemical experiments were controlled by a potentiostat/galvanostat VersaSTAT 3 (Princeton Applied Research).

5.2.3 Characterization of NWs

After RhNW electrodeposition, the Anodiscs were snapped apart without use of any cutting tools, taking advantage of their brittleness. The cleaved Anodisc cross-sections were observed using Field Emission Scanning Electron Microscopy (FESEM, Hitachi S-4800) and color mapped with Energy Dispersive X-ray Spectroscopy (EDX, Bruker Quantax) for elemental composition analysis.

5.3 Results and Discussions

5.3.1 Sulfuric Acid Effect on Template Stability

For electrodeposition of rhodium from a sulfate solution, it is recommended that the vessel and plating solution be heated to 35°C or above [92]. It is also known that further decrease in pH by addition of sulfuric acid to the sulfate plating solution, can improve the rhodium deposit smoothness [92, 93]. However, the initial attempts to grow rhodium on top of silver in alumina template failed at 40°C due to dissolution of alumina.

In the succeeding experiments, alumina dissolution was avoided by decreasing the working temperature. Operating at room temperature, we were able to grow

RhNWs for prolonged times without dissolving the alumina template. Figure 5.1 shows an FESEM image of a bundle of RhNWs synthesised at room temperature from a solution with pH=1.1. The inset shows a single straight RhNW on a carbon-coated glass substrate. The average diameter of RhNWs was found to be ∼250 nm. For the goal of creating cylindrical cantilever resonators, the intent was to grow NWs to a desired length of at least 10 μm with which may be achieved by prolonging the deposition time.

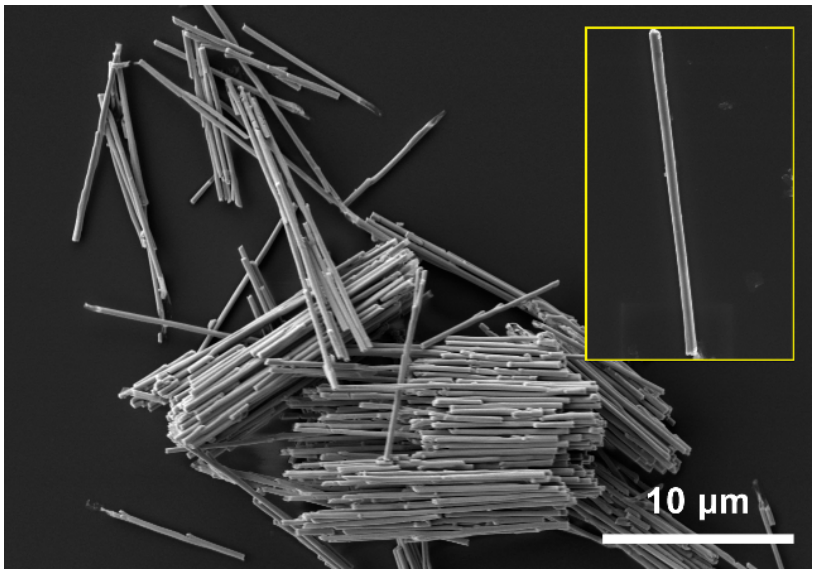

Figure 5.1: RhNWs grown at room temperature from a rhodium sulfate solution with pH=1.1 and -400 mV working potential with respect to Ag/AgCl RE.

5.3.2 Hydrogen Evolution Effect on NW Length Uniformity

Choosing an appropriate working potential for electrodeposition is not trivial. Higher working potentials accelerate the NW growth process but could enhance hydrogen bubbling, which in turn disrupts uniform deposition of rhodium across the template. Figure 5.2 shows current density transients obtained for RhNW growth at -75, -100 and -250 mV with respect to the RE. The *i-t* curves for the specimens synthesized at -250 mV exhibits periodic jumps in the current. This can be associated with hydrogen bubble release in the acidic bath. As electrodeposition proceeds, the evolved hydrogen gas builds up within the porous AAO template, narrowing ion transport paths and reducing the current gradually. Once the bubble size reaches a critical value it is suddenly released and the current returns to its base value.

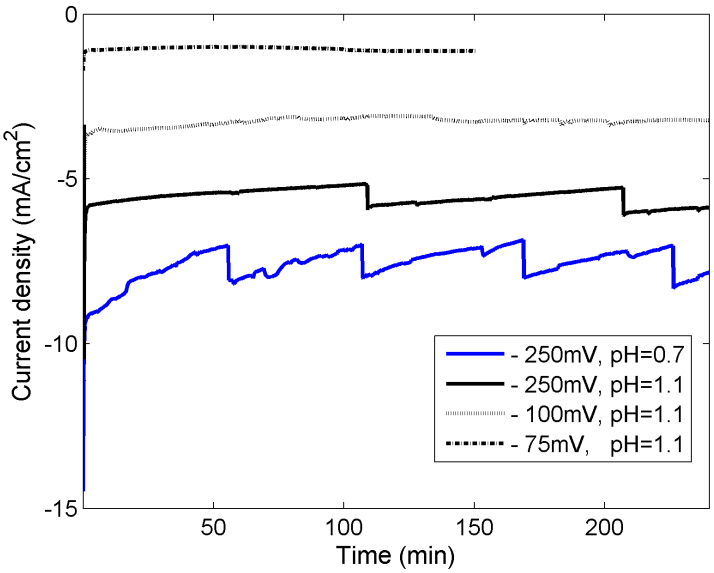

Figure 5.2: Current transients for RhNW electrodeposition obtained for various working potentials. Periodic hydrogen bubble release is revealed as steps in the current density. The periodicity and the height of steps are more pronounced at higher working potentials and lower pH.

This behavior became less observable at lower working potential and sulfuric acid content (higher pH). In Figure 5.2, the *i-t* curve at -250 mV for the solution with pH=0.7 (2 vol.% extra sulfuric acid added) as compared to the one with pH=1.1 (0.5 vol.% extra added sulfuric acid) at the same working potential, shows higher instability in the current and more frequent bubble release. This indicates that the bubble-induced non-uniformity in rhodium deposition is more significant at higher sulfuric acid content of the solution.

EDX color-mapped FESEM images of template cross-sections were obtained after RhNW growth for two different conditions: (A) at -100 mV from a solution with pH=0.7 for 40 minutes, and (B) at -250 mV from a solution with pH=1.1 for 240 minutes. The RhNW length uniformity in (A) was found to be less than in (B), despite the fact the specimen in (A) was electrodeposited at lower cathodic voltage compared to (B), that is -100 mV in place of -250 mV. In order to quantify the statistical uniformity of the NWs in each set, the length of 40 adjacent NWs were measured. The standard deviation was calculated and normalized by the average NW length for each set of NWs. The RhNWs in (A) and (B) showed normalized standard deviation values of 0.17 and 0.06, respectively. The much larger deviation in (A)

Table 5.1: Effect of sulfuric acid content on Rh deposition efficiency at -100 mV with respect to Ag/AgCl RE for 10 μm RhNW length.

pH	Deposition time (min)	Expected NW length (μm)	Average NW length (μm)	Rh deposition efficiency (%)
1.1	240	15.7	10	64
0.7	150	21.0	10	48

even when operated at lower overpotential and shorter time, shows that sulfuric acid content of the solution plays a key role in RhNW electrodeposition process. With less added acid, less hydrogen gas bubbles are formed, leading to higher uniformity of NW length even when working working at relatively higher overpotentials.

Additionally, the reduction of hydrogen at the cathode decreases rhodium deposition efficiency. In order to quantify RhNW plating efficiency, the average length of NWs grown from two different solutions at the same working potential, was measured. The expected NW length was calculated by recording the total charge consumed during the process. Table 5.1 shows that rhodium deposition efficiency reduces to 48% from 64% when NWs with average 10μm length are grown from a solution with pH=0.7 compared to 1.1.

5.3.3 Effect of EDTA and PEI on RhNW Surface Morphology

Controlling the surface morphology of a catalytic material is a powerful tool to manipulate its properties and enhance its performance as a catalyst. To alter the base surface morphology of the RhNWs, EDTA was added (5 g/L) to the sulfate solution. Figures 5.3A and 5.3B show FESEM images of the base surface of the grown RhNWs from a solution, with no added sulfuric acid without and with EDTA respectively. NWs synthesised from a solution with EDTA (shown in Figure 5.3B) exhibit roughened surface morphology compared to those of Figure 5.3A which are grown from a solution without EDTA. It is well-known that surface energy considerations are crucial in understanding the morphology of noble metal nanostructures [36]. The effect of EDTA on the roughness and grain morphology of other face-centered cubic materials such as platinum and gold has also been reported [94, 95]. As a common chelating and capping agent [96], EDTA can influence both the thermodynamics and kinetics of the metal reduction and growth.

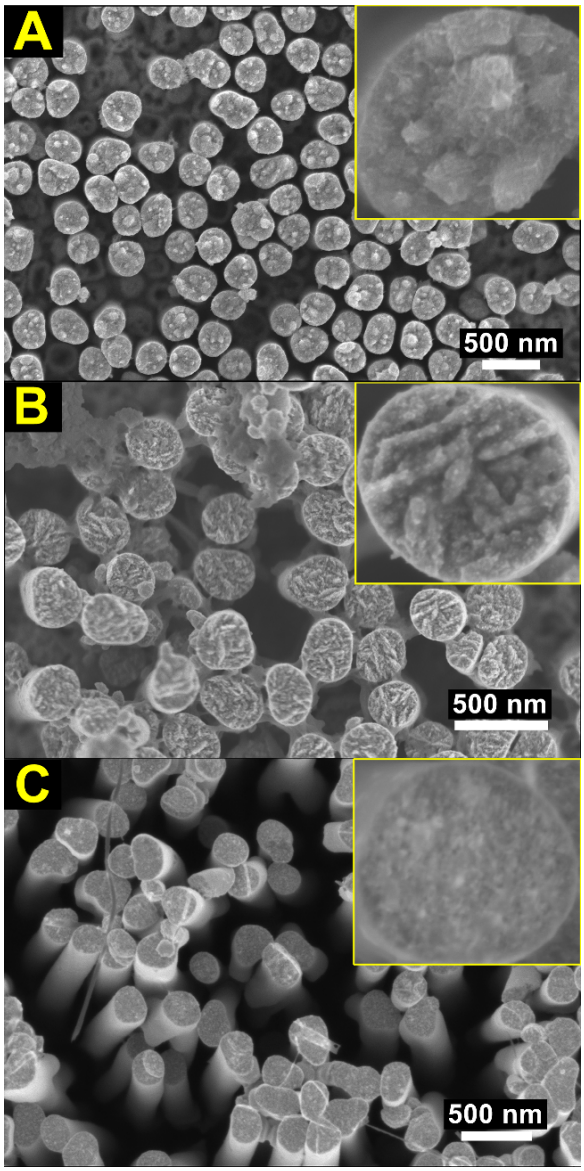

Figure 5.3: FESEM image of the base surface of RhNWs grown from a sulfate solution (A) without additive; (B) with EDTA (5 g/L) additive and (C) 0.1 vol.% PEI. The NW surface morphology roughness changes when EDTA is added to the solution in (B) whereas in (C) ultrafine grain structure was formed when PEI was added.

Figure 5.3C shows RhNWs obtained from a sulfate solution with 0.1 vol.% PEI added. It shows a distinctly surface morphology compared to Figure 5.3A and 5.3B, with a smoother surface and a distinguishable finer grain structure.

In order to better understand the effect of PEI on NW structure development, a chronoamperometric curve was recorded during NW electrodeposition. Figure 5.4

shows the current density vs electrodeposition time curves for identical solutions containing 0.1 vol.% PEI at -400 mV with respect to the RE where (A) an AAO template was used in the Teflon cell and (B) a millimeter-scale silver electrode was used in a beaker (as shown in Figure 5.4B). Compared to the *i-t* curves in Figure 5.2, the mean current density is significantly higher than the solutions without PEI. This can be related to the presence of amine groups in PEI structure which facilitates proton conductivity [97, 98] leading to enhanced hydrogen reduction. At points P1 and P2 in Figure 5.4A, elevated jumps in the current density are revealed similar to those of Figure 5.2. However, unlike the curves in Figure 5.2, new oscillations in the current density were observed along the curve in Figure 5.4A as a result of PEI addition and the confinement of the hydrogen reduction within AAO channels.

Use of a higher sampling rate for the nanoporous AAO template of Figure 5.4A, reveals a second (higher) frequency of the current density oscillations ($\sim$10 Hz), compared to the slower $\sim$0.03 Hz oscillation for the same Figure. However, for the millimeter-scale silver electrode in Figure 5.4B, these periodic oscillations were not observed.

The two different frequencies of oscillations in 5.4A are most likely related to the continuous trapping and release of the evolved hydrogen bubbles within AAO channels during the process. In the presence of PEI, the enhanced hydrogen reduction rate on the electrode surface significantly influences the co-reduction of rhodium when the bubbles are confined within the long and narrow pore channels. The surface of freshly-formed trapped hydrogen bubbles can act as a secondary template [76] for the reduction of rhodium and alter the structure of the growing NWs. Clearly, this change in the nanostructure can affect NW dissipation as well as other mechanical physical properties.

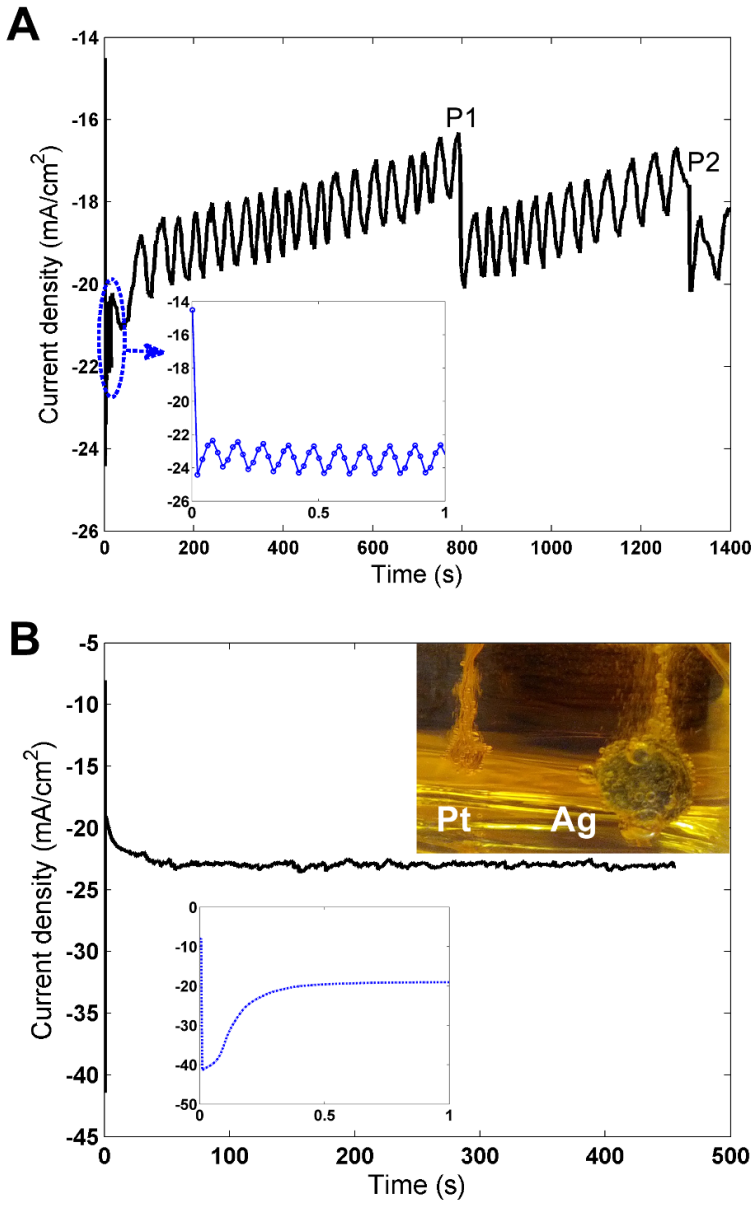

Figure 5.4: Current transients for Rh electrodeposition obtained at -400 mV with respect to Ag/AgCl RE. (A) in AAO nanoporous template and (B) using a silver electrode in a beaker. Periodic hydrogen bubble release is revealed at points P1 and P2 as steps in the current density. Insets: the inception of the electrodeposition process with data points collected every 0.02 second.

5.4 Conclusions

We have synthesized straight separable cylindrical RhNWs from a sulfate solution which can be used in nanoresonance applications. The effect of sulfuric acid content and working potential on hydrogen evolution and the NW length uniformity was demonstrated. The NW surface morphology was altered by adding EDTA as roughening reagent which makes the RhNWs more suitable for catalysis applications. It was shown that the use of PEI can result in the enhanced hydrogen reduction and multiscale frequency trap and release of the bubbles. This directly influences the co-reduction of rhodium on the electrode surface and alters the nanostructure development of the growing RhNWs.

5.5 Acknowledgement

We gratefully acknowledge helpful discussions with D. Harrington and the use of A. Brolo's chemistry facility. This work was supported by Canadian funding agencies: NSERC, CFI, BCKDF and the University of Victoria.

Chapter 6

Electrochemical Nanowire Clamping for Resonance Measurement

This chapter describes the NW clamping process as a part of a hybrid integration method that has been developed by Li *et al.* [3, 4]. In this method, off-chip synthesized NWs are fabricated at low cost. Directed assembly also uses low-cost conventional top-down microfabrication to create devices using electrohydrodynamic forces. Detailed description of the hybrid integration scheme has been the focus of my colleague Mahshid Sam and will be described in her PhD dissertation.

For the device fabrication, three separate mechanisms are combined to achieve high-yield NW resonator integration over centimeter-scale chip areas. NW assembly, patterning the clamp windows, and electrodepositing the metal clamp.

Spatially confined electric fields created by applying an AC bias to the interdigitated guiding electrodes induce long-range dielectrophoretic forces [6] that are used to attract and orient the NWs in the direction of the field gradient[1].

Prior to the clamping step, the NWs assembled in the wells were retained there by the capillary forces exerted on the NWs as the solution in the wells evaporated, while the misaligned NWs were found in other regions of the chip. NW resonator integration was completed by electrodepositing metal clamps in windows defined at one end of the NWs aligned in each well and dissolving the photoresist layers.

[1]Detailed description given in: Mahshid Sam, Nima Moghimian, Rustom B. Bhiladvala, "Field Directed Assembly of Nanowires: Estimating Directors, Disruptors and Yield Indices Maximizes Device Yield", prepared for submission to *Nano Letters*, 2015.

6.1 Nanoresonator Directed Assembly

Directed assembly is one of the nanofabrication techniques that bridges top-down and bottom-up strategies to create opportunities for fabricating nanostructures at lower cost compared to the high resolution top-down assembly [3, 99]. In directed assembly, photolithography allows full-wafer coverage of the substrate with gold metal pads and the electrical bus bars to supply voltage to them. Previously made NWs are then assembled on the substrate by applying electric field through the busbars. The assembly of NWs contains four main steps: fabricating a patterned substrate for NWs positioning, NWs assembly, patterning the clamp windows and electrodepositing the metal clamp. The assembled NWs can then be characterized by microscopy and electrical measurements.

Figure 6.1 shows the setup for NWs positioning and assembly by applying an electric field using a probe-station. A drop of NWs suspension in ethanol is placed on microscale electrodes where an electric field is applied. The NWs in the alcohol are directed to predetermined locations and are suspended over the electrodes. After the assembly, the solvent is allowed to evaporate. When an AC electric field is applied to a medium including NWs, an electric dipole is induced to enable dielectrophoresis, which attracts and orients the nanostrucures to the electrodes. The magnitude of the dipole depends on the voltage frequency, material properties and electrode geometry [86].

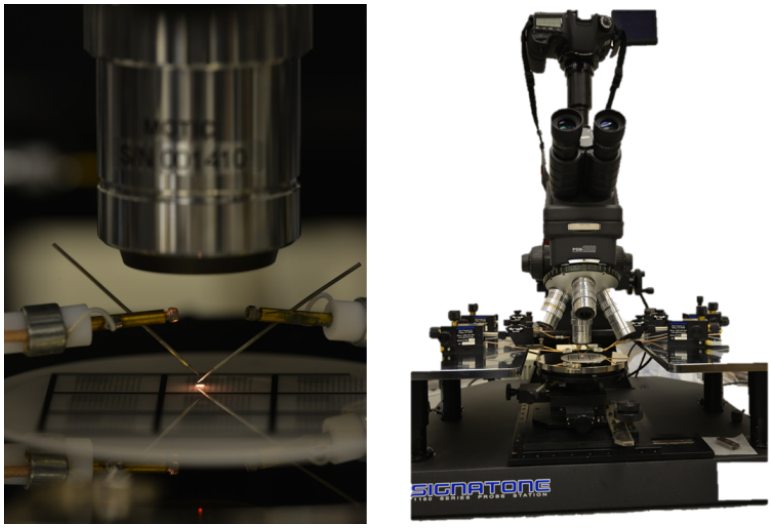

Figure 6.1: Probe-station used for positioning NWs onto target locations of resonator device chip.

The probe-station is equipped with a microscope for observing the NW assembly process and with a function generator for applying the AC voltage. For the electrode patterns described above, an AC voltage with ∼7 V_{RMS} at various frequencies was applied between the interdigitated electrodes. A drop of diluted NW suspension (2-10 μL for a chip with a circular area of 1 cm diameter was dispersed inside and the area marked with a dam. The NW concentration was adjusted to prevent the formation of NW chains at high concentrations, or low NW assembly yield at low concentrations. The AC electric field produced a spatially-confined electric field gradient in the NW suspension, which attracted and oriented the NWs to align with the field gradient.

Importantly, the misaligned NWs that are not attached to the substrate by the metal clamp are lifted off the chip when the photoresist was dissolved, giving high yields of single NW assembly. In addition to mechanically attaching the NWs to the substrate, the metal clamps also served as contacts to electrically drive the resonant device oscillations.

After positioning the NWs into the patterned wells, the next step is opening the clamp site by exposing the photoresist using a photolithography mask. The exposed polymer is removed to prepare the clamp box for electrodeposition of the clamp material.

6.2 Device Design

Two NW wafer designs were used in this work for two different purposes. In the first design (D1), a wafer with arrays of highly packed interdigitated electrode were patterned mainly for multiplex sensing. In the second design (D2), wafers with large spaces between the NWs were patterned for quick prototyping and molecular gas dynamics measurements. Each wafer contains six identical NW chips. Table 6.2 summarizes the specifications of the NW chips obtained from the D1 and D2 wafers.

Table 6.1: Specifications of a single NW chip in each of the two wafer designs used in this work. Each wafer contains 6 chips.

Wafer design	Clamp box size	Number of clamp sites per chip	Total electroactive area (cm^2)
D1	40 μm × 80 μm	9600	3.1×10^{-1}
D2	20 μm × 20 μm	20	8.0×10^{-5}

The D2 design is more convenient for rapid prototyping and measurements of NW resonance frequency from each batch of NWs. The clamp condition had to be readjusted for the newer design (D2) as the electroactive surface areas are of different orders.

6.3 Nanowire Clamping

Clamping NWs is essential for obtaining a rigid support that approximates the fixed boundary condition for a cantilevered nanoresonator. To do so, a critical clamp size must be reached. Qin *et al.*, [100] have shown the effect of clamping size on resonance frequency and measured Young's modulus of zinc oxide NWs. They performed the resonance tests in *situ* inside a scanning electron microscope. The NWs were cantilevered on a tungsten probe by electron-beam-induced deposition (EBID) of hydrocarbon. They demonstrated that the resonance frequency increases with increasing clamp size until reaching a critical clamp size. The critical clamp size is identified as a function of NW diameter and NW Young's modulus [100].

The importance of considering the effect of clamping in resonance measurements is that the uncertainty in boundary condition could lead to considerable errors in the measurements of Young's modulus as exemplified in [100].

An ideal clamp is necessary to satisfy the Euler-Bernoulli elastic beam behavior. Many fabrication approaches lead to nonideal anchoring using adhesion forces or metal/oxide deposition, introducing interfacial mechanical instabilities and additional energy dissipation mechanisms in resonant systems [101]. In contrast, our strategy produces nanobeams solidly connected to pads allowing the direct integration of chemically synthesized nanoscale building blocks into functional NEMS.

Several approaches have been employed to obtain a secure clamp bond. For example Belov *et al.*, [102] have used a method involving the directed growth of suspended horizontal NWs. In this approach, catalytic nanoparticles are formed on the sidewalls of prefabricated trenches, followed by the lateral epitaxial growth of the cantilevered NWs. Because the NWs are grown epitaxially from the surface, the bond to the surface at the clamping point is rigid. However, the direction of growth with respect to the pad in the CVD process is not entirely controllable and significantly limits the yield of functional resonating NWs.

The NW clamps in this work were made by use of electrodeposition from aqueous metal ion solutions. In this method, we obtain an intimate contact all around the

clamp-NW interface, which allows a repeatable approximation to the fixed boundary condition approximation.

Design guidelines should be provided for any clamping methods to ensure the satisfaction of clamp requirements. The electrodeposition conditions such as current density and ionic concentrations directly influence the morphology and quality of the deposited material. Rough (bumpy) or dendritic surfaces can be produced under certain electrochemical conditions. The deposition time determines the height of the deposited clamp material, however, the deposition rate and morphology are not always homogeneous over the electroactive surface area. This may lead to low quality or asymmetric clamp (discussed in section 6.5), which is not reliable for resonance measurements. The suitable operating conditions differ for different materials and different solution compositions.

6.4 Clamp Materials

A combination of chemical resistance, high elastic modulus as well as low material cost can define a criterion for clamp electrodeposit material selection. Among the readily available materials (in the context of nanoresonator fabrication) that can be easily electrodeposited as clamp and have a high chemical resistance, three materials can be considered: gold, silver and rhodium. The elastic moduli of gold, silver and rhodium along with their prices are listed in Table 6.4.

Table 6.2: Clamp electrodeposition candidate materials for NW resonator device fabrication. The prices are average for December 2014 traded at London Metal Exchange.

Material	Elastic modulus (GPa)	Price (USD/oz)
Ag	76	16
Au	82	1200
Rh	379	1185

Table 6.4 shows that rhodium has significantly higher elastic modulus than gold and silver while its price is very close to the price of the gold. Silver is the cheapest material among the three with its elastic modulus being about the same as gold. This suggests that silver can be a good choice where the price is concerned e.g., when fabricating large area arrays of NW sensors. Also, rhodium is probably the best choice when rigidity of the clamp is the most critical factor. Gold is not the best

choice considering the price paid for the elastic modulus gained. However, among these noble metals, gold is the only material used so far for electrochemical clamping of NW resonator sensor devices [3, 4, 8]. The reason most probably is the well-known chemistry of the electrochemical process. Electrodeposition of gold from solutions with cyanide complex has been used for years in electronics industry. When used as NW clamp, the deposit obtained from cyanide complex also shows excellent quality in terms of smoothness, uniformity and NW coverage. However, cyanide-based solutions are highly toxic (as discussed in [9] presented in Chapter 4). Other complexes of gold such as chloride and sulfite are orders of magnitude less stable than gold cyanide [39]. The stability constants[2] of gold chloride $AuCl_2^-$ [70] and gold sulfite are K=10^9 and K=10^{10}, respectively , compared to that of cyanide K=10^{26} [39].

Low stability constant of non-cyanide complexes of gold can result in non-compact (dendritic) or fibrous clamp deposits, which are not suitable for intimate coverage of NWs. In fact a large number of variables in the electrodeposition process have bearing on the structure. These include: metal-ion concentration, additives, current density, temperature, agitation and polarization [1].

Rhodium has not been tried as a clamp material most likely because of its relatively high price (historically expensive). However, it can be a good choice in cases where the price is not the most important factor. Rhodium electrodeposition is also a well-developed process as the material is largely used for decorative electroplating. Silver, is a good trade-off. It has a bulk modulus close to gold at about 1/70 of the price of gold.

6.4.1 Silver as a Clamp Material

We have examined several working conditions for the electrodeposition of silver as a clamp material for nanoresonator devices. We have used commercially available succinimide $Ag(C_4H_5NO_2)_2$ silver solution with silver solubility close to silver cyanide and higher than thiosulfate and dimethyl-hydantoin.

Historically electrodeposition of silver started with the double-silver cyanide complex $KAg(CN)_2$ with excess free cyanide. Although this bath is still one the more commonly-used ones, many other baths have been proposed for silver electrodeposition over the years [39]. In some cases dendritic deposition of silver may be obtained

[2]A stability constant is an equilibrium constant for the formation of a complex in solution. It is a measure of the strength of the interaction between the reagents that come together to form the complex.

most frequently. Ideally dense pore-free coating is desired.

We have found that in order to obtain an intimate clamp coverage and a smooth deposit, electrochemical parameters such as current density should be optimized. Our studies show that the quality of the clamp is highly sensitive to the operating conditions of the electrochemical process especially when the relative surface area of the deposit growth is small (ranging $\sim 10^{-4}$–10^{-1} cm^2).

Figure 6.2 shows how a change in the electrochemical conditions can change the morphology of the silver electrodeposit.

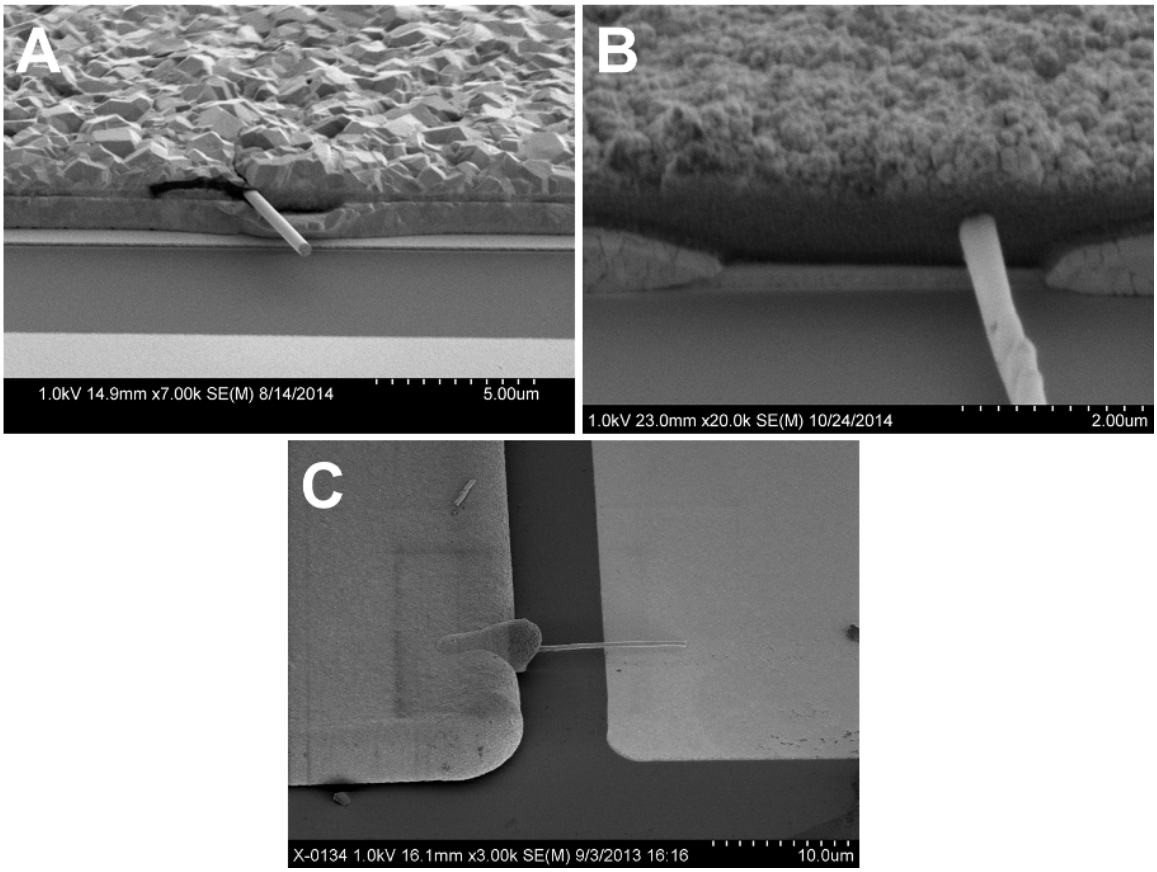

Figure 6.2: Silver Clamps from Ag Cyless (succinimide) solution electrodeposited at various conditions (A) 3.3×10^{-2} mA/cm^2 current density, no agitation, room temperature, (B) same current density, agitated, T=40°C, (C) current density 6.6 mA/cm^2 room temperature, no agitation.

6.4.2 Gold as a Clamp Material

Traditionally, gold has been electrodeposited from cyanide electrolytes where Au(I) is ligated with cyanide CN^-. The cyanide baths are exceptionally stable with the stability constants ranging 10^{26}–10^{38} [39, 47]. However, as mentioned previously, there is a growing concern regarding use of cyanide-based processes. As a result, non-cyanide gold solutions have lower toxicity and less strict handling and disposal requirements [47], and therefore, are preferred over cyanide-based solutions. The main problem with non-cyanide gold solutions is their lower stability constants. Green [70] has done a review on gold electrodeposition for microsystem applications using various gold electrodeposition baths.

The instability of gold solutions usually manifests itself in the formation of colloidal gold and is usually attributed to the disproportionation of Au(I) in the solution [9]. The formation of colloidal gold is undesirable in gold electrodeposition as the particles tend to increase surface roughness and promote formation of dendrites, rough nodules and other defects [70]. For instance, our attempts with gold chloride solution (SOL4 containing 6.25 g/L $HAuCl_4 \cdot 3\,H_2O$) did not result in a uniform and smooth deposit. Figure 6.3 shows that a extraneous dendritic needle-structured clamp was formed even at low current density of 3.3 mA/cm^2.

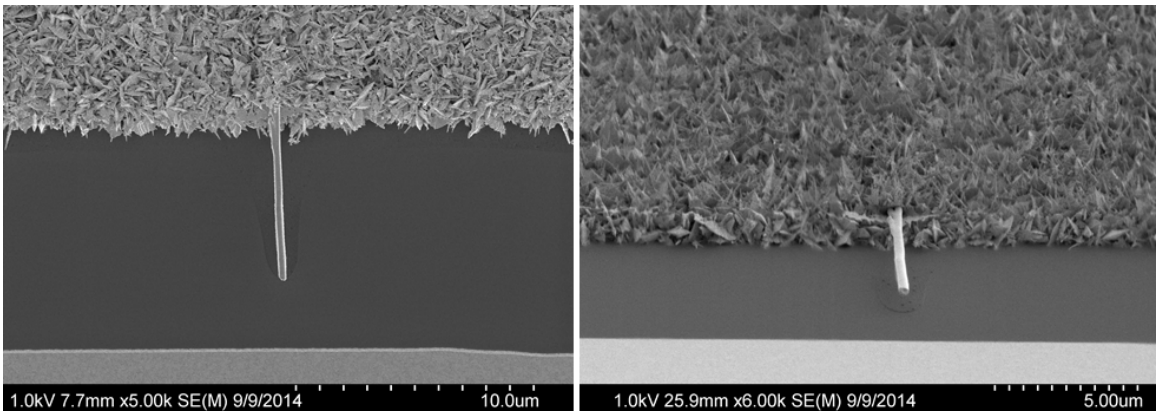

Figure 6.3: Top and side views of a dendritic gold clamp made at 3.3 mA/cm^2 from an additive-free 6.25 g/L$HAuCl_4 \cdot 3\,H_2O$ solution (SOL4) at room temperature with no agitation.

Figure 6.4 shows a closer look at the dendritic structure and its compactness.

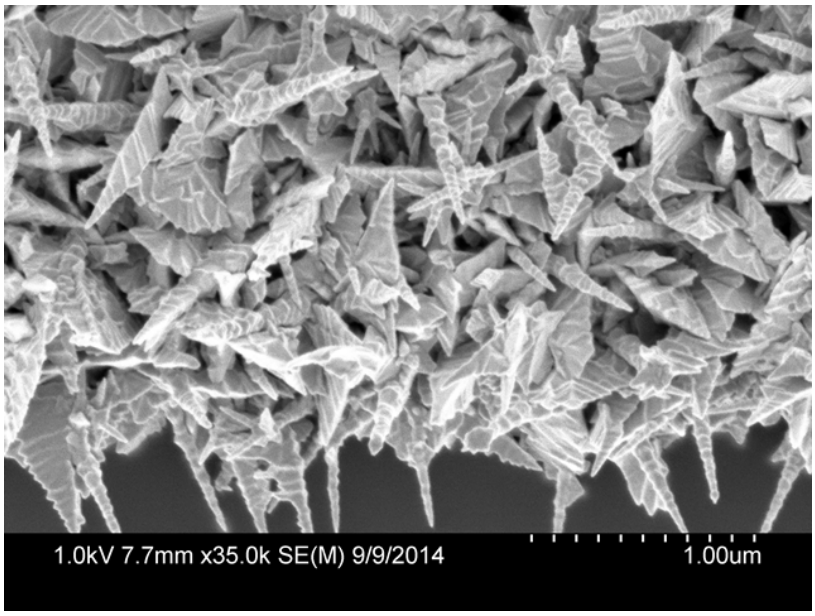

Figure 6.4: Non-compact dendiritic (needle-structured) gold electrodeposit obtained from a chloride solution (6.25 g/L $HAuCl_4 \cdot 3\,H_2O$) at 3.3 mA/cm^2.

We have also used EDTA as additive to the 6.25 g/L $HAuCl_4 \cdot 3\,H_2O$ and tried gold sulfite solution (composition used for gold NW growth) for clamping. The results can be found in Appendix F.

6.5 Clamp Defects

An electrodeposited clamp can be considered defective in several ways. Non-compact clamps, clamp out-box growth, asymmetric clamp, clamp with poor adhesion to the substrate and cracked clamps are typical examples of clamp defect identified in this study. The reason for some of these defects may not be very clear as several causes could be associated with them. The following sections introduce the above-mentioned defects mainly through SEM images.

6.5.1 Non-compact Dendritic Growth

Dendritic growth is a commonly observed result from the electrodeposition of many materials. Non-compact coverage of NWs introduces uncertainties on the boundary conditions of the resonator and therefore, should be avoided. Figure 6.5 shows dendritic silver clamps at three different magnifications. In Figure 6.5A, a silicon oxide

chip with smooth gold connection pads and dendritic silver clamps is shown. Figure 6.5B shows a side view of a single clamped NW that can be electrically driven using the gold pad underneath the NW. Figure 6.5C shows the NW from another perspective. It clearly shows that the clamp with the dendritic electrodeposit did not provide an intimate, symmetric coverage.

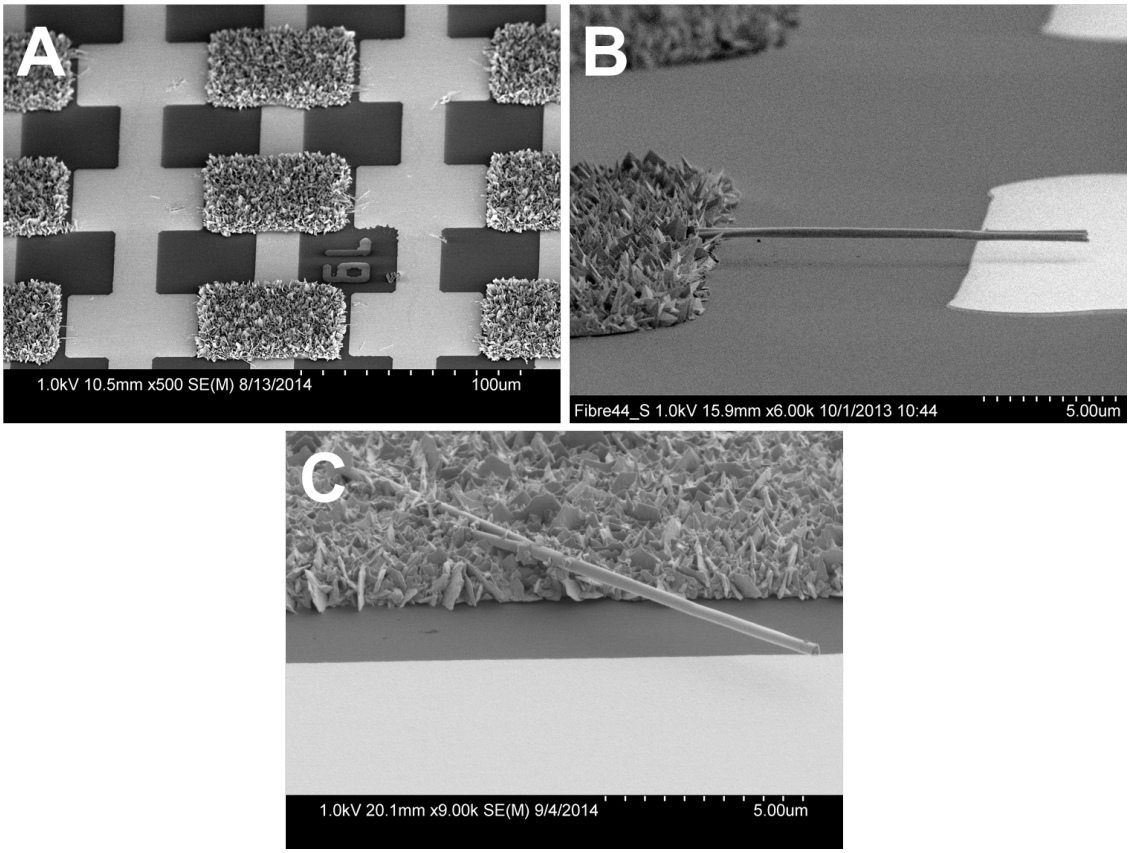

Figure 6.5: SEM images of a dendritic clamp electrodeposit at different magnifications and angles.

Another typical form of dendritic growth is shown in Figure 6.6. The electrodeposit form is closer to a flake-like shape rather than needle-dendrite shape shown in Figure 6.5. In the particular case of flake-like growth, the flakes are mostly formed on top of the clamp deposit. It was speculated from the image that the electrochemical growth of the clamp has had two distinct stages. In the first stage the electrodeposit was more compact and in the second stage a transition to dendritic growth occurred.

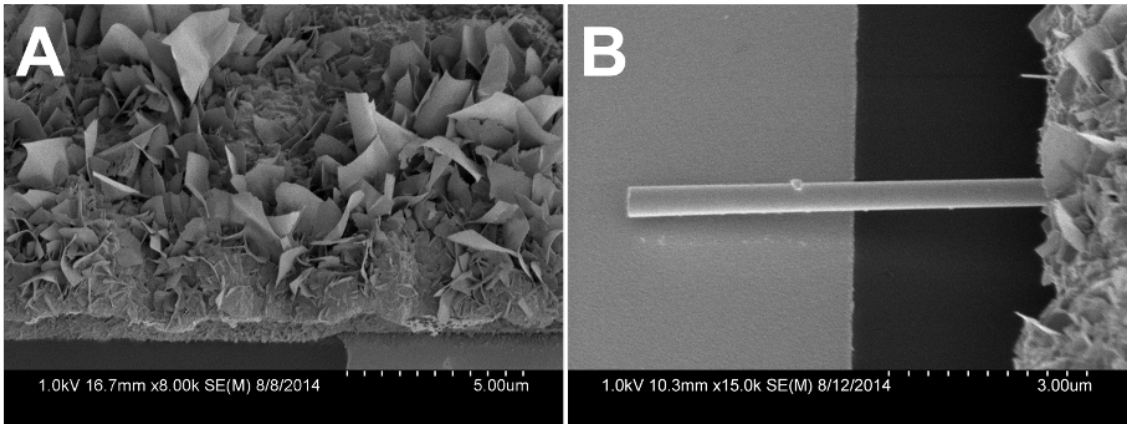

Figure 6.6: Flake-like dendrites observed on the top surface of clamp electrodeposits

In order to check for the two stage growth, a sharp probe tip (of the probe-station) was used to scratch the electrodeposited silver clamp. Figure 6.7 shows three different scratched clamps on a same chip at different angles. Figure 6.7A shows the top view of a cracked clamp. Figure 6.7B shows a side view of a kinked silver clamp after manipulations with the probe. Figure 6.7C more clearly reveals the structure of the clamp as two distinct layers. The lower silver layer is shinier and compact. The upper layer is darker and dendritic.

Several factors could contribute to the formation of these two distinct layers. The reduction in the concentration of the metal ion and change of pH over time are most likely to be the main reasons.

Compact and non-compact clamp electrodeposits can be quickly identified under a light microscope. The light scattering properties of a dendritic clamp provides a dark (almost black) color, whereas the compact growth can be seen as regular silver color. Figure 6.8 shows four light microscope images of different silver clamped electrodeposits on a silicon oxide chip. The silver clamp Figure 6.8A has a shiny silver color as the deposit is compact and smooth. The clamp in Figure 6.8B is still compact but less smooth. Figure 6.8C shows a deposit with partial surface dendrites seen mostly close to the sides. The clamp in Figure 6.8D was completely covered with dendritic silver electrodeposit.

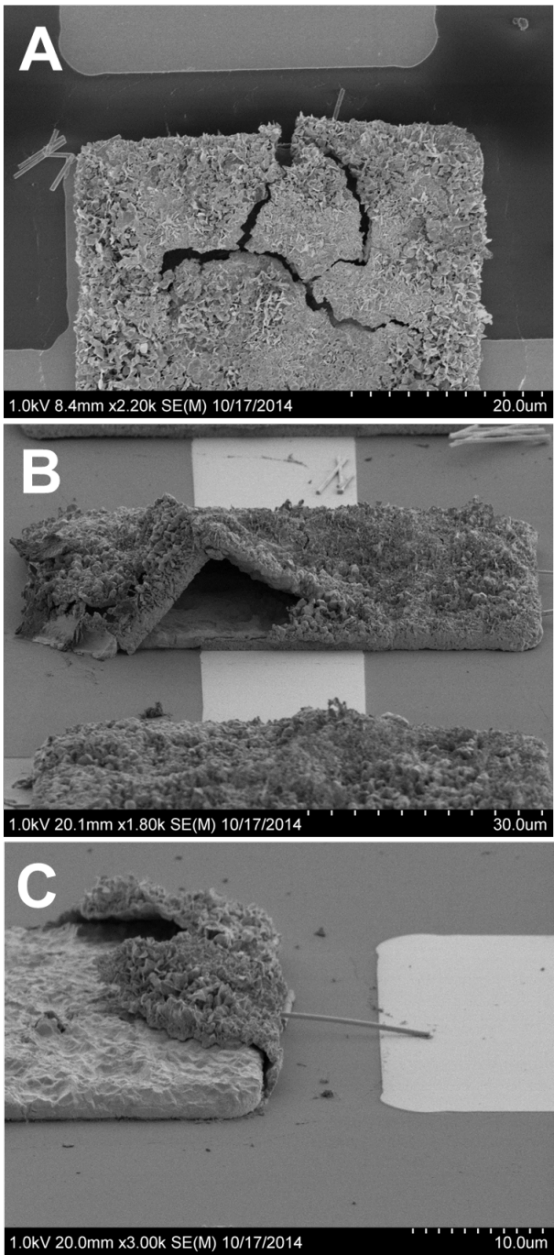

Figure 6.7: A silver clamp was scratched using a probe needle to reveal the clamp deposit structure. (A) top view of a clamp site cracked. The top view could give the impression that the entire clamp might be dendritic or fibrous. However, looking at images (B) and (C) it is seen that two distinct structures exist.

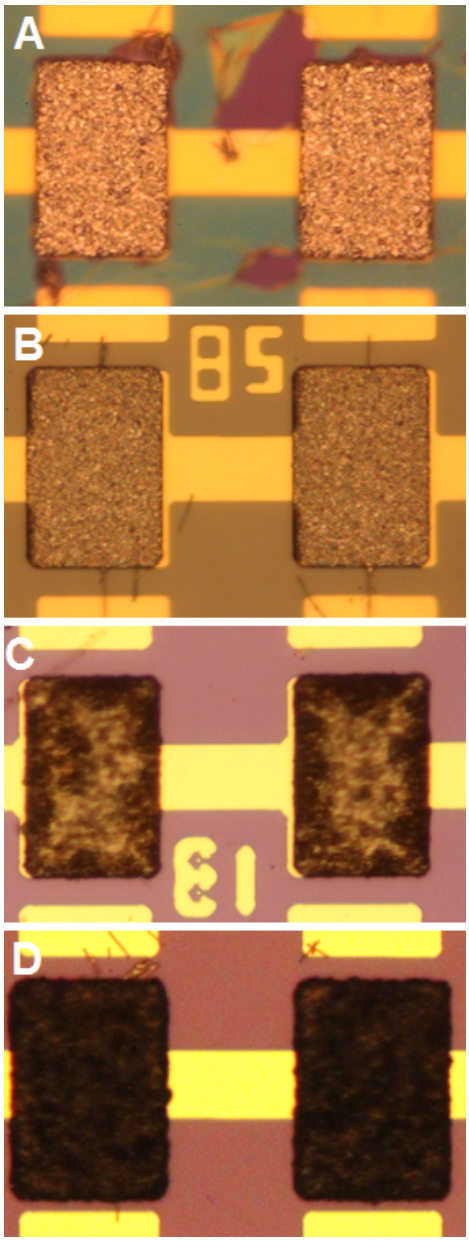

Figure 6.8: The difference in light scattering properties of non-compact dendrites and compact silver electrodeposits changes the color of the clamp region under the light microscope. Silver (A) smooth compact and (B) rough compact electroposits. (C) Partial formation silver dendrites. (D) Silver clamp completely covered with dendrites. Each clamp rectangle is 40 μm by 80 μm.

6.5.2 Clamp Out-box Growth

A metal clamp electrodeposit is intended to cover a NW by filling inside a rectangular clamp box (patterned by photoresist) and grow vertically. The growing clamp electrodeposit should not jacket the NW or cover any suspended part of NW outside the clamp box. Figure 6.9 shows two examples of clamp front overtake. In Figure 6.9A, small pieces of non-compact clamp electrodeposit have grown on the NW over a suspended length of $\sim$2 μm. In Figure 6.9B, although the clamp is smooth and compact, it has grown partly in a horizontal direction and covered asymmetrically a fraction of the suspended NW length.

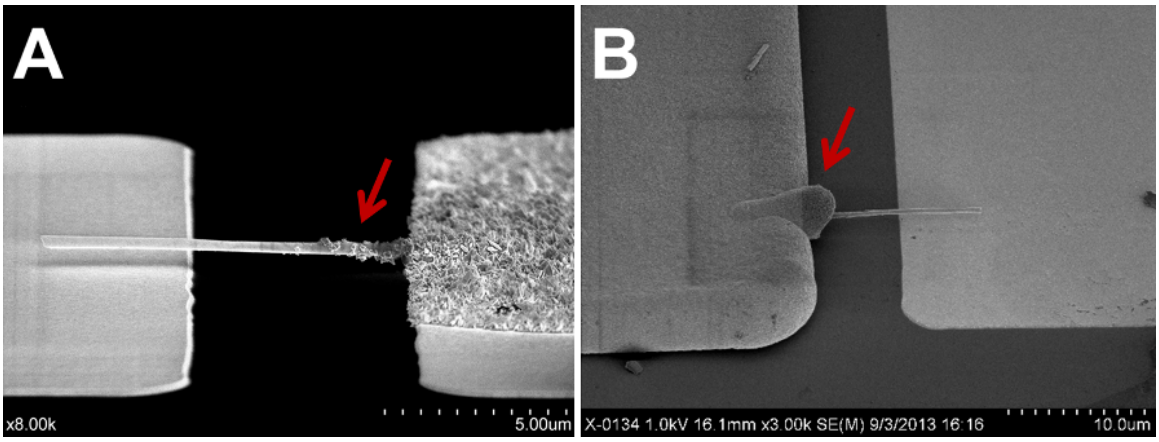

Figure 6.9: Clamp out-box growth defect marked with arrows for (A) non-compact and (B) compact electrodeposition.

The clamp out-box growth defect introduces uncertainties in the suspended length of the NW as well as the NW mass. Reasons for this defect could be misalignment during photolithography or poor adhesion at some locations of the interface between the two photoresist layers used. When the entire NW length is not covered with photoresist, the clamp electrodeposit can grow on the uncovered parts of NW.

6.5.3 Coverage Asymmetry

Another clamp defect that can be a major source of uncertainty in NW resonance calculation is asymmetry in the clamp coverage. Figure 6.10 shows two examples of asymmetrical clamps. In Figure 6.10A, a hollow region underneath the NW can be observed. This NW will have a longer effective length when moving down and a shorter effective length when it moves up. One reason for the formation of such hollow

regions, is the presence of broken pieces of other NWs in the clamp well. The small broken pieces may change the current distribution around the NW and therefore, alter the clamp nucleation and growth pattern.

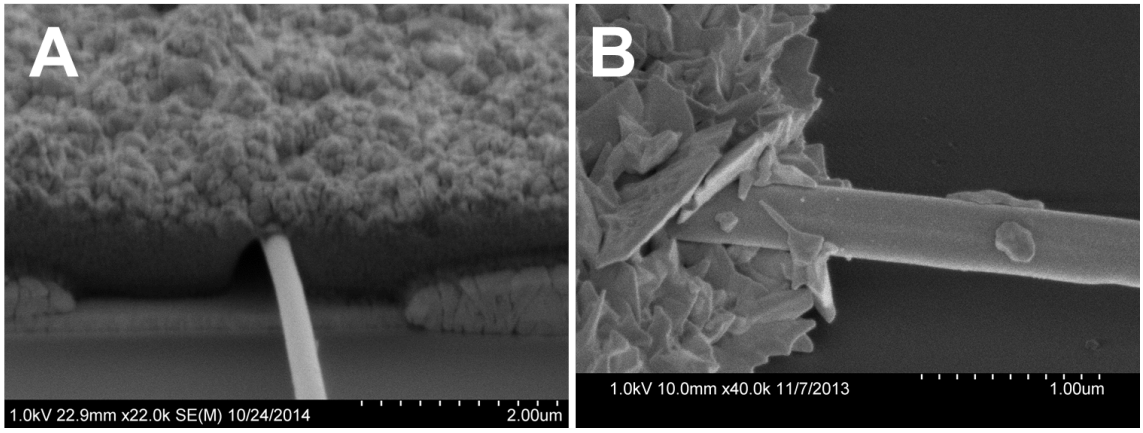

Figure 6.10: Twp examples of clamp asymmetry: (A) hollow region underneath the NW and (B) asymmetric coverage due to non-compact dendritic growth.

Figure 6.10B shows an asymmetrical clamp due to noncompact dendritic growth. The presence of dendrites disrupts the integrity of the clamp electrodeposit. This discontinuity in the electrodeposit results in asymmetrical coverage of NW that is especially important at the clamped-suspended interface of NW. Therefore, the electrochemical conditions (most importantly overpotential or current) for each clamp solution should be tuned to avoid dendritic growth.

6.5.4 Adhesion to the Substrate

As for any electrodeposited layer, the clamp should adhere firmly to the substrate. Figure 6.11 shows three examples of poor adhesion defect in NW clamping. Figure 6.11A shows a detached silver clamp. Figure 6.11B shows four smooth and compact silver clamps that are curled up at the corners and partially detached from the substrate. In Figure 6.11C, a dendritic electrodeposit is shown that has not covered the NW and is separated from the substrate.

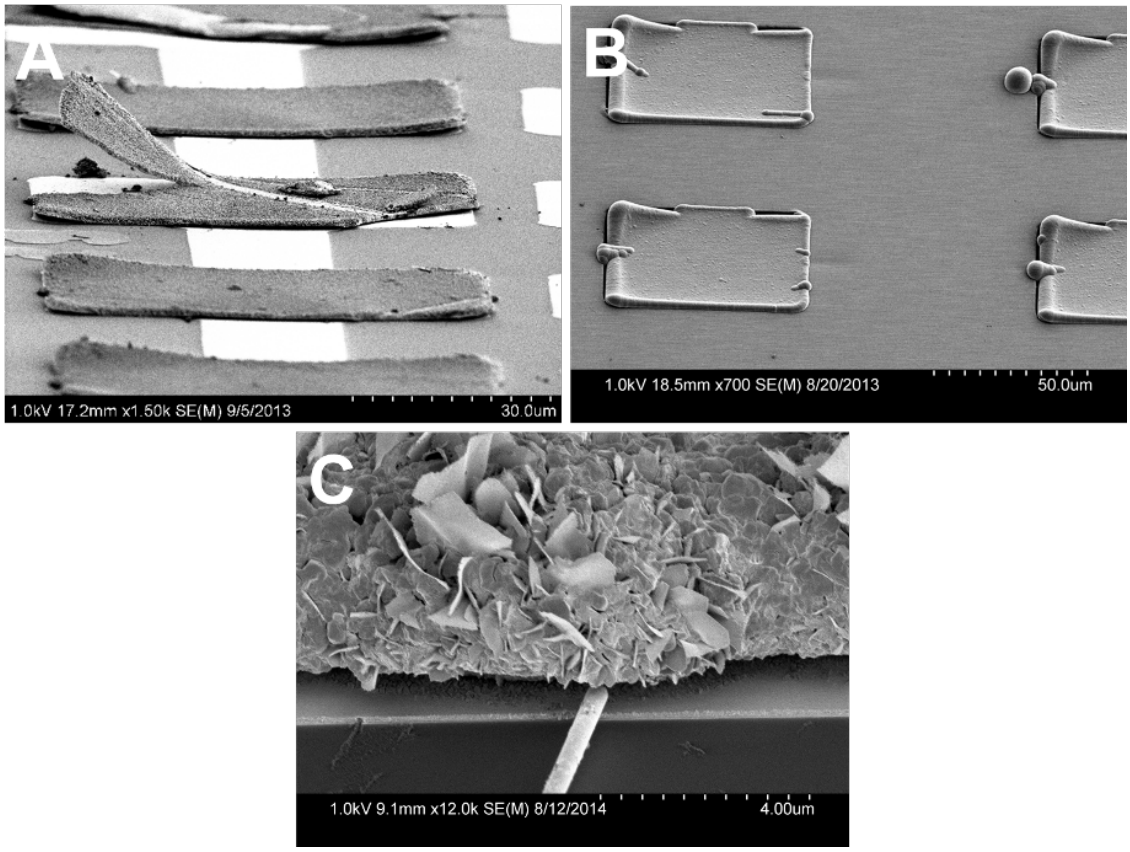

Figure 6.11: Examples of clamp poor adhesion.

Adhesion defects usually happen due to highly stressed deposits. The second common reason for poor adhesion of the clamp to substrate is poor surface quality or cleanness. The presence of polymeric residues on the gold surface can reduce the adhesion of silver to the gold substrate.

6.5.5 Cracked Clamp

Presence of cracks in the clamps can become an immediate problem by causing asymmetry and lowering the effective clamp stiffness. But, even if it is small and not an immediate concern, the clamp crack can become a fatigue issue over time. The relatively high frequency of NW oscillations will speed up the fatigue failure due to the rapid increase in the number of stress cycles. Figure 6.12 shows a crack in the clamp on the left side of the NW.

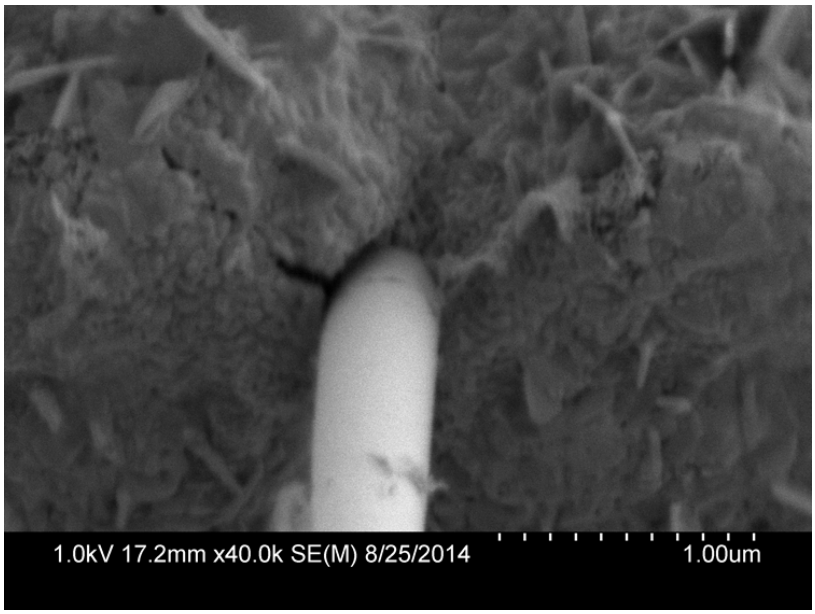

Figure 6.12: A cracked clamp.

Cracking in the non-compact clamps was found to be more probable than in the compact clamps. The local stresses induced during wet cleaning, rinsing and drying steps of nanoresonator fabrication may be a cause of crack formation in the clamp deposit. Also residual stresses during the electrodeposition can be another reason for crack initiation and propagation.

6.6 Device Fabrication Defects

Apart from the various defects in the electrodeposited clamps, other defects could occur during nanoresonator fabrication that can make the resonator dysfunctional. The residues from the NW synthesis, photolithography and microfabrication steps can be a source of device failure. Also, unintended electrical shorts created by NW bridging are among the nanoresonator device fabrication defects. This section briefly reviews these issues.

6.6.1 Polymeric Residues from Lithography

Photoresists are used in photolithography for patterning and fabrication of functional structures on a chip device. For each photoresist, a specific developer or remover is used. The clamp sites and later the clamped NWs are covered with photoresists at

different stages. In the process of removing the photoresist, polymeric residues may not be cleaned completely due to various reasons. Figure 6.13 shows a black "blanket" of polymer covering a successfully clamped NW.

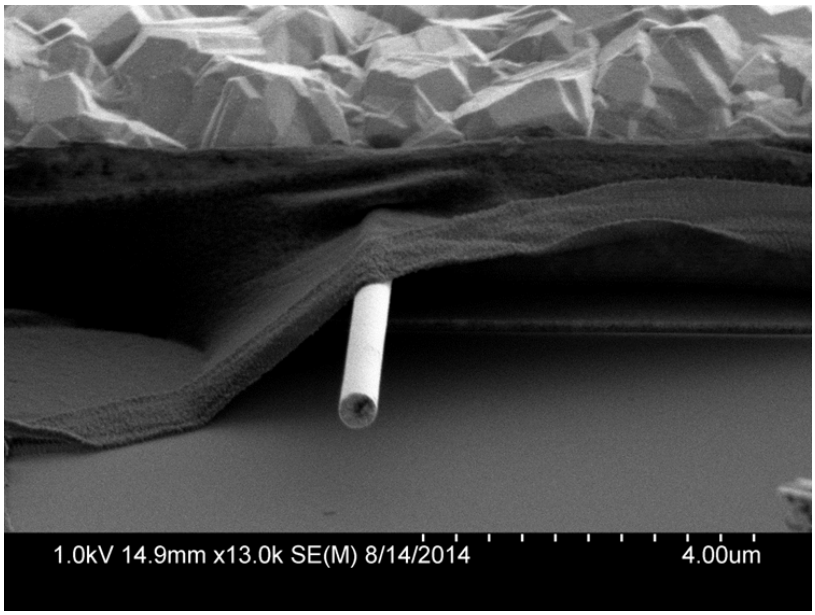

Figure 6.13: Fabrication defect: polymer blanket leftover from the photoresist removing process.

Polymeric contaminations should be removed ideally in one shot, because each incident of wet cleaning increases the chance of NW sticking to the gold pad. The forces due to the surface tension caused by the drying liquid, can make NW dysfunctional by bending and sticking it to the driving pad. Heating the substrate for polymer ashing or use of hot organic solvents could provide a solution to these sources of contamination.

6.6.2 Polymeric Residues from NW Synthesis

Dissolving the polycarbonate templates cleanly is usually more difficult than dissolving aluminium oxide templates. Organic residues as well as broken pieces from the NW synthesis process can also contaminate the NW resonator before clamping. Figure 6.14 shows a clamped NW with several contamination pieces of organic and metal residues.

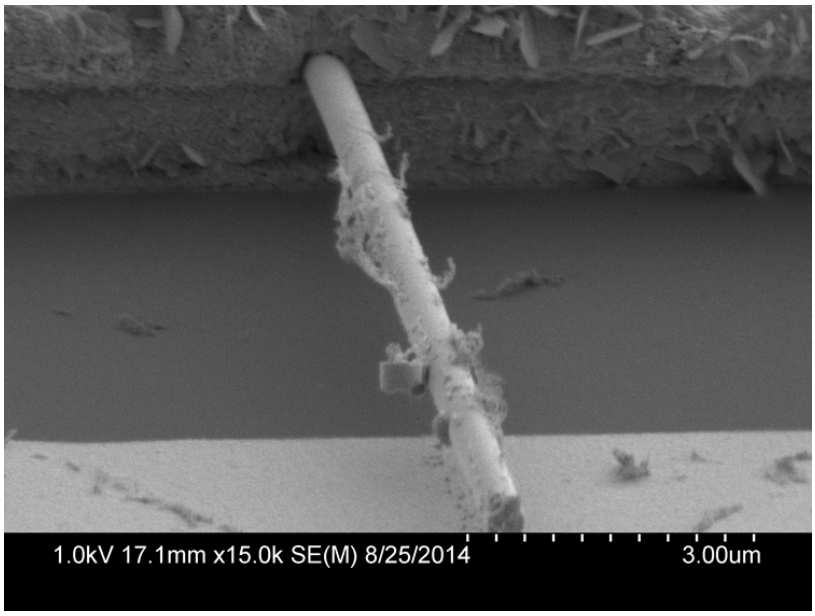

Figure 6.14: Contaminated NW with the residues from the NW synthesis process.

Appendix C.3 discusses various sources of contamination from NW extraction process. Template dissolution and NW extractions protocol–specially from polycarbonate templates, should be carefully followed in order to avoid contamination of the device at the microfabrication step.

6.6.3 NW Bridges and Shorts

Another typical issue that rises during the nanoresonator microfabrication process is the electrical shorts between the gold connection pads or clamps. The NWs that fall and attach to their driving pad will electrically short the electrical driving and positioning circuit of several other NWs. This has been a significant problem in D1 design and the main driving force to make wafers using the D2 design. In some cases the short circuit problem can be solved by use of post-clamp troubleshooting tools such as the probe-station needles or focused ion beam (FIB).

6.7 FIB as a Post-clamp Cleaning Tool

In this work, we have occasionally used FIB (Hitachi FB-2100) as a post-cleaning and troubleshooting tool for the first time. Although use of FIB in final mass production, would be time-consuming and expensive, in some cases FIB can be used to prevent the

dysfunction of several high-quality functional devices. We have used FIB for removing large pieces of dirt, minor cleaning, and a little more frequently for disconnecting the electrically shorted regions from the functional nanoresonators.

As mentioned in section 6.6.3, if a metal NW resonator adheres to the underlying electrode pad during integration or device operation, it could create a low-resistance path, or partial electrical shorting of electrodes over the entire chip. Depending on the location, in some cases, pairs of the electrodes were isolated by using a focused ion beam or sharp probe-station tip to troubleshoot shorting. FIB gives much more precise and cleaner cut. Figure 6.15 shows two side-by-side SEM images of a gold bar electrically disconnected by use of a focused ion beam. A fabrication beam of 40-1-150 (acceleration voltage of 40 kV – condenser lens on – objective aperture diameter 150 μm) was used at 60k magnification, for total 14 passes with 0.5 μs/pixel doze.

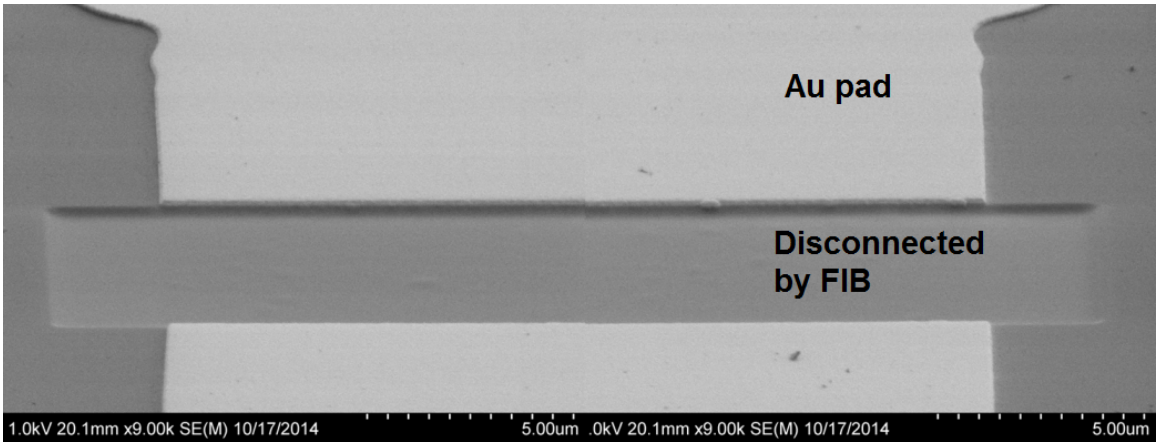

Figure 6.15: FIB-milled slot used for isolating two bridged pads by removing part of a gold connection bar. Two SEM images positioned side-by-side to depict the entire FIBed area. Fabrication beam 40-1-150 used at 60k magnification, for total 14 passes with 0.5 μs/pixel doze.

Using this approach, a number of NWs were isolated from the main chip and electrically connected in parallel for electrostatic actuation. This approach is time consuming and may even cause the failure of the NW device when high doses (combination of high accelerating voltage, current, exposure time or number of passes) of ion beam are used. Therefore, a new chip pattern was designed to reduce the chance of electrical shorts and if they occur, to make the isolation easier.

FIB was also used for removing large pieces of polymeric dirt residue attached to the NW resonator. Figure 6.16A and B show the front view of a clamped NW

before and after using FIB, respectively. Figure 6.16C and D, respectively, show the top view of the same NW before and after removing the large polymeric residue with FIB.

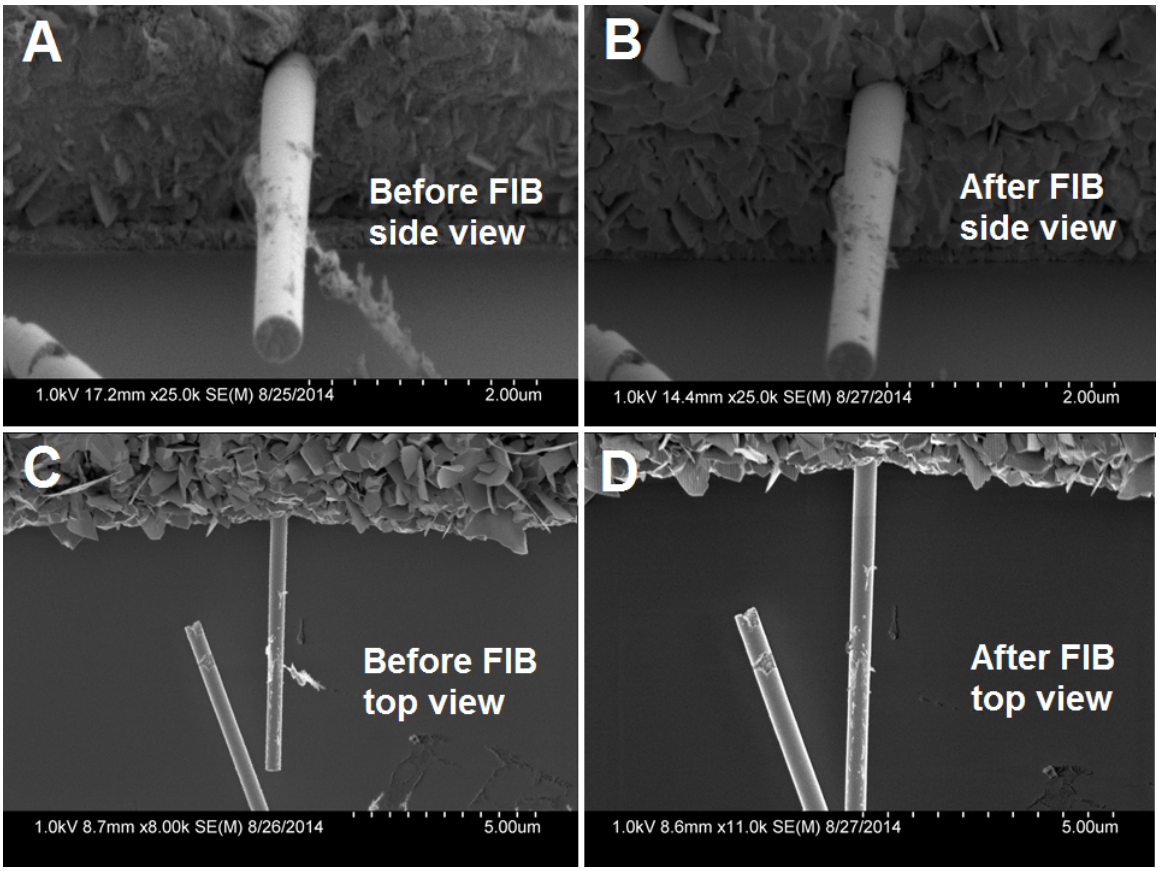

Figure 6.16: FIB successfully disconnected a large piece of polymeric residue. Ion beam 20-0-30 was used at 15kX magnification for 10 s.

Similarly, Figure 6.17A to D show the use of FIB for partial cleaning of small organic residues attached to the NW.

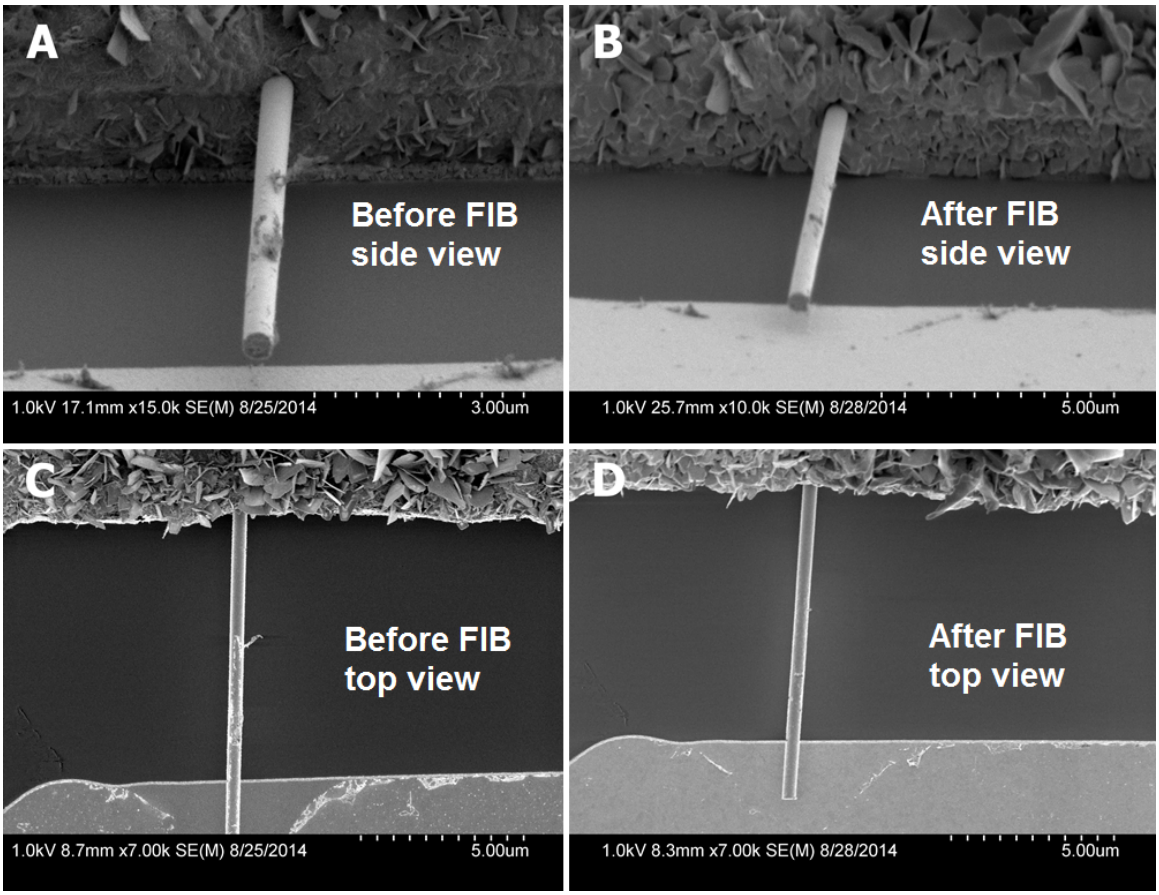

Figure 6.17: FIB successfully cleaned a small piece of polymer. Ion beam 20-0-30 was used at 15kX magnification for 5 s.

Nonetheless, the dose of ion beam used for cleaning is critical for the accomplishment of the cleaning process. It was found that if an ion beam is used for longer times, at higher accelerating voltages or at higher magnifications, the ions momentum might be enough to cause the NWs adhere to their underlying pad and become dysfunctional.

Figure 6.18A and B show the front view of a clamped NW before and after irradiation with FIB, respectively. Images of Figure 6.18C and D show the same NW at the same conditions from the top view. Although a good fraction of the NW contamination is removed (Figures 6.18B and D) but the tip of the NW has adhered to the gold pad due to a high dosage of beam used.

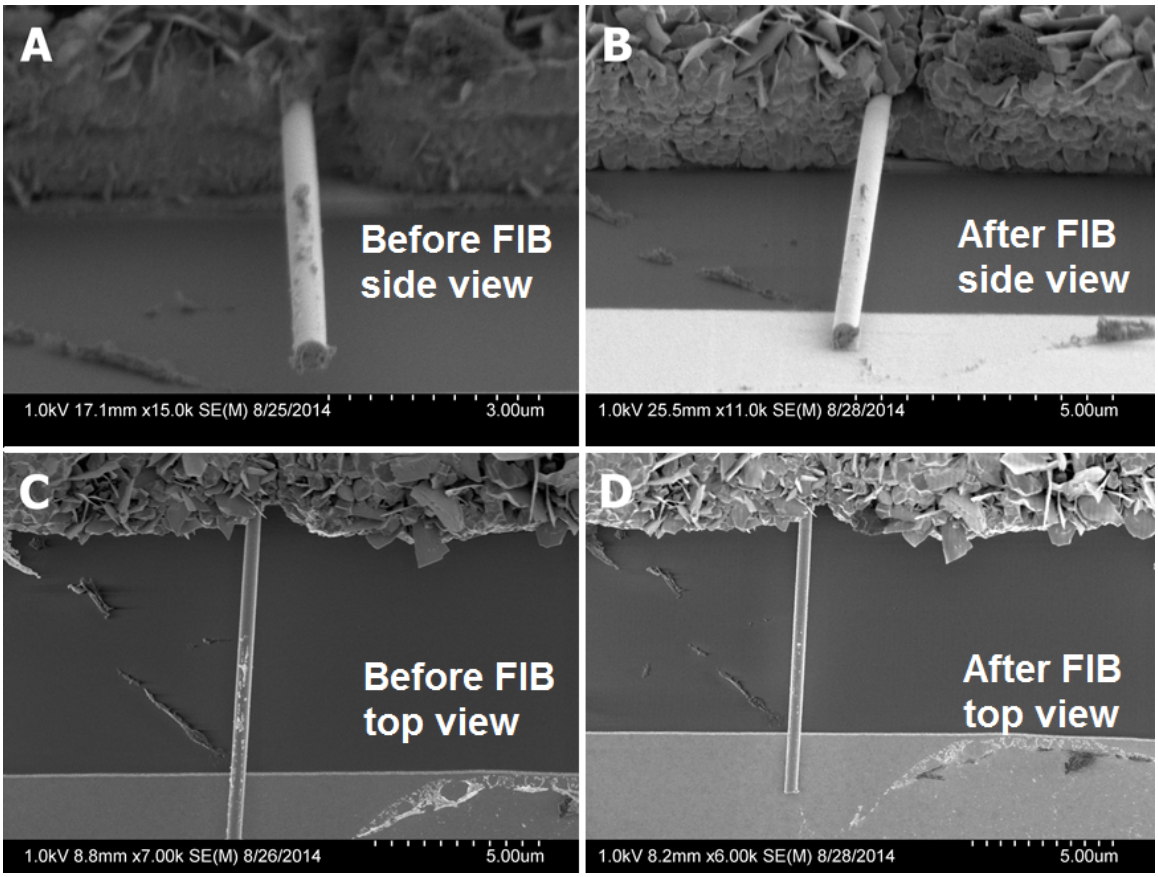

Figure 6.18: FIB failed the NW while trying to clean a small piece of polymer. Ion beam 20-0-30 was used at 15kX magnification for 25 s.

Therefore, use of FIB should be limited to low doses and shorter irradiation times (less than 10 s using 20-0-30 beam) for cleaning purposes. Additionally, several other technical improvement in our microfabrication and polymer dissolving methods have reduced the frequency of such contamination on the NWs and hence, has reduced the need to use FIB for post-clamp cleaning.

6.8 Clamping Conditions in This Work

Several clamp materials and conditions have been investigated in this work. Silver was finally chosen as the clamp material for reasons mentioned in Section 6.4. In general higher temperatures of solution (up to 55°C) and agitation (magnetic-bar stirring) were found helpful in growth of compact, dendrite-free silver electrodeposit. Increasing the electrolyte temperature increases the limiting current density and thus allows

operation with the same electrolyte composition, at higher current density [39]. Electrolyte agitation influences the maximum cathodic current density at which smooth dendrite-free deposition is possible. Agitation of the electrolyte is also important to keep the metal concentration uniform [39].

Both galvanostatic and potentiostatic deposition methods were used. Galvanostatic deposition at current densities ranging 0.3×10^{-2} to 3.3×10^{-2} mA/cm^2 for D1 wafers resulted in reasonably compact and uniform deposition up to 4 μm thickness (roughly equivalent to 4 hours of electrodeposition at given conditions). For the design D2, since the total electroactive area is very small, potentiostatic growth was found to be much more practical. Working potentials of -250 to -300 mV with respect to the Ag/AgCl RE was used typically used for 20 min at temperatures of 40-50°C. This resulted in fine-grained, nodular and compact deposition.

Finally, the distances between the electrodes, had a significant influence on the structure of the silver electrodeposit. In order to fix the electrode distances, a clamp fixture cap was designed and machined to hold all the electrodes and the chip at certain distances from each other repeatedly.

6.9 Conclusions

A probe-station was used for positioning the off-chip synthesized NWs onto a chip device and then the NWs were clamped by deposition of metal into clamp boxes. Two wafer designs were used in this work for making NW resonator devices. The electroactive surface area available for electrochemical clamping for the designs D1 and D2 were 3.1×10^{-1} and 8.0×10^{-1} cm^2, respectively. The importance of considering the effect of clamping in resonance frequency or Young's modulus measurements is that the uncertainty in boundary condition could lead to considerable errors in the measurements. The NW clamps in this work were made by use of electrodeposition from aqueous metal ion solutions. In our method, a full coverage of NW, which holds the resonator firm and approximates the fixed boundary condition was required. The electrodeposited clamps will provide the NW coverage necessary to satisfy the Euler-Bernoulli elastic beam behavior and the rigidity only if the clamp deposit is compact and defect-free.

It was shown that a clamp material should have a combination of high chemical resistance, high elastic modulus as well as low material. Among the three candidates (i.e., gold silver and rhodium) silver was chosen as the main clamp material in this

work due to its much lower price than gold and elastic modulus similar to gold. Main clamp defects, namely, non-compact dendritic structure, out-box growth, coverage asymmetry and cracked clamp were reviewed. By adjusting the electrochemical conditions the nucleation and growth of the electrodeposit can be altered for a defect-free NW coverage. Current densities ranging 0.3×10^{-2} to 3.3×10^{-2} mA/cm^2 for D1 wafers or working potential of about -300 mV vs RE for D2 wafers were found to be suitable electrodepostion conditions at temperatures 40-50°C with solution agitation.

The utility of FIB as a post-clamp cleaning tool was introduced. It was shown that low enough dosage of an ion beam can be used for removing pieces of polymeric residues from the clamped NWs. FIB was also used for isolating short-circuited areas and occasionally, for raising NWs from the dead.

6.10 Future Work

Several interesting questions remain for exploring the electrochemical deposition of the clamp material. The electric field distribution inside the clamp around the NW, can be studied to optimize the clamp window and half-depth well geometry. Also, it would be interesting to experimentally determine the thickness of clamp at which the nucleation and growth process alters at prolonged times. This can contribute towards understanding the reason for formation of the two distinct layers of silver electrodeposit observed in Figure 6.8.

Chapter 7

Nanowire Resonance Measurements

In general, a resonant measurement scheme involves driving the resonator with oscillatory signal that is swept over a suitable frequency range and detecting the resonance spectrum, with the peak resonance frequency defined as the frequency of maximum resonator displacement. The small critical dimension of nanoresonators (e.g., diameter of NW resonator) and the small displacement make the detection of resonance challenging [103]. The following sections discuss the actuation methods, detection method, and other experimental procedures for the resonance measurement.

7.1 Nanowire as a Harmonic Oscillator

A harmonic oscillator has many resonance modes although typical nanoresonators were operated at their fundamental mode in this work. For cantilevered NW resonators, the resonance frequency (f_n) for the n^{th} mode can be obtained from Euler-Bernoulli beam theory [104] as:

$$f_n = \frac{{\beta_n}^2}{8\pi}\sqrt{\frac{E}{\rho}}\frac{D}{L^2} \tag{7.1}$$

where E and ρ are the Young's modulus and the density of NW, D and L are the NW diameter and suspended length, n is the mode number and β_n is the associated eigenvalue. For example, the first four modes have eigenvalues of β_0=1.875, β_1=4.694 and β_2=7.855. The ratio of the resonance frequency for the first two modes

(fundamental mode and the first mode) is ≈6.27

The Q-factor, which is a property-dependent, dimensionless factor, expressed as:

$$Q = 2\pi \frac{mf}{C} \tag{7.2}$$

where C is the damping term, m is the mass and f is the resonance frequency. For $Q \gg 1$, f reduces f_0. Under this condition, Q can be rewritten as:

$$Q = \frac{f_0}{\Delta f} \tag{7.3}$$

where Δf is the full width at half-power maximum of the resonance spectrum. This expression enables the determination of the Q-factor from measured resonance spectra. However, if the damping is significant (Q is comparable to 1), f will be significantly different from the natural frequency f_0.

Q-factor is the most relevant quantity for fluid-nanoresonator interaction studies. High fluid damping reduces the Q-factor and can also reduce the accuracy of frequency peak locating (flattened, rather than sharp peak) and decrease the signal-to-noise ratio. However, at high vacuum, the accuracy of frequency peak location is very unlikely to change [7]. High Q-factor or low damping, allows for the amplitude of resonance to decay slowly.

Q-factor is largely used to characterize dissipation within the NW material (can be related to grain structure and the density of grain boundaries [4]) as well as measuring the damping due to fluid-nanoresonator interaction [7].

7.2 Resonance Frequency Detection Setup

A considerable obstacle in developing NW resonator-based technologies is the realization of robust methods to detect the displacement amplitude of the resonators. In this thesis, a laser interferometry technique similar to the one used by Li [103] was used to detect the resonance of cantilevered NW resonators.

Figure 7.1 shows the schematic of the measurement setup used in this work to measure the resonance of cantilevered NW resonators at high vacuum. The main components in this setup included the resonator actuation system that uses either a piezo disk to drive the entire chip or electrostatic actuation to drive each NW resonator independently; the laser system for the optical detection of the displacement of NW resonators; the vacuum system that enabled the resonators to be operated at

high vacuum ($<10^{-8}$ torr) and the signal detection system consisting of an AC-coupled photodetector and a spectrum analyzer.

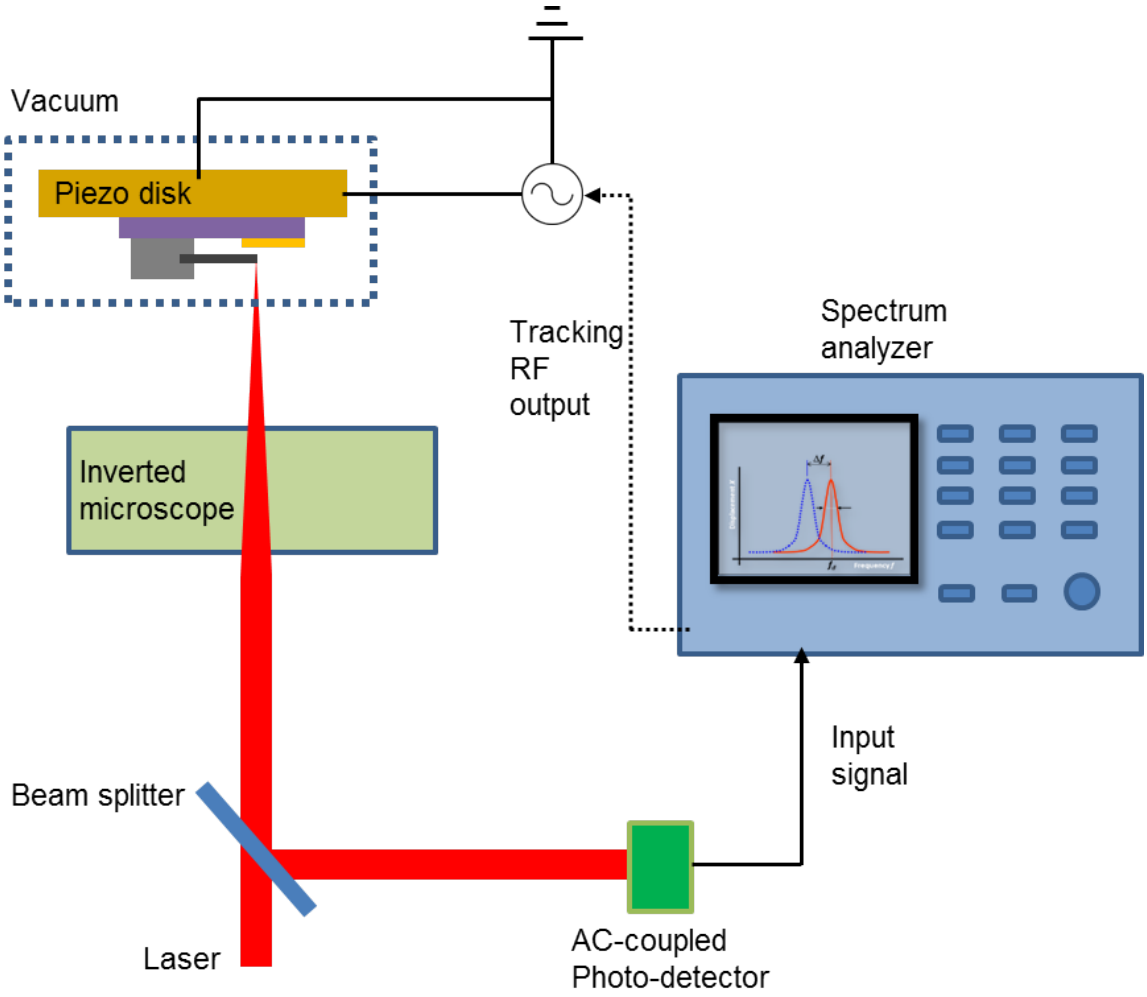

Figure 7.1: Schematic of the measurement setup (showing piezo-driven operation) used in this work to measure the resonance of NW resonators.

Piezo disk actuation was used for the majority of the resonators characterized in this thesis. As an alternative method, electrostatic actuation yields cleaner resonant spectra and newer chips have been designed to enable this. Figure 7.2 shows the laser interferometry setup used for resonance frequency shift detection.

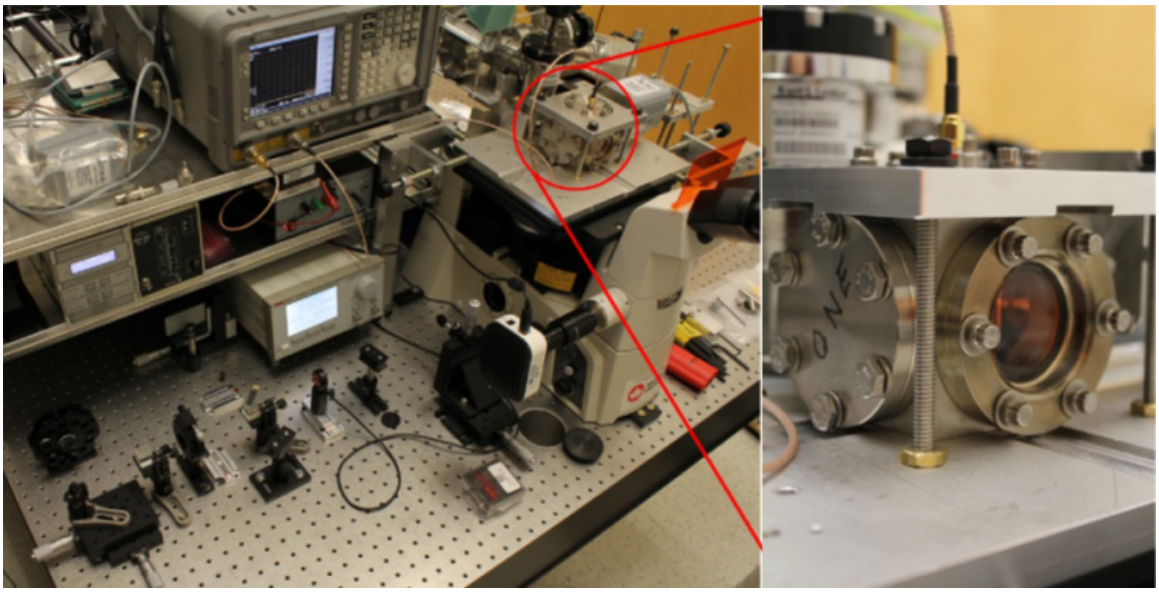

Figure 7.2: Laser interferometry setup used for resonance frequency shift detection. A magnified image of the vacuum chamber is shown on the right.

To conduct resonance measurements, the NW resonator chip was mounted on a piezo disk and placed into the high vacuum chamber with the chip facing downward after the NW resonator fabrication (discussed in Chapter 6). The vacuum chamber was secured on an inverted optical microscope that was used to focus a laser onto the free end of the cantilevered NW resonator through a 40X objective. The light reflected off the NW surface and chip substrate generated the interference signal and was guided back through the microscope objective. A beam splitter was used to direct the reflected light to an AC-coupled photodetector, which filtered the DC background from the AC signal. An RF spectrum analyzer with a tracking generator output was used to supply the driving AC voltage and to measure the signal from the photodetector. The amplitude of the interference signal varied with displacement amplitude –the frequency corresponding to the peak amplitude is the damped resonance frequency. The pressure of the measurement chamber was controlled by a turbo-molecular pump placed in series with a dry backing pump, which allowed the chamber pressure to be controlled from 10^{-8} torr to 1 atmosphere by pumping out or feeding in pure (10 ppm impurities), dry nitrogen.

7.3 NW Resonance Actuation

The two actuation methods for driving the NW resonators, used in this work, piezo disk and electrostatic, are briefly described below.

7.3.1 Piezo Disk Actuation

In this actuation method, a commercially available piezo disk that was driven by an AC voltage was used to induce oscillations of the resonators. Many research groups have successfully used this actuation method to characterize NEMS resonators. In this work, piezo disks were extracted from Radio Shack buzzers to drive the NW resonators with resonance frequencies ranging from 1 MHz to 10 MHz. The piezo disk contained three layers: a brass substrate, a piezoelectric film, and an aluminium contact. This piezo disk and a mounted NW chip are shown in Figure 7.3.

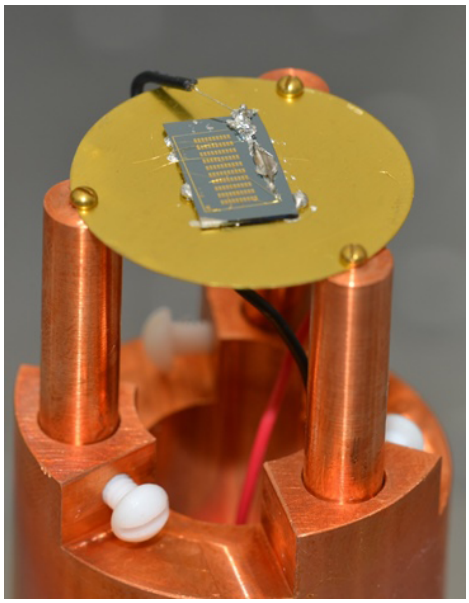

Figure 7.3: A chip is mounted on the brass disk, which is assembled on a vacuum flange (not shown) using metal screws and copper pillars. Two electric feedthroughs on the flange can be used to apply the AC voltage; one was used for the piezo disk actuation and the other for electrostatic actuation.

During the measurement, the AC voltage induced the vibration of the piezo disk, which drove all of the resonators on the chip. The AC voltage was swept over a range of frequencies that was centered around the resonance frequency of the NW resonator

being measured.

The frequency response of the piezo disk can affect the measurement and evaluation of the resonator performance. The impedance of the piezo disk varies significantly within the frequency span and can generate a non-uniform driving force on the NW resonators during the measurement particularly when large frequency spans are involved. This makes it difficult to quantify the force applied to the resonator and to analyze the resonance performance of very low quality factor resonators.

7.3.2 Electrostatic Actuation

In electrostatic actuation, an AC voltage, is applied between the resonator and a counter electrode. Due to the capacitive coupling, the voltage produces an electric field between the resonator and the electrode. This induces charge on the resonator, which in turn will generate an electrostatic force to drive the resonators [103].

In this research work, rhodium NW resonators were electrostatically actuated by applying an AC voltage between the pairs of interdigitated electrodes that were used for NW resonator assembly and integration (results not included in this dissertation). The chip containing the NW resonators was mounted on the piezo disk as described in the previous section to allow actuation by the two methods.

The lead wire bonded to the clamping electrode was connected to the electrical feedthrough on the flange to provide the AC voltage for driving the resonance. The other bonded lead wire was connected to the brass substrate, which was connected to the Cu pillars that served as the ground (See Figure 7.3).

7.4 Nanowire Resonance Measurement Procedure

The resonance measurement procedures mainly include mounting the chip on the piezo disk, loading the piezo disk into the chamber, evacuating the chamber to desired vacuum level, laser alignment to individual resonator, and resonance spectrum collection.

After the NW resonator integration, the chip containing the NW resonators was mounted on the brass substrate of a piezo disk (shown in Figure 7.3) using indium metal in place of fluxed solder, to secure the chip to its mounting surface. Indium was chosen because it has a low vapor pressure and a low melting point (T_m=156°C), and the solid is soft enough to cut small volumes with a blade.

A 10 mW laser (wavelength=633 nm), providing approximately 3 mW input power for measurement, was focused on the free end of the NW resonator on the chip, through the inverted microscope. The light reflected off the NW surface and chip substrate generated the interference signal and was guided back through the same microscope objective. A beam splitter was used to direct the reflected light to an AC-coupled photodetector, which filtered the DC background from the AC signal. The filtered-off background included the interference between the light reflected back from the two sides of the glass view port on the vacuum chamber and from various component faces in the optical path. An RF spectrum analyzer (Agilent E4402B) with a tracking generator output was used to supply the AC voltage and to measure the signal from the photodetector. The amplitude of the interference signal varied with the displacement amplitude and had a maximum value at the NW's resonance frequency.

7.5 Nanowire Resonance Characterization Results and Discussion

Resonance spectra from four RhNW resonators in high vacuum ($<10^{-7}$ torr) were collected using a piezo disk driving method and are shown in Figure 7.4. For comparison, the resonance amplitude (y axis) of each spectrum is normalized to its own peak amplitude. Table 7.1 lists the size and resonance characteristics of four Rh NW resonators.

Table 7.1: Size and resonance specifications of the four measured RhNWs made from SOL10 inside PC400ST2525 template at -400 mV vs Ag/AgCl RE. The NWs with silver at 3.3×10^{-2} mA/cm^2 current density (D1 design).

NW	D (nm)	L (μm)	f (MHz)	Peak amplitude (μV)
I	430	13.6	1.458	63
II	454	11.3	2.315	20
III	450	9.9	2.966	13
IV	441	9.3	3.224	16

All the four NWs were electrodeposited from SOL10 inside PC400ST2525 polycarbonate template at -400 mV with respect to the Ag/AgCl RE. The NWs were

clamped using a silver Cy-less solution (SOL5) at 3.3×10^{-2} mA/cm^2 current density. Figure 7.4 shows the corresponding piezo-driven resonance spectra of NWs I-IV.

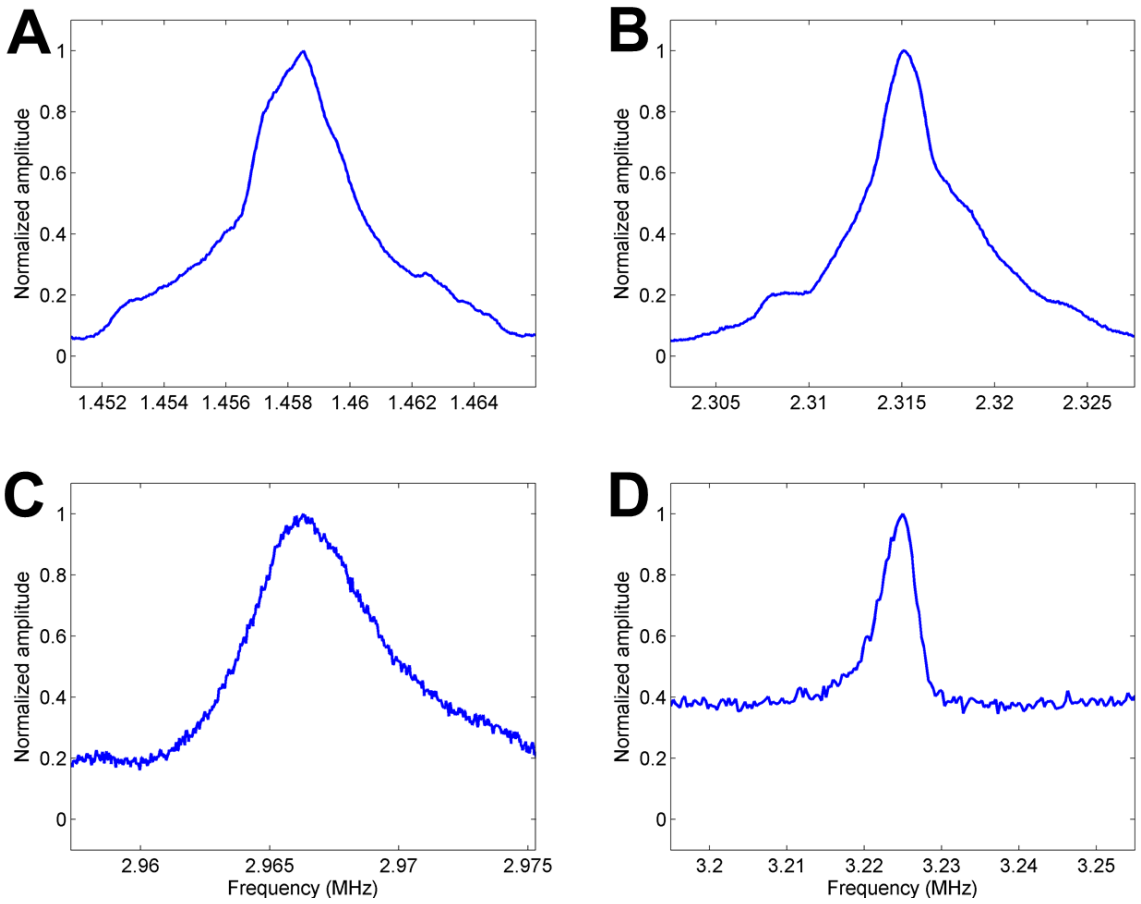

Figure 7.4: Resonance spectra in high vacuum. RhNW resonators were driven by piezo disk actuation method. All spectra were normalized to their own peak amplitude. Spectra A to D correspond to NWs I to IV, respectively.

The signal-to-noise ratio of Figures 7.4A and B are higher than those of Figures C and D. The piezo disk actuation typically results in noisy spectra. The spectra signal-to-noise ratio at lower frequencies for NW1 and NWII is higher than NWIII and NWIV driven at higher frequencies. Although piezo driven results are noisy compared to electrostatic actuation and not suitable for determining the Q-factors, it is very unlikely that the location of peak frequency changes in the spectra. Therefore, the results in Figure 7.4 were used for determining the elastic behavior of these NWs. Figure 7.5 shows a plot of resonance frequencies against D/L^2.

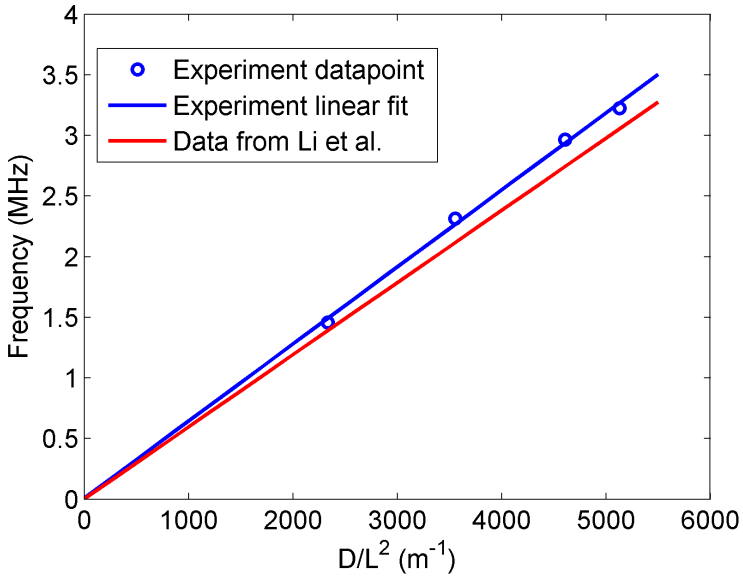

Figure 7.5: Piezo driven resonance frequency of RhNWs I-IV vs their geometry factor D/L^2. The red line shows the data from [4] for comparison.

Using Eq. 7.1 with rhodium density 12.41 g/cm^3 and assuming a rigid clamp (β_0=1.88), the elastic modulus of the RhNWs I-IV were calculated to be 254 GPa, 67% of 379 GPa quoted for bulk polycrystalline rhodium [54]. This result already shows 14% improvement compared to the 222 GPa from RhNWs made galvanostatically at current density of 1.2 mA/cm^2 (red line, from [4]). There is very little known about mechanical properties of free-standing nanoscale objects such as NWs due to difficulties associated with standard tensile or bending tests [5]. However, it might be possible to increase the elastic modulus of rhodium NWs closer to 379 GPa quoted for bulk polycrystalline rhodium. In this work, rhodium NWs with different grain size and structure have been made, which are currently being assembled on resonance chips by Mahshid Sam for measurements. For instance, rhodium NWs made by use of PEI as an additive (SOL9) or EDTA (SOL7) have shown grain sizes down to 5 nm under TEM. These results suggest that different intrinsic dissipation and elastic modulus might be expected from these NWs. By development of the structural studies, new requirements for grain structure of NWs can be established for making NWs with the highest elastic modulus possible from any given material. The measurement of the shift in the peak resonance frequency of NWs has been used to demonstrate [8] specific response to the mass of a few molecules of PCA3, an RNA biomarker for prostate cancer. It has also been used for drag force measurements on NWs in the transitional

and free molecular flow regimes of rarefied gas dynamics [3, 105]. These measurements are important for developing theory [106] and for practical matters such as the effect of gas damping on various sensors [7]. Thus, improvement of mechanical properties of electrodeposited NWs can directly serve many active research areas, as well as sensor devices.

7.6 Conclusions

The resonance frequency measurement results of four rhodium NWs at high vacuum, compared to previous studies, exemplified how the mechanical properties such as elastic modulus, can be altered for nanoresonators made from a given material, only by control over electrochemical deposition conditions (in this case, potentiostatic deposition at a higher overpotential). These in turn can stimulate work on new requirements for grain size and crystal structure control. The results would also be used as a baseline for improving the mechanical properties of other materials used in nanoelectromechanical systems.

7.7 Future Work

The photolithographic patterning and microfabrication of resonator chips were carried out at the Simon Fraser University, as the required tools and clean room facility were not available at UVic. Restrictions in the avalability of equipments, costly trips and user charges, and many other practical limitations slowed down the development and production of our NW test chips.

However, for a systematic study of the electrochemical conditions (mainly: overpotential, ionic concentration, temperature and additives in SOL6-10) and their relationship to the structure and properties of the nanoresonator, several batches of high-quality NWs have been produced and are readily available for chip assembly and resonance test. A number of these batches of NWs are currently being assembled on resonator chips by Mahshid Sam. The results would be used shortly for better understanding of the connection between the grain structure and material elastic modulus and intrinsic dissipation (by electrostatic drive) of NWs.

An equipped microfabrication facility is expected to become available at UVic in a time scale of one year. This will significantly boost the chip production rate for resonance measurements and make use of NWs synthesized in this PhD work.

Additionally, the new STEHM microscope with the highest TEM resolution, has very recently become available to the UVic users. Availability of the new, high-resolution, aberration-corrected TEM will be an important advantage for the structural studies required for continuing this work in the future.

Chapter 8

Conclusions

This dissertation presents the first research work that targets the material properties induced by the synthesis conditions of nanoresonators and their relation to resonance frequency. In this study, synthesis of cylindrical, straight and separable NWs in particular was explored for use in resonator devices. Several parameters that can significantly influence the electrochemical nucleation and growth of the resonator and clamp material were used to engineer the mechanical characteristics of the electrodeposit.

In previous work on the bottom-up assembly of off-chip synthesized nanoresonators, the role of materials synthesis conditions on the performance of resonator systems had not been studied. Therefore, the most important distinction of this PhD work is showing how the material properties, structure, and the synthesis conditions of nanoresonators can be tuned to alter the performance of resonator devices. As a result of this work, many other research directions were identified for future improvement of resonators. Several defects, shortcomings were diagnosed, categorized and discussed for the first time in this work. For many of them, possible reasons and remedies were suggested.

In particular two important concerns related to the synthesis of gold and rhodium NWs for use as resonator were addressed in the form of published papers: producing straight separable gold NWs from a non-cyanide solution and making rhodium NWs with the possibility of controlling the grain structure.

In addition, the structure of five different commercially-made anodized aluminium oxide and track-etched polycarbonate membranes were examined for use as template for electrochemical synthesis of NW resonators or NWs electrodes in photovoltaic systems. The important role of template preparation method on obtaining a clean

batch of functional NWs was introduced for the first time for various templates.

The nucleation and growth of silver, gold and rhodium from various solutions and under a range of electrochemical conditions were studied to find suitable working conditions for making NW resonators. The structure of the electrodeposit in this work were mainly studied by use of SEM at low acceleration voltages. Effect of complexing agents and various chemistries of the solution for gold NW deposition were investigated by use of SEM characterization. A tube-to-rod growth pattern was observed for early stages of NW electrodeposition. It was shown that metal nanotubes are formed initially and merge into nanorods before reaching 1 μm length.

In this work, silver was proposed and used as clamp material, alternative to previously used gold clamps made from cyanide. Silver with its price about 1/70 of gold and elastic modulus close to gold, was shown to be a suitable replacement to gold clamps made from cyanide-based solutions. Our resonance measurements of the rhodium NWs clamped with silver, proved that the elastic modulus of rhodium NWs can be improved by changing the electrochemical conditions. Rhodium NWs made and clamped with silver in this work from a sulfate solution at -400 mV vs Ag/AgCl show 14% increase in elastic modulus compared to galvanostatically grown rhodium NWs in other studies. This increase in NW elastic modulus has been achieved from a solution without additives. Therefore, by continuing the resonance measurement on NWs made from different solutions with additives, new results can be expected.

This research work has introduced a new view of the interdisciplinary research field of nanoresonators and perhaps other related fields, by relating the synthesis conditions and materials properties to mechanical performance of nanoresonator devices. It has shown that choosing the material element itself does not entirely determine the properties of a nanoresonator. The electrochemical conditions of the synthesis can have a considerable influence on the mechanical properties and the performance of the nanoresonator. This also gives the metal NWs a better chance to extend the NEMs application.

Appendix A

Electrochemical Cell

A second electrochemical cell was designed and machined to be used for a smaller size of PC templates i.e. 13 mm in diameter. These particular templates are of interest because of their small pore diameter (nominal 10 nm is the smallest size produced by the manufacturer). Using these templates, NWs with actual diameter of ∼40 nm can be made. However, the maximum nominal length of these NWs is 7 μm, which is a limiting factor for application as nanoresonator.

The main reason for this particular cell design was to provide a platform for synthesizing NWs directly attached to any conductive substrate (without an evaporated contact layer). For this cell, the conductive substrate should be long enough so that the electrical contact can be made to the potentiostat cable. The substrate should also be flat at microscopic scale. It should also be rigid enough not to crack under screws tension. The initial design was modified and finalized (see Figures A.1 and A.2) by a mechanical engineering undergraduate co-op student Spencer Davis.

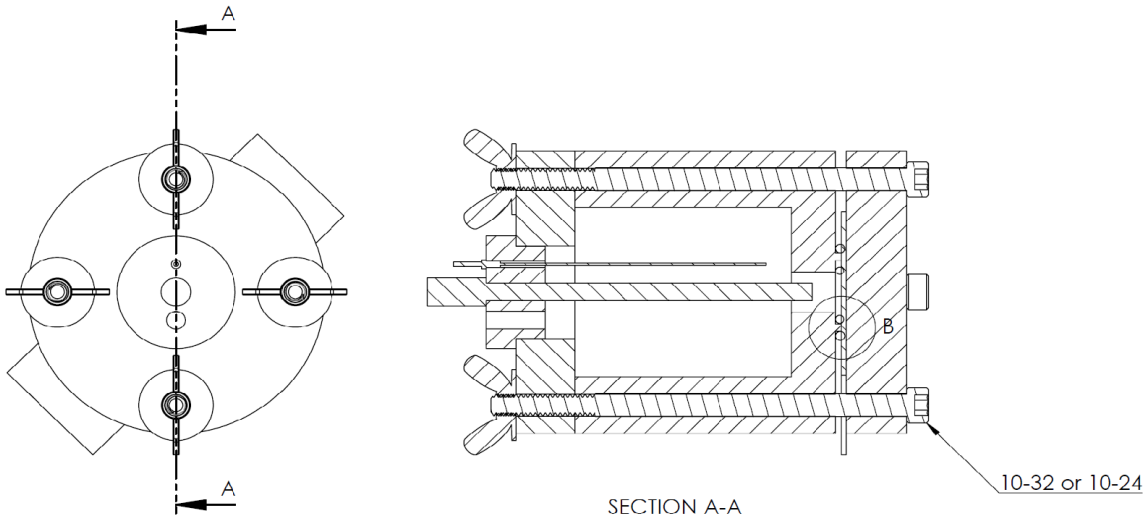

Figure A.1: Design used for machining the second electrochemical cell.

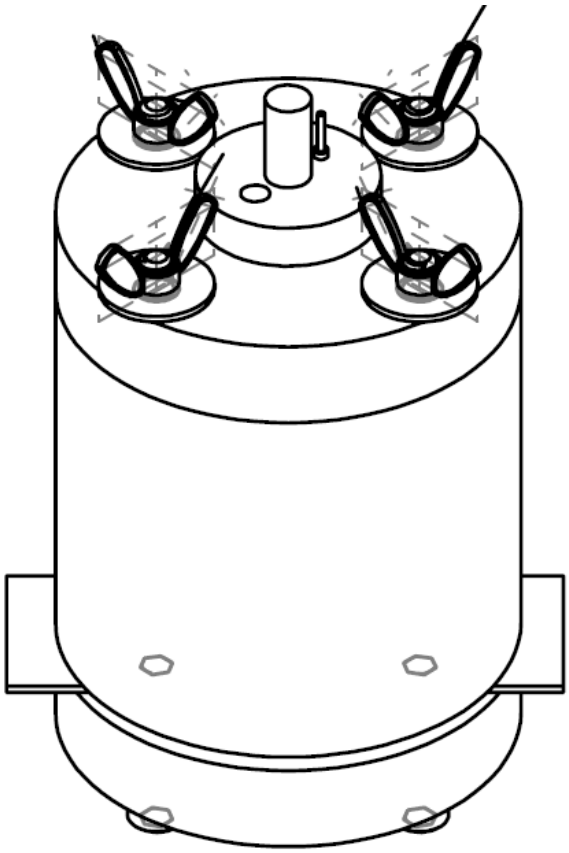

Figure A.2: 3D view of the second electrochemical cell.

Figure A.3 shows the assembly steps of the cell.

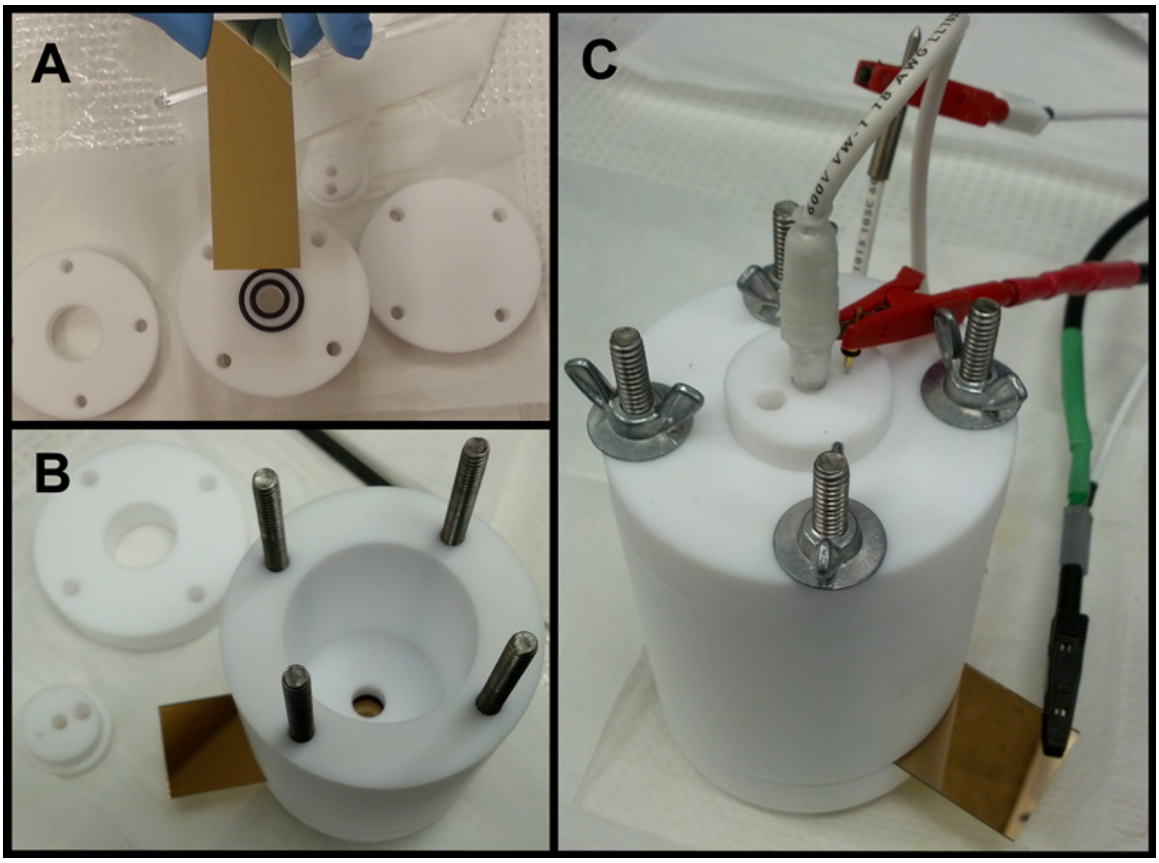

Figure A.3: Assembly of the second electrochemical cell.

Appendix B

Templates

This Appendix provides information on the commercial membranes that were purchased for NW growth. The list of membrane size and features are given in Table 2.3.

Figures B.1, B.2 and B.3 show snapshots of all the membrane boxes that were used in this work. The information on the boxes can be used for placing purchasing order.

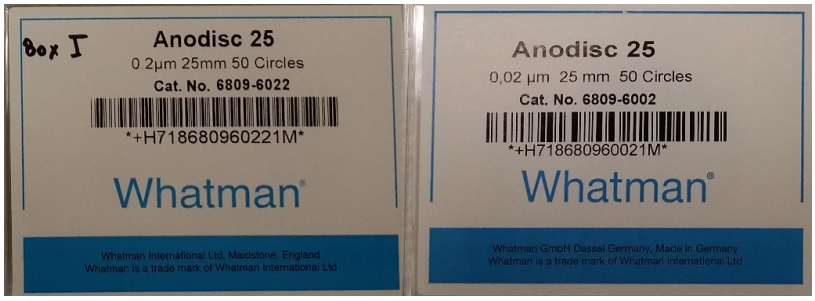

Figure B.1: Anodized Aluminium Oxide membranes purchased from Whatman for this study.

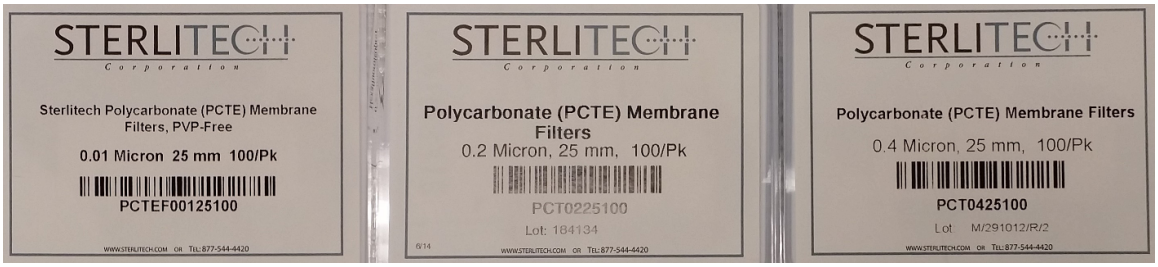

Figure B.2: Polycarbonate membranes purchased from Sterlitech for this study.

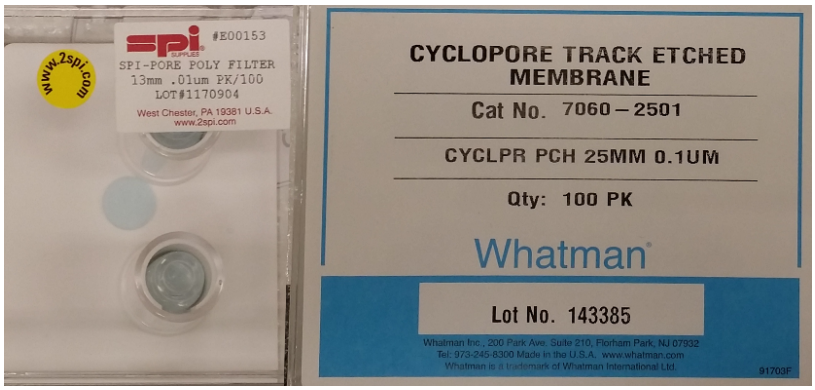

Figure B.3: Other polycarbonate membranes purchased from SPI (left) and Whatman (right) for this study.

Figure B.4 shows an image of AO200WT6025 templates after coated on one side with silver as an electrical contact layer. The aluminium oxide membranes before silver evaporation have white color. After contact layer evaporation, the silver side becomes bright and the other side will be seen dark due to a light scattering effect.

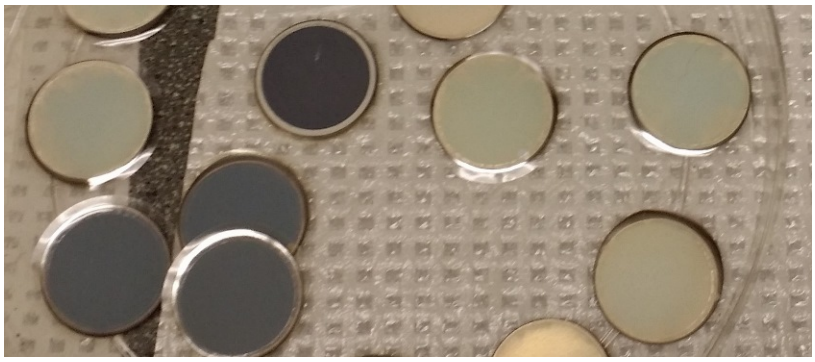

Figure B.4: Aluminium oxide membranes (AO200WT6025) photographed after coated with silver. Silver coated side is the bright side.

Figure B.5 shows three sets of polycarbonate templates that are coated silver on one side and can be used for NW electrodeposition.

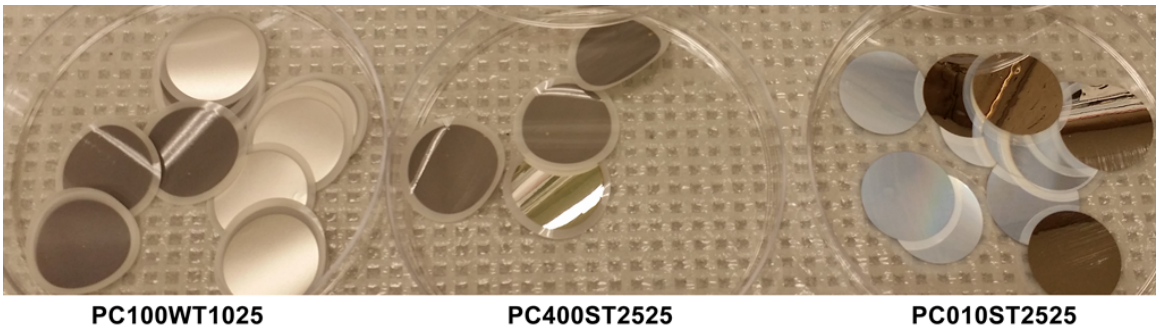

Figure B.5: Three sets of polycarbonate membranes photographed after being coated with silver.

As mentioned in section 2.6.2 (Figure 2.8(B)) the two sides of polycarbonate membranes are not identical. Mirror-like light reflection from five membranes (that were placed upside-down) compared to the matte reflections from the other membranes inside the holder, suggested the two sides of the polycarbonate membranes have distinct surface properties. The difference is related to the fabrication process (as also confirmed by the manufacturer) which creates a rough surface on one side of the membranes as shown in Figure B.6.

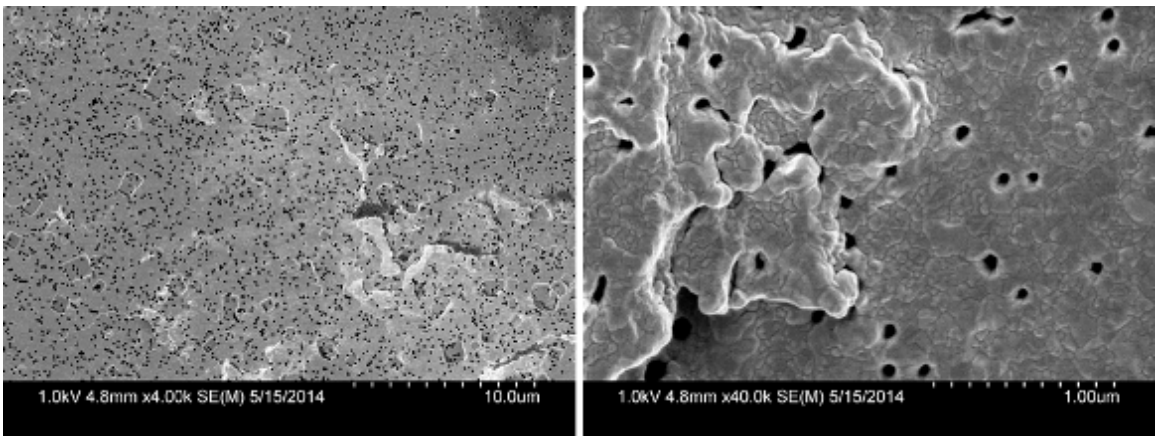

Figure B.6: A low and a high magnification SEM image of the rough surface side of the polycarbonate membrane.

Also the two sides of anodized aluminium oxide membranes are not identical.

Figure B.7 shows the difference in the surface colors of the silver-coated templates marked by arrows and the other coated membranes. shown by arrows.

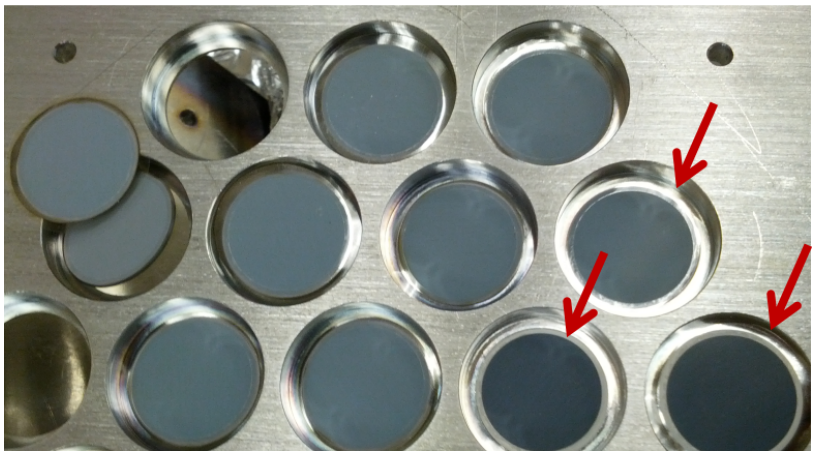

Figure B.7: The anodized aluminium oxide membranes coated on two different sides show two different colors. Those marked with red arrows have a distinct darker color compared to the others.

In the case of anodized aluminium oxide, the difference in light scattering is most probably related to the existance of the branched region on one side of the template (discussed in section 2.5.2).

Appendix C

Dissolving Template Material and Nanowire Extraction

In order to obtain single NWs for assembly on a resonator device, the NWs must detached from the silver layer and be extracted from the membrane inside which they have grown. After termination of the electrochemical deposition of NWs, the evaporated silver contact layer, as well as any sacrificial silver elctrodeposit will be removed by rinsing three times with 34% nitric acid.

In our experiments, the templates containing NWs were placed on a Petri dish for silver dissolution. At each rinse, a few droplets ($\sim$ 5 ml) of nitric acid is dropped by a pipette on the silver-coated side of the template. The templates were slowly shook for 30 seconds and then the acidic liquid was removed with a pipette. The templates were rinsed with DI water between every two acid rinses. After final rinsing with DI water, the templates are ready for membrane dissolution. For each membrane material a separate dissolution process must be taken as discussed in the following two sections.

C.1 Dissolving Aluminium Oxide Membranes

After silver dissolution with nitric acid, the aluminium oxide membranes were snapped apart into two or three pieces and placed in centrifuge tubes. The centrifuge tubes were then filled with a 3 M solution of sodium hydroxide or potassium hydroxide and centrifuged to extract NWs from the resulting solution. The supernatant was then removed using a micropipette. Distilled water was added for dilution and the process

repeated three times. After final step of centrifugation and supernatant removal, ethanol was added for storage of NWs.

C.2 Dissolving Polycarbonate Membranes

The standard solvent for polycarbonate dissolution is dichloromethane (also known as methylene chloride) with the chemical formula CH_2Cl_2. Other solvents such as acetone, ammonia, brake fluid and drilling oil have been suggested for removing polycarbonate membranes (online chemical forum discussions). However, my attempts with acetone by immersing PC template in a beaker full of the liquid for more than one week did not result in dissolving any observable amount of polycarbonate.

Although dichloromethane[1] is a polar molecule, its lack of ability to make hydrogen bonds makes dichloromethane almost insoluble in water. My experiments also confirmed that water and dichloromethane tend to separate in a test tube. For rinsing purposes, ethanol should be used instead of water (unlike aluminium oxide templates).

For dissolving a polycarbonate template after electrodeposition, the membrane can be put inside a test tube. Prior to dichloromethane, nitric acid (34%) should be added to test tube for silver dissolution. Similar to the procedure for aluminium oxide templates, the polycarbonate membrane should be rinsed with DI water three times in order to remove acid residues. Prior to the addition of dichloromethane to test tube, all the remaining water should be extracted by pipetting and the test tube should be left open for an hour for complete drying. For a faster drying, a stream of nitrogen or dry air can assist.

In case dichloromethane is added without completing the water-drying stage, a droplet of water will remain on top of the dichloromethane in the test tube (the density of dichloromethane is 1.33 g/cm^3) until the end of nanowire extraction that would make the entire pipetting precess more difficult.

Once the template is fully dried, dichloromethane can be added using a pipette. At this stage, upon the addition of dichloromethane, the template would no longer be observable as a separate entity in the tube. The nanowires will disperse entirely in the solvent. To separate the nanowires from the solvent, a centrifuge equipment

[1]Dichloromethane is a carcinogen and should not be used unless under a working fume hood, with appropriate precautions taken and all safety protections worn. One should never work with dichloromethane without having read the MSDS thoroughly.

should be used similar to aluminium oxide template dissolution and wire extraction procedure.

At least three rinses with extra dichloromethane, shaking and pipetting followed by three times rinsing with ethanol is required for clean nanowire extraction procedure. Some articles have mentioned a protocol for cleaner rinse which includes: two times rinsing polycarbonate in dichloromethane at 40°C followed by rinsing in chloroform (CH_3Cl) and later ethanol. Use of a plasma cleaner at 100°C has also been recommended.

We have also used commercial photoresist remover known as Shipley 1165 for dissolving polycarbonate membranes. This is a mixture of a few organic solvents specifically formulated to remove all Shipley photoresists.

C.3 Nanowire Contamination from Dissolution Process

A clean dissolution of membrane is more challenging in the case of polycarbonate compared to aluminium oxide. SEM analysis of more than 40 times attempts to dissolve polycarbonate membranes after NW growth, has shown that the contamination sources can be classified into three major types. Figure C.1 shows three main types of contaminations identified in the NW extraction process.

Figure C.1A shows spot granular contamination typically attached to NW surface. Figure C.1A shows a contamination type that precipitates on the substrate rather than the NW surface. This type is most probably coming from the polymeric test tube. Figure C.1C shows large pieces of polymeric contamination that usually appear when the polycarbonate dissolution process is not complete.

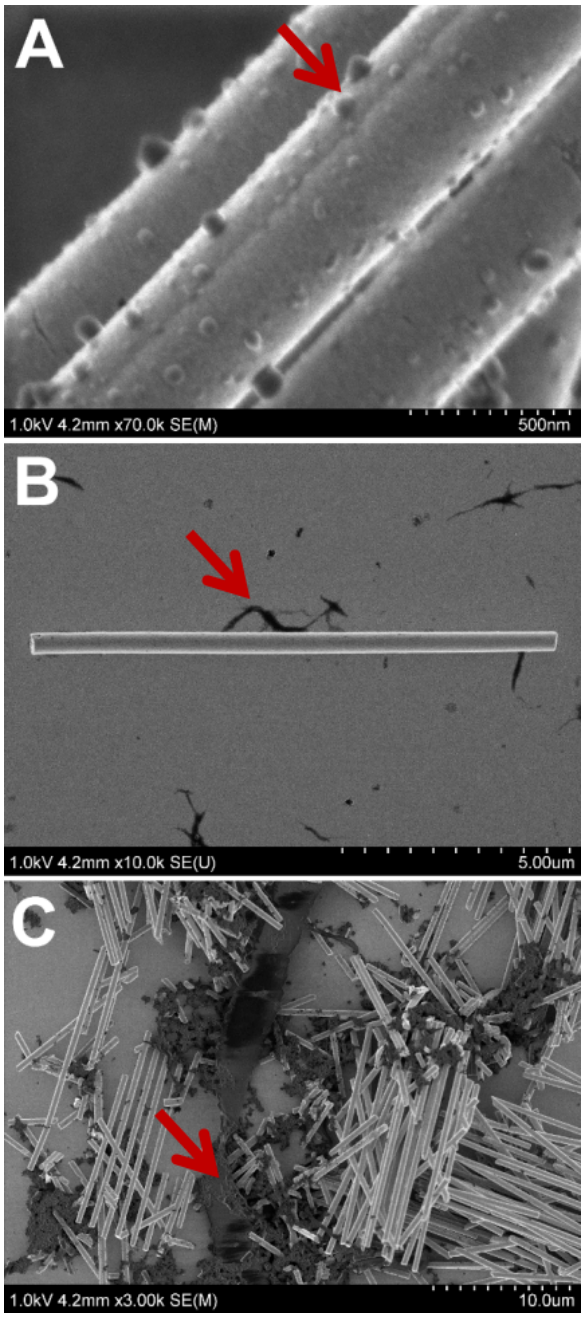

Figure C.1: Three main types of contaminations identified: (A) spot contamination on NW surface, (B) off-NW dark string contamination, and (C) Large dark chunks of polymer usually found between the NWs.

It should be noted that prolonged exposure of regular test tubes to dichloromethane will result in the dissolution of the test tube material. Dissolution product will be clearly observable after 24 hours. The lid of test tube becomes thin and fragile. (It

also dissolves nitrile gloves!) in order to avoid contamination from the test tube into the NW batch, the test tubes were replaced by glass vials. Figure C.2 shows regular test tubes, as-received glass vials and machine-cut glass vials that were shortened to fit into the centrifuge tubes or adaptors.

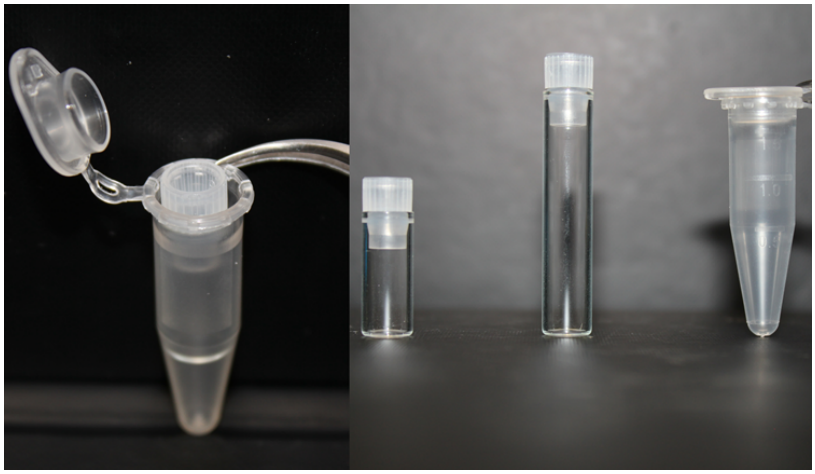

Figure C.2: From right to left: regular test tube, as-received glass vials and machine-cut glass vials that can fit into centrifuge tubes after cut.

Using glass vials the solvent could be left for longer times in the vial to dissolve the membrane with no concern about losing the nanowire batch. Figure C.3 shows a clean batch of NWs obtained by dissolving the polycarbonate template with a Shipley 1165 solvent that often works cleaner than dichloromethane.

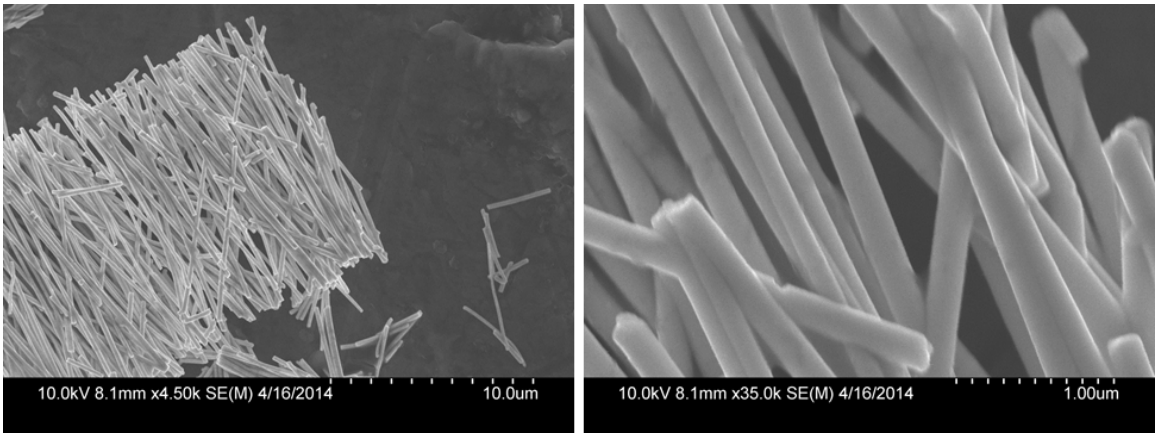

Figure C.3: A clean polycarbonate membrane dissolution.

Appendix D

FIB for TEM Specimen Preparation

FIB was used in several trial runs to check the feasibility of using FIB as a cutting tool to prepare thin specimens for electron diffraction studies under TEM. Ideally, thin slices –less than 100 nm– should be cut out of NWs in longitudinal and cross-sectional directions to check the texture, grain orientation, grain size distribution and other crystal features of the NWs. However, the cutting process can also cause sputtering of the atoms and reconstruction of the cut-surface producing artefacts.

The local heating due to intense ion-beam interaction with a tiny region of the NWs can activate recrystallization of the metallic NW. In this case, the crystal characteristics inherent to the electrodeposition synthesis will be lost and can be a serious source of error in the interpretation of the results.

FIB was initially used on rhodium NWs (dispersed on an Au-evaporated glass slide) to find the proper working conditions. The specimen used was 14Rh1027-pc400nm with NW diameters of about 450 nm.

The reference ion beam 40-1-30[1] was tested as a cutting (fabrication mode) beam only. The viewing beam was a low intensity 10-0-30 beam, which caused a minimal damage to the NWs but did not give a high viewing resolution.

The dwell time for all the cuts was 0.5 μs (the minimum time available for this device). For most cuts, the magnification was set to 15000X and the zoom was 4X giving a total magnification of 60000X. For fabrication with the 40-1-30 beam, the

[1]The ion beams of Hitachi FB-2100 FIB are tabulated by a format of *xx-y-zz*, where *xx* is the acceleration voltage in kV, *y* is either one or zero depending on the condenser lens being on or off, and *zz* is the aperture size in μm.

number of rasters was N=200.

The other beam used was 30-0-30, which worked reasonably well for side-cutting. For cross-sectional cuts, this beam was used with N=800 twice (total 1600) because going 1600 time at once caused the NW to melt locally and deform. Also a box of 1 μm by 0.5 μm was tried with the beam 30-0-30 to make the NW thinner.

After live monitoring of the cutting process under various beam conditions, it seems that FIB is a highly destructive cutting tool for NWs. Local heating at cutting regions is very likely to reconstruct the crystal structure of NWs, making the TEM observation unreliable.

The ionic current values in Tables D.1 and D.2 were provided by the Advanced Microscopy Facility of the University of Victoria[2].

Table D.1: Ion beam current in nA when condenser lens is off, based on the ion acceleration voltage and the diameter of objective aperture of Hitachi FB-2100 FIB.

$_{kV}\backslash^{Aperture(\mu m)}$	5	15	30	80
10	0.00010	0.00027	0.00133	NA
15	NA	NA	NA	NA
20	NA	NA	0.00305	NA
25	NA	NA	NA	NA
30	NA	0.00143	0.00674	0.03946
35	NA	NA	NA	NA
40	0.00130	0.00335	0.01583	0.09280

Table D.2: Ion beam current in nA when condenser lens is on, based on the ion acceleration voltage and the diameter of objective aperture of Hitachi FB-2100 FIB.

$_{kV}\backslash^{Aperture(\mu m)}$	5	15	30	80	150
10	NA	NA	NA	NA	NA
15	NA	NA	NA	NA	NA
20	NA	0.00588	NA	0.26861	NA
25	NA	NA	NA	NA	NA
30	NA	0.00882	0.05195	0.44652	2.1265
35	NA	NA	NA	NA	NA
40	0.00303	0.01064	0.06540	0.64103	3.0318

[2]Data available at: http://www.stehm.uvic.ca/facility/instruments/.

Appendix E

Electrospun Gold Microparticles

An electrospinning setup in the Jun Lab was used for making gold particles. The intent was to carry out feasibility of using the setup for making gold fibres or coating polymers with gold for protein attachment. The details of the electrospinning setup can be found in the PhD Dissertation of Junghyuk Ko from Martin Jun's group.

A gold chloride solution (SOL4) was ejected from a nozzle towards an aluminium foil electrode, which was at a potential of -5 kV with respect to the nozzle. The foil was wetted with ethanol to provide a reducing ambient. Figure E.1 shows formation of gold particles with diameter ranging 0.3–3 μm, on the ethanol-wetted areas of the foil.

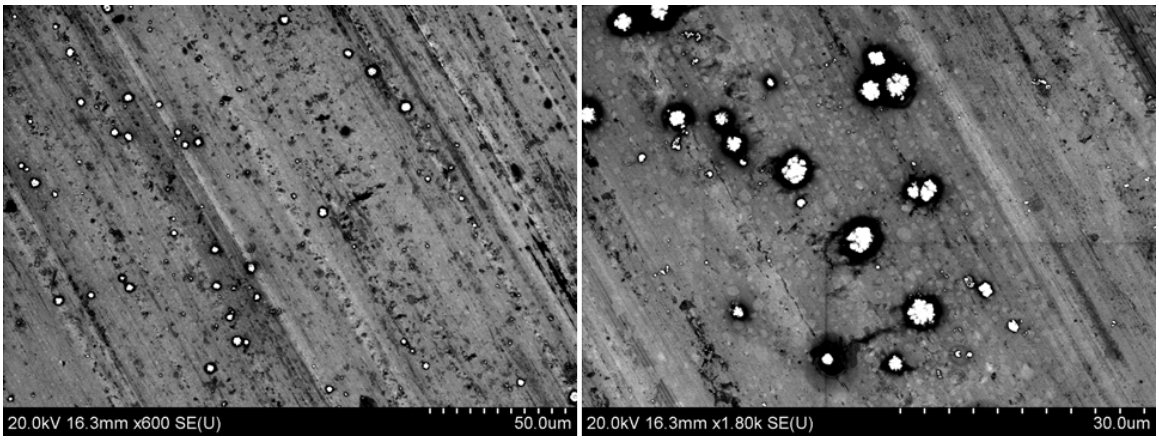

Figure E.1: Micon size gold particles made by use of an electrospinning device and collection on an ethanol-wetted aluminium foil.

The chemical analysis of the particles with EDX confirmed the presence of gold as shown in Figure E.2.

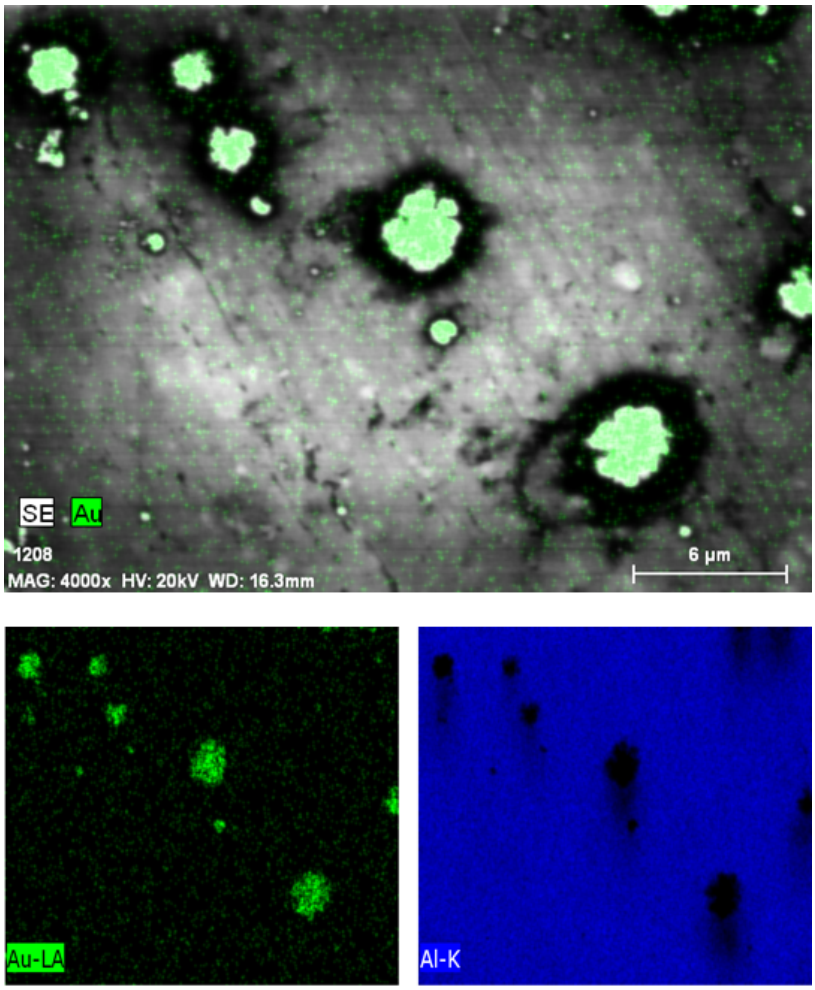

Figure E.2: EDX color maps confirmed the chemical identity of gold after electrospinning.

Figure E.3 shows that the gold particles only formed in the areas wetted with ethanol.

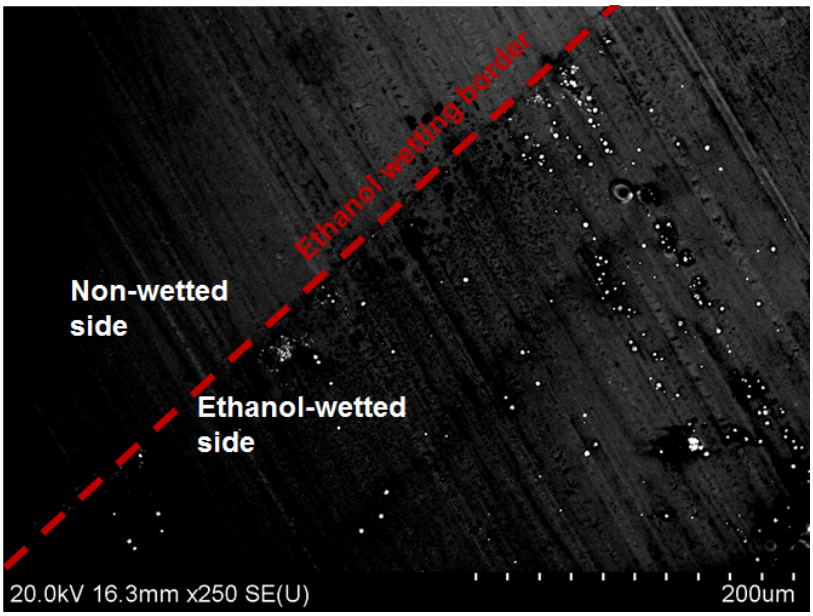

Figure E.3: Gold particles formed by electrospinning only in places where ethanol was present.

The effect of nozzle-substrate distance, voltage, substrate and many other factors can be investigated in a systematic set of experiments for obtaining various structures.

Appendix F

Gold Clamps

Section 6.4.2 described the pros and cons of using gold as an electrodeposition clamp material. Non-cyanide gold solutions (SOL1 to SOL4) were only tried for clamp electrodeposition. After 40 minutes, the amount of electrodeposited gold was negligible. Figure F.1 shows an attempt to fill a clamp box with gold using SOL2. Surface contamination from the photolithography process could have also interfered with the electrodeposition process.

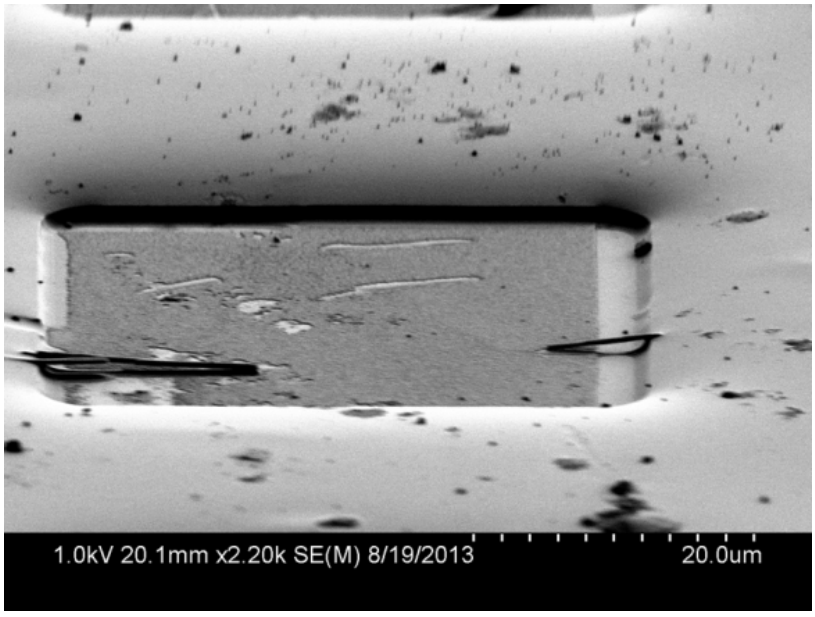

Figure F.1: A clamp box to be filled with gold deposit from SOL2. After 40 minutes only a very thin layer of gold was deposited.

For improving the quality of the clamp from gold chloride solution (SOL4), EDTA

was also added to the solution to see if the compactness and morphology of the deposit can be changed. A solution of 6.25 g/L $HAuCl_4 \cdot 3H_2O$ and 2 g/L EDTA (SOL3) was prepared and used for electrodeposition of gold on evaporated gold substrates at two different current densities. Figure F.2A and B show the morphology of electrodeposited gold at current densities 0.1 and 3.3 mA/cm^2, respectively.

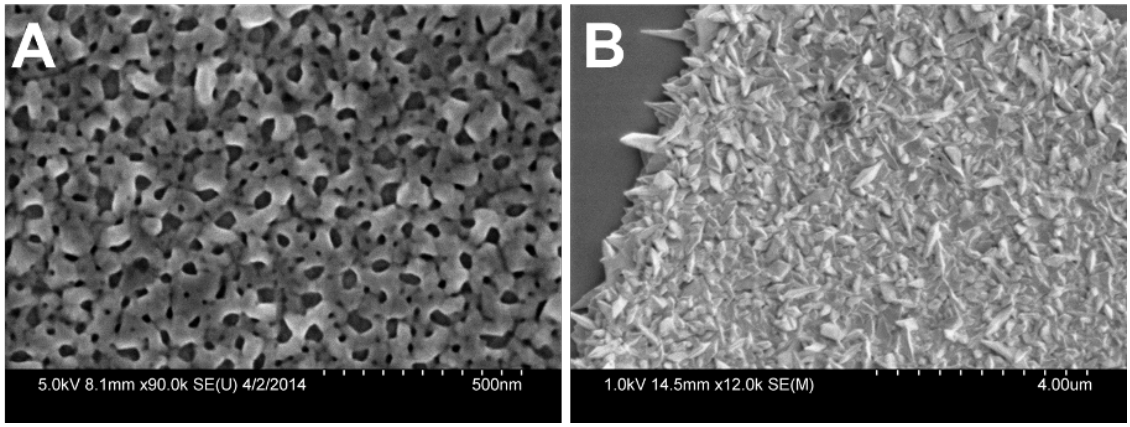

Figure F.2: SEM images of two distinct gold morphologies obtained from SOL3 under current densities of (A) 0.1 mA/cm^2 and (B) 3.3 mA/cm^2.

Bibliography

[1] M Schlesinger and M Paunovic. *Fundamentals of electrochemical deposition*. Wiley, 2006.

[2] CR Sides and CR Martin. Deposition into templates. In *Electrochemistry at the Nanoscale*, pages 279–320. Springer, 2009.

[3] M Li, RB Bhiladvala, TJ Morrow, JA Sioss, K Lew, JM Redwing, CD Keating, and TS Mayer. Bottom-up assembly of large-area nanowire resonator arrays. *Nat. Nanotechnol.*, 3(2):88–92, 2008.

[4] M Li, TS Mayer, JA Sioss, CD Keating, and RB Bhiladvala. Template-grown metal nanowires as resonators: Performance and characterization of dissipative and elastic properties. *Nano Lett.*, 7(11):3281–3284, 2007.

[5] B Wu, A Heidelberg, and JJ Boland. Mechanical properties of ultrahigh-strength gold nanowires. *Nat. Mater.*, 4(7):525–529, 2005.

[6] Y Liu, JH Chung, WK Liu, and RS Ruoff. Dielectrophoretic assembly of nanowires. *J. Phys. Chem. B*, 110(29):14098–14106, 2006.

[7] RB Bhiladvala. Nanomechanical resonant sensors and fluid interactions. In *Encyclopedia of Nanotechnology*, pages 1630–1643. Springer, 2012.

[8] JA Sioss, RB Bhiladvala, W Pan, M Li, S Patrick, P Xin, SL Dean, CD Keating, TS Mayer, and GA Clawson. Nanoresonator chip-based RNA sensor strategy for detection of circulating tumor cells: response using PCA3 as a prostate cancer marker. *Nanomed-Nanotechnol.*, 8(6):1017–1025, 2012.

[9] N Moghimian, M Sam, JD Coelho, SDW Warwick, and RB Bhiladvala. Suppressing electroless growth allows cyanide-free electrodeposition of straight separable gold nanowires. *Electrochim. Acta*, 114:643–648, 2013.

[10] N Moghimian, M Sam, and RB Bhiladvala. Rhodium nanowires: Synthesis and nanostructure tailoring by controlling hydrogen evolution. *Mater. Lett.*, 113: 152–155, 2013.

[11] Z Zhang, S Dai, DA Blom, and J Shen. Synthesis of ordered metallic nanowires inside ordered mesoporous materials through electroless deposition. *Chem. Mater.*, 14(3):965–968, 2002.

[12] Z Miao, D Xu, J Ouyang, G Guo, X Zhao, and Y Tang. Electrochemically induced sol-gel preparation of single-crystalline TiO_2 nanowires. *Nano Lett.*, 2 (7):717–720, 2002.

[13] TR Kline, M Tian, J Wang, A Sen, MWH Chan, and TE Mallouk. Template-grown metal nanowires. *Inorg. Chem.*, 45(19):7555–7565, 2006.

[14] US Mohanty. Electrodeposition: a versatile and inexpensive tool for the synthesis of nanoparticles, nanorods, nanowires, and nanoclusters of metals. *J. Appl. Electrochem.*, 41(3):257–270, 2011.

[15] SR Nicewarner-Pena, RG Freeman, BD Reiss, L He, DJ Peña, ID Walton, R Cromer, CD Keating, and MJ Natan. Submicrometer metallic barcodes. *Science*, 294(5540):137–141, 2001.

[16] HH Lou and Y Huang. Encyclopedia of chemical processing. 2005.

[17] FR Hartley. *Chemistry of the platinum group metals: recent developments*. Elsevier, Amsterdam ; New York, 1991.

[18] CJ Murphy, AM Gole, JW Stone, PN Sisco, AM Alkilany, EC Goldsmith, and SC Baxter. Gold nanoparticles in biology: Beyond toxicity to cellular imaging. *Accounts Chem. Res.*, 41(12):1721–1730, 2008.

[19] A Bruno Frazier and MG Allen. Metallic microstructures fabricated using photosensitive polyimide electroplating molds. *J. Microelectromech S.*, 2(2):87–94, 1993.

[20] CP Bean. Process for filling pores. U.S. Patent No. 3483095, 1969.

[21] GE Possin. A method for forming very small diameter wires. *Rev. Sci. Instrum.*, 41(5):772–774, 1970.

[22] WD Williams and N Giordano. Fabrication of 80 Å metal wires. *Rev. Sci. Instrum.*, 55(3):410–412, 1984.

[23] RM Penner and CR Martin. Preparation and electrochemical characterization of ultramicroelectrode ensembles. *Anal. Chem.*, 59(21):2625–2630, 1987.

[24] SK Chakarvarti and J Vetter. Template synthesis –a membrane based technology for generation of nano-/micro materials: a review. *Radiat. Meas.*, 29(2): 149 – 159, 1998.

[25] JD Klein, RD Herrick, D Palmer, MJ Sailor, CJ Brumlik, and CR Martin. Electrochemical fabrication of cadmium chalcogenide microdiode arrays. *Chem. Mater.*, 5(7):902–904, 1993.

[26] CR Martin. Nanomaterials - a membrane-based synthetic approach. *Science*, 266(5193):1961–1966, 1994.

[27] CR Martin. Membrane-based synthesis of nanomaterials. *Chem. Mater.*, 8(8): 1739–1746, 1996.

[28] CR Martin. Template synthesis of electronically conductive polymer nanostructures. *Accounts of chemical research*, 28(2):61–68, 1995.

[29] BE Fischer and R Spohr. Production and use of nuclear tracks: imprinting structure on solids. *Rev. Mod. Phys.*, 55(4):907, 1983.

[30] SK Chakarvarti and J Vetter. Morphology of etched pores and microstructures fabricated from nuclear track filters. *Nucl. Instrum. Meth. B*, 62(1):109–115, 1991.

[31] R Spohr. *Ion tracks and microtechnology: principles and applications*. Friedrich Vieweg & Sohn Verlagsgesellschaft, 1990.

[32] C Schönenberger, BMI Van der Zande, LGJ Fokkink, M Henny, C Schmid, M Krüger, A Bachtold, R Huber, H Birk, and U Staufer. Template synthesis of nanowires in porous polycarbonate membranes: electrochemistry and morphology. *J. Phys. Chem. B*, 101(28):5497–5505, 1997.

[33] P Apel. Track etching technique in membrane technology. *Radiat. Meas.*, 34 (1):559–566, 2001.

[34] YN Xia, PD Yang, YG Sun, YY Wu, B. Mayers, B. Gates, YD Yin, F. Kim, and YQ Yan. One-dimensional nanostructures: Synthesis, characterization, and applications. *Adv. Mater.*, 15(5):353–389, 2003.

[35] S Jin, MJ Bierman, and SA Morin. A new twist on nanowire formation: Screw-dislocation-driven growth of nanowires and nanotubes. *J. Phys. Chem. Lett.*, 1 (9):1472–1480, 2010.

[36] AR Tao, S Habas, and P Yang. Shape control of colloidal metal nanocrystals. *Small*, 4(3):310–325, 2008.

[37] O Yevtushenko, H Natter, and R Hempelmann. Grain-growth kinetics of nanostructured gold. *Thin Solid Films*, 515(1):353–356, 2006.

[38] B Scharifker and G Hills. Theoretical and experimental studies of multiple nucleation. *Electrochim. Acta*, 28(7):879–889, 1983.

[39] M Schlesinger and M Paunovic. *Modern Electroplating*. John Wiley & Sons, 4 edition, 2000.

[40] L Oniciu and L Mureşan. Some fundamental aspects of levelling and brightening in metal electrodeposition. *J. Appl. Electrochem.*, 21(7):565–574, 1991.

[41] MET Molares, V Buschmann, D Dobrev, R Neumann, R Scholz, IU Schuchert, and J Vetter. Single-crystalline copper nanowires produced by electrochemical deposition in polymeric ion track membranes. *Adv. Mater*, 13(1):5, 2001.

[42] DB Williams and CB Carter. *The Transmission Electron Microscope*. 2 edition, 2009.

[43] VM Dusevich, JH Purk, and JD Eick. Choosing the right accelerating voltage for SEM (an introduction for beginners). *Microscopy Today*, 18(01):48–52, 2010.

[44] SSV Tatiparti and F Ebrahimi. Potentiostatic versus galvanostatic electrodeposition of nanocrystalline Al–Mg alloy powders. *J. Solid State Electr.*, 16(3): 1255–1262, 2012.

[45] L Soleimany, A Dolati, and M Ghorbani. A study on the kinetics of gold nanowire electrodeposition in polycarbonate templates. *J. Electroanal. Chem.*, 645(1):28–34, 2010.

[46] RJ Morrissey. Noncyanide silver plating. Technical report, Technic, Incorporated, Providence, RI.

[47] S Roy. Electrochemical gold deposition from non-toxic electrolytes. *ECS Trans.*, 16(36):67–72, 2009.

[48] ML Wu, WJ Tsai, A. Ger, JF Deng, SH Tsay, and MH Yang. Cholestatic hepatitis caused by acute gold potassium cyanide poisoning. *J. Toxicol-Clin. Toxic.*, 39(7):739–743, 2001.

[49] MG Budden and DS Wilkinson. Skin and nail lesions from gold potassium cyanide. *Contact Dermatitis*, 4(3):172–173, 1978.

[50] IH Wright and CJ Vesey. Acute-poisoning with gold cyanide. *Anaesthesia*, 41 (9):936–939, 1986.

[51] G Baltrūnas, A Valiūnienė, J Vienožinskis, E Gaidamauskas, T Jankauskas, and Z Margarian. Electrochemical gold deposition from sulfite solution: application for subsequent polyaniline layer formation. *J. Appl. Electrochem.*, 38(11):1519–1526, 2008.

[52] H Honma and Y Kagaya. Gold plating using the disulfiteaurate complex. *J. Electrochem. Soc.*, 140(9):L135–L137, 1993.

[53] H Honma and K Hagiwara. Fabrication of gold bumps using gold sulfite plating. *J. Electrochem. Soc*, 142(1):81–87, 1995.

[54] H Kuhn and D Medlin. ASM handbook. volume 8: Mechanical testing and evaluation. *ASM International, Materials Park, OH 44073-0002, USA, 998*, 2000.

[55] SS Chang, CW Shih, CD Chen, WC Lai, and CRC Wang. The shape transition of gold nanorods. *Langmuir*, 15(3):701–709, 1999.

[56] E Gil-Santos, D Ramos, J Martínez, M Fernández-Regúlez, R García, A San Paulo, M Calleja, and J Tamayo. Nanomechanical mass sensing and stiffness spectrometry based on two-dimensional vibrations of resonant nanowires. *Nat. Nanotechnol.*, 5(9):641–645, 2010.

[57] TJ Morrow, M Li, J Kim, TS Mayer, and CD Keating. Programmed assembly of DNA-coated nanowire devices. *Science*, 323(5912):352–352, 2009.

[58] B He, TJ Morrow, and CD Keating. Nanowire sensors for multiplexed detection of biomolecules. *Curr. Opin. Chem. Biol.*, 12(5):522–528, 2008.

[59] S Ramanathan, DL Koch, and RB Bhiladvala. Noncontinuum drag force on a nanowire vibrating normal to a wall: Simulations and theory. *Phys. Fluids*, 22: 103101, 2010.

[60] YT Yang, C Callegari, XL Feng, KL Ekinci, and ML Roukes. Zeptogram-scale nanomechanical mass sensing. *Nano Lett.*, 6(4):583–586, 2006.

[61] A Heidelberg, LT Ngo, B Wu, MA Phillips, S Sharma, TI Kamins, JE Sader, and JJ Boland. A generalized description of the elastic properties of nanowires. *Nano Lett.*, 6(6):1101–1106, 2006.

[62] CR Weinberger and W Cai. Plasticity of metal nanowires. *J. Mater. Chem.*, 22(8):3277–3292, 2012.

[63] W Wang, LA Castro, M Hoyos, and TE Mallouk. Autonomous motion of metallic microrods propelled by ultrasound. *ACS Nano*, 6(7):6122–6132, 2012.

[64] B Edwards, TS Mayer, and RB Bhiladvala. Synchronous electrorotation of nanowires in fluid. *Nano Lett.*, 6(4):626–632, 2006.

[65] BD Smith, TS Mayer, and CD Keating. Deterministic assembly of functional nanostructures using nonuniform electric fields. *Annu. Rev. Phys. Chem.*, 63: 241–263, 2012.

[66] MCP Wang and BD Gates. Directed assembly of nanowires. *Mater. Today*, 12 (5):34–43, 2009.

[67] JKN Mbindyo, BD Reiss, BR Martin, CD Keating, MJ Natan, and TE Mallouk. DNA-directed assembly of gold nanowires on complementary surfaces. *Adv. Mater.*, 13(4):249–254, 2001.

[68] JM Moon and A Wei. Uniform gold nanorod arrays from polyethylenimine-coated alumina templates. *J. Phys. Chem. B*, 109(49):23336–23341, 2005.

[69] JG. Wang, ML Tian, TE Mallouk, and MHW Chan. Microstructure and interdiffusion of template-synthesized Au/Sn/Au junction nanowires. *Nano Lett.*, 4 (7):1313–1318, 2004.

[70] TA Green. Gold electrodeposition for microelectronic, optoelectronic and microsystem applications. *Gold Bull.*, 40(2):105–114, 2007.

[71] J Liu, JL Duan, E Toimil-Molares, S Karim, TW Cornelius, D Dobrev, HJ Yao, YM Sun, MD Hou, D Mo, ZG Wang, and R Neumann. Electrochemical fabrication of single-crystalline and polycrystalline Au nanowires: the influence of deposition parameters. *Nanotechnology*, 17(8):1922–1926, 2006.

[72] Q Xu, G Meng, F Han, X Zhao, M Kong, and X Zhu. Controlled fabrication of gold and polypyrrole nanowires with straight and branched morphologies via porous alumina template-assisted approach. *Mater. Lett.*, 63(16):1431–1434, 2009.

[73] L Wang, Y Song, L Sun, C Guo, Y Sun, and Z Li. Controllable synthesis of gold nanowires. *Mater. Lett.*, 62(25):4124–4126, 2008.

[74] X Hou, X Zhang, S Chen, Y Fang, N Li, X Zhai, and Y Liu. Size-controlled synthesis of Au nanoparticles and nanowires and their application as SERS substrates. *Colloid. Surface. A*, 384(1-3):345–351, 2011.

[75] CX Kan, WP Cai, ZS Li, GH Fu, and LD Zhang. Reduction effect of pore wall and formation of Au nanowires inside monolithic mesoporous silica. *Chem. Phys. Lett.*, 382(3-4):318–324, 2003.

[76] C Huang, J Jiang, M Lu, L. Sun, EI Meletis, and Y Hao. Capturing electrochemically evolved nanobubbles by electroless deposition. A facile route to the synthesis of hollow nanoparticles. *Nano Lett.*, 9(12):4297–4301, 2009.

[77] FQ Sun, WP Cai, Y Li, BQ Cao, F Lu, GT Duan, and LD Zhang. Morphology control and transferability of ordered through-pore arrays based on electrodeposition and colloidal monolayers. *Adv. Mater.*, 16(13):1116–1121, 2004.

[78] A He, Q Liu, and DG Ivey. Development of stable, non-cyanide solutions for electroplating Au-Sn alloy films. *J. Mater. Sci-Mater. El.*, 17(1):63–70, 2006.

[79] XY Zhang, LD Zhang, Y Lei, LX Zhao, and YQ Mao. Fabrication and characterization of highly ordered Au nanowire arrays. *J. Mater. Chem.*, 11(6): 1732–1734, 2001.

[80] K Hayashi and Y Hirose. Displacement gold plating solution, February 26 2003. EP Patent 1,285,979.

[81] BL Rivas and KE Geckeler. Synthesis and metal complexation of poly(ethyleneimine) and derivatives. *Adv. Polym. Sci.*, 102:171–188, 1992.

[82] O Boussif, F Lezoualc'h, MA Zanta, MD Mergny, D Scherman, B Demeneix, and J Behr. A versatile vector for gene and oligonucleotide transfer into cells in culture and in vivo: polyethylenimine. *P. Natl. Acad. Sci.*, 92(16):7297–7301, 1995.

[83] MMO Sullivan, JJ Green, and TM Przybycien. Development of a novel gene delivery scaffold utilizing colloidal gold–polyethylenimine conjugates for DNA condensation. *Gene Ther.*, 10(22):1882–1890, 2003.

[84] J Mao, J Yao, L Wang, and W Liu. Easily prepared high-quantum-yield CdS quantum dots in water using hyperbranched polyethylenimine as modifier. *J. Colloid Interface. Sci.*, 319(1):353–356, 2008.

[85] ML Tian, JU Wang, J Kurtz, TE Mallouk, and MHW Chan. Electrochemical growth of single-crystal metal nanowires via a two-dimensional nucleation and growth mechanism. *Nano Lett.*, 3(7):919–923, 2003.

[86] EM Freer, O Grachev, X Duan, S Martin, and DP Stumbo. High-yield self-limiting single-nanowire assembly with dielectrophoresis. *Nat. Nanotechnol.*, 5 (7):525–530, 2010.

[87] X Sun, S Dong, and E Wang. One-step synthesis and characterization of polyelectrolyte-protected gold nanoparticles through a thermal process. *Polymer*, 45(7):2181–2184, 2004.

[88] C Hageluken. Markets for the catalyst metals platinum, palladium and rhodium. *Metal-Berlin*, 60(1):31–42, 2006.

[89] S Chandra, KS Lokesh, A Nicolai, and H Lang. Dendrimer-rhodium nanoparticle modified glassy carbon electrode for amperometric detection of hydrogen peroxide. *Anal. Chim. Acta*, 632(1):63–68, 2009.

[90] R Leghrib, T Dufour, F Demoisson, N Claessens, F Reniers, and E Llobet. Gas sensing properties of multiwall carbon nanotubes decorated with rhodium nanoparticles. *Sensors Actuat. B-Chem.*, 160(1):974–980, 2011.

[91] F Muench, C Neetzel, S Kaserer, J Brötz, J Jaud, Z Zhao-Karger, S Lauterbach, H Kleebe, C Roth, and W Ensinger. Fabrication of porous rhodium nanotube catalysts by electroless plating. *J. Mater. Chem.*, 22(25):12784–12791, 2012.

[92] M Pushpavanam, V Raman, and BA Shenoi. Rhodium– electrodeposition and applications. *Surf. Technol.*, 12(4):351–360, 1981.

[93] D Pletcher and RI Urbina. Electrodeposition of rhodium .2. sulfate solutions. *J. Electroanal. Chem.*, 421(1-2):145–151, 1997.

[94] F Yang, DK Taggart, and RM Penner. Fast, sensitive hydrogen gas detection using single palladium nanowires that resist fracture. *Nano Lett.*, 9(5):2177–2182, 2009.

[95] D Wang, Y Liu, X Zhou, J Sun, and T You. Edta-controlled one-pot preparation of novel shaped gold microcrystals and their application in surface-enhanced raman scattering. *Chem. Lett.*, 36(7):924–925, 2007.

[96] JR Hart. *Ethylenediaminetetraacetic Acid and Related Chelating Agents*. Wiley-VCH Verlag GmbH Co. KGaA, 2000.

[97] A Pangon, K Tashiro, and S Chirachanchai. Polyethylenimine containing benzimidazole branching: a model system providing a balance of hydrogen bond network or chain mobility enhances proton conductivity. *J. Phys. Chem. B*, 115 (39):11359–11367, 2011.

[98] R Tanaka, H Yamamoto, A Shono, K Kubo, and M Sakurai. Proton conducting behavior in non-crosslinked and crosslinked polyethylenimine with excess phosphoric acid. *Electrochim. Acta*, 45(8):1385–1389, 2000.

[99] N Moghimian, EA Etrati, M Sam, and RB Bhiladvala. Hybridizing micromachining and microfabrication for sensor chips. In *Proceedings of the 8th International Conference on MicroManufacturing*, number 121. March 2013.

[100] Q Qin, F Xu, Y Cao, PI Ro, and Y Zhu. Measuring true young's modulus of a cantilevered nanowire: Effect of clamping on resonance frequency. *Small*, 8 (16):2571–2576, 2012.

[101] A San Paulo, J Bokor, RT Howe, R He, P Yang, D Gao, C Carraro, and R Maboudian. Mechanical elasticity of single and double clamped silicon nanobeams fabricated by the vapor-liquid-solid method. *Appl. Phys. Lett.*, 87 (5):053111, 2005.

[102] M Belov, NJ Quitoriano, S Sharma, WK Hiebert, TI Kamins, and S Evoy. Mechanical resonance of clamped silicon nanowires measured by optical interferometry. *J. Appl. Phys.*, 103(7):074304, 2008.

[103] M Li. *Hybrid Integration of Nanowire Resonator Arrays.* PhD thesis, The Pennsylvania State University, 2008.

[104] W Weaver Jr, SP Timoshenko, and DH Young. *Vibration problems in engineering.* John Wiley & Sons, 1990.

[105] M Defoort, KJ Lulla, T Crozes, O Maillet, O Bourgeois, and E Collin. Slippage and boundary layer probed in an almost ideal gas by a nanomechanical oscillator. *Phys. Rev. Lett.*, 113(13):136–101, 2014.

[106] H Struchtrup and P Taheri. Macroscopic transport models for rarefied gas flows: a brief review. *IMA J. Appl. Math.*, 76(5):672–697, 2011.